

**SILICON-BASED PLANAR PHOTONIC CRYSTALS  
FOR APPLICATION TO  
DISPERSION COMPENSATION**

**Dissertation**

zur Erlangung des akademischen Grades

Doctor ingenieur (Dr. ing.)

vorgelegt der

Mathematisch-Naturwissenschaftlich-Technischen Fakultät  
(Fachbereich Ingenieurwissenschaften)  
der Martin-Luther-Universität Halle-Wittenberg

von Cécile Jamois  
geb.: 19.04.1977 in Rennes

Gutachter:

1. Prof. Ulrich Gösele
2. Prof. Manfred Eich
3. Prof. Henry Benisty

Halle (Saale), 16. Juni 2004

**urn:nbn:de:gbv:3-000007058**

[<http://nbn-resolving.de/urn/resolver.pl?urn=nbn%3Ade%3Agbv%3A3-000007058>]

---

## Abstract

The principle and the feasibility of dispersion compensators in planar photonic crystals based on the insulator-on-silicon-on-insulator (IOSOI,  $\text{SiO}_2/\text{Si}/\text{SiO}_2$ ) system was demonstrated. This dispersion compensator should compensate for the dispersion of a single-wavelength channel with a bandwidth of 0.4 nm, corresponding to 40 GHz at 1.55  $\mu\text{m}$  wavelength, and be integrated into a silicon chip, in order to be compatible with other electrical and optical integrated devices. Due to the small thickness of the silicon core and the high index contrast between the core and the oxide claddings, the behavior of the IOSOI system is fully three-dimensional and combines the properties of a two-dimensional photonic crystal with those of a planar waveguide. Performing theoretical studies on the properties of this planar photonic crystal, a design of a dispersion compensator taking into account several requirements for a good device functionality was elaborated and optimized. Issues like the light confinement, the radiation losses, the existence of cladding modes, as well as their consequences on the device properties were addressed. Light coupling from an integrated ridge waveguide into the photonic crystal waveguide used as dispersion compensator was also discussed. Though challenging, the experimental fabrication of such devices, compatible with the standard silicon technology, was demonstrated. Moreover, a theoretical estimate showed that the small experimental imperfections, arising from the process difficulties, may be compensated after fabrication by tuning via free-carrier injection.

## Zusammenfassung

Das Prinzip und die Realisierbarkeit von Dispersionskompensatoren in IOSOI (insulator-on-silicon-on-insulator,  $\text{SiO}_2/\text{Si}/\text{SiO}_2$ )-basierten planaren photonischen Kristallen ist bewiesen worden. Der zu realisierende Dispersionskompensator soll voll kompatibel zu anderen integrierten (elektrischen als auch optischen) Modulen werden. Dafür muss er in einen "silicon-on-insulator" (SOI) Chip integriert werden. Dabei ist die Zielvorgabe, die Dispersion eines einzelnen Kanals mit 40 GHz Bandbreite bei 1.55  $\mu\text{m}$  Wellenlänge zu kompensieren. Wegen der dünnen Silizium Schichtdicke und dem hohen Indexkontrast zwischen dem Silizium und den zwei Oxyd Deckschichten, ist das Verhalten des planaren photonischen Kristalls dreidimensional, und es kombiniert die Eigenschaften eines zwei-dimensionalen photonischen Kristalls mit denen eines planaren Wellenleiters. Nach theoretischer Untersuchung der Eigenschaften des planaren photonischen Kristalls wurde ein Wellenleiterdesign ausgewählt und verbessert, um es als Dispersionskompensator einsetzen zu können. Fragestellungen wie die Lichtbeschränkung, die Radiationsverluste, oder die Existenz von "Claddingmoden" wurden untersucht. Zum Abschluss der Untersuchung wurde auch auf Fragen der Lichteinkopplung in den Wellenleiter eingegangen. Auch wenn die mit der Standardsiliziumtechnologie kompatible experimentelle Herstellung solcher Module sehr aufwendig ist, konnte gezeigt werden, dass sie möglich ist. Darüberhinaus wurde gezeigt, dass kleine experimentelle Unzulänglichkeiten, welche durch Prozessschwierigkeiten entstehen, durch die Injektion von freien Ladungsträgern nachträglich kompensiert werden können.

# Contents

<b>1</b>	<b>Motivation</b>	<b>4</b>
1.1	Introduction . . . . .	4
1.2	Dispersion Compensators: Background . . . . .	6
1.2.1	Why Do We Need Dispersion Compensators? . . . . .	6
1.2.2	Currently Used Dispersion Compensators . . . . .	7
1.3	Photonic-Crystal-Based Dispersion Compensators: Principle . . . . .	9
1.3.1	Two-Dimensional Photonic Crystals . . . . .	9
1.3.2	Waveguides in Two-Dimensional Photonic Crystals . . . . .	11
1.3.3	Photonic Crystals-Based Dispersion Compensators . . . . .	15
1.3.4	Requirements . . . . .	17
<b>2</b>	<b>Study of the Bulk Photonic Crystal Slab</b>	<b>19</b>
2.1	Selection of the Material System . . . . .	19
2.2	Effects of the Vertical Confinement . . . . .	20
2.2.1	Higher-Order Modes . . . . .	20
2.2.2	Polarization Mixing . . . . .	23
2.2.3	2D-3D Transition . . . . .	24
2.2.4	Planar Waveguide Approximation . . . . .	25
2.2.5	Selection of the Slab Thickness . . . . .	27
2.3	Light Line and Resonant Modes . . . . .	29
2.3.1	Guided Modes and Resonant Modes . . . . .	29
2.3.2	Computation of Resonant Modes . . . . .	30
2.3.3	Determination of Radiation Losses . . . . .	31
2.4	Discussion of the Band Structure . . . . .	33
2.4.1	Origin of the Modes . . . . .	33
2.4.2	Cladding Modes and Surface Modes . . . . .	35
2.4.3	Consequences on the Planar-Photonic-Crystal Properties . . . . .	38
2.5	Conclusions . . . . .	43
<b>3</b>	<b>Design of the Dispersion Compensator</b>	<b>44</b>
3.1	Dispersion Properties . . . . .	44
3.1.1	Selection of the Waveguide Type . . . . .	44
3.1.2	Study of the Selected Design . . . . .	47
3.2	Propagation Losses . . . . .	53
3.2.1	Radiation Losses . . . . .	53
3.2.2	Coupling to Bulk Modes . . . . .	55
3.3	Tunability . . . . .	57
3.3.1	Liquid Crystal Infiltration . . . . .	58
3.3.2	Free Carrier Injection . . . . .	60
3.4	Coupling Issues . . . . .	62
3.4.1	Impedance Matching . . . . .	63

3.4.2	Mode Matching . . . . .	64
3.4.3	Band Flatness . . . . .	65
3.5	Conclusions and Full Design . . . . .	67
<b>4</b>	<b>Experimental Fabrication</b>	<b>69</b>
4.1	Overview on the Fabrication Process . . . . .	69
4.2	Electron-Beam Lithography . . . . .	70
4.2.1	Design of the Masks . . . . .	73
4.2.2	Results of Resist Patterning . . . . .	75
4.3	Cr Etching . . . . .	77
4.3.1	Preliminary Result . . . . .	77
4.3.2	Optimization of the Gas Composition . . . . .	78
4.3.3	Optimization of the RF Power . . . . .	78
4.3.4	Further Optimization of the Process . . . . .	79
4.4	Silicon and Silicon Dioxide Etching . . . . .	82
4.4.1	Results for RIE Etching . . . . .	82
4.4.2	Results for ICP Etching . . . . .	83
4.5	Conclusions . . . . .	89
<b>5</b>	<b>Conclusion and Outlook</b>	<b>90</b>
5.1	Theory and Design of the Dispersion Compensator . . . . .	90
5.2	Experimental Fabrication . . . . .	91
<b>6</b>	<b>Appendix: Atlas of Waveguide Designs</b>	<b>93</b>
	<b>List of Abbreviations</b>	<b>105</b>
	<b>Bibliography</b>	<b>106</b>
	<b>List of Publications</b>	<b>113</b>
	<b>Acknowledgments</b>	<b>115</b>
	<b>Eidesstattliche Erklärung</b>	<b>116</b>
	<b>Curriculum Vitae</b>	<b>117</b>

# 1. Motivation

## 1.1 Introduction

In the last decades, strong efforts have been carried out to investigate and control the optical properties of materials, to confine light in specified regions, to prohibit its propagation or to allow it to propagate only in certain directions and at certain frequencies. The introduction of components based on total internal reflection for light guidance, such as optical fibers or integrated ridge waveguides, has enabled a revolution in the telecommunication and optical industry. In parallel to that, another way of controlling light, based on Bragg diffraction, has already been used in many devices like dielectric mirrors. In 1987, the principle of dielectric mirrors, leading to one-dimensional light reflection, was generalized to two and three dimensions [1, 2] founding a new class of materials: photonic crystals. Since then, this new field has gained continuously increasing interest [3].

Photonic crystals (PCs) are materials with a periodically varying dielectric constant. Many basic properties of PCs can be understood by following an analogy with their electronic counterparts the semiconductors, as illustrated in fig. 1.1. In the terminology of solid state physics, a crystal is an "infinite" periodic repetition of a unit cell, which consists of an arrangement of atoms or molecules with corresponding symmetry elements. Therefore, a crystal represents a periodic potential to the electron propagating through it, and the geometry of the lattice, as well as the nature of the atoms and their arrangement within the unit cell, are responsible for most electronic properties of the crystal.

In a similar way, PCs consist of an elementary building block of materials with different refractive indices arranged in a specific geometry with a spacial periodicity. Consequently, PCs represent a periodic dielectric constant to electromagnetic waves propagating through them. If the difference between the dielectric constants of the materials constituting the crystal is high enough, and the absorption of light by these materials is sufficiently low, the periodicity of the dielectric constant leads to many of the same phenomena for photons as the atomic potential does for electrons. In particular, if the wavelength of light incident on the crystal is of the same order of magnitude as the periodicity, the multiply-scattered waves at the dielectric interfaces interfere, leading to a band structure for photons.

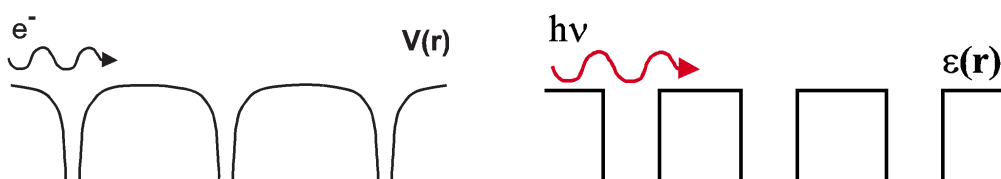


**Figure 1.1:** Analogy between a semiconductor lattice with a periodic atomic potential and a photonic crystal lattice having a periodic dielectric constant, (by A. Birner, Halle, 1999).

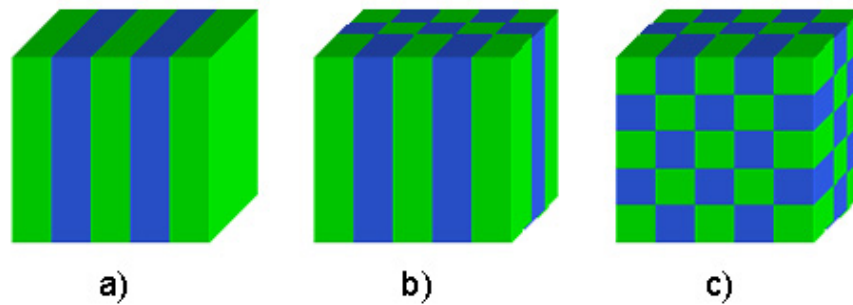


**Figure 1.2:** The three different classes of photonic crystals: a) one-dimensional, b) two-dimensional and c) three-dimensional photonic crystal. The different colors represent materials of different dielectric constants.

Depending on the number of directions in which the dielectric constant is periodically arranged, a PC can be one-, two-, or three-dimensional. In a one-dimensional (1D) photonic crystal, the dielectric constant is periodic along one axis and continuous in the plane normal to it (fig. 1.2a). A specific example is the dielectric mirror, which is a stack of periodically alternating layers of materials with different dielectric constants. Typically, if the layer thickness is a quarter of the wavelength, incident light is completely reflected, because the wavelength lies within the band gap of this PC structure.

If the dielectric constant is periodic in a plane and continuous in the direction normal to it, we speak of two-dimensional (2D) PCs (fig. 1.2b). A more detailed discussion of the properties of 2D PCs will be given later in this chapter. In three-dimensional (3D) PCs, the dielectric constant is periodic in all three directions  $x$ ,  $y$  and  $z$  (fig. 1.2c). Only in this last case a complete band gap for all directions and polarizations can be achieved. The structures of 3D PCs are very numerous and various, within which the most common being the inverted opals [4] and the wood-pile structure [6, 7]. Although these 3D PCs look very promising and have been theoretically widely studied, their experimental fabrication remains a challenge [4, 6, 7, 8, 9]. Therefore, 2D photonic crystals, which are much easier to fabricate and still offer most of the interesting properties of their 3D counterparts, have been investigated intensively. In particular, some years ago, the concept of PC slabs emerged [10, 11] and has been widely studied since then, because it offers a compromise between the 2D and 3D concepts. PC slabs, also called planar photonic crystals (PPCs), consist of a thin 2D PC surrounded by a lower-index material. Combining the index-guiding in the vertical direction with the presence of the photonic crystal in the plane of periodicity, a 3D control of light can be achieved [12, 13, 14].

Photonic crystals can be used for various purposes, such as lasing [15, 16], sensing [17, 18], opalescent coatings, wavelength multiplexing [19, 20], and other telecommunication applications [21, 22]. These applications are based on several interesting properties of the PC band structure and on their particular dispersion, e.g., modification of spontaneous emission [23, 24] or birefringence [25], superprism effect and negative refraction [26, 27, 28, 29]. Among these properties, the existence of a photonic band gap (PBG) is the most widely utilized property. PBGs, which prohibit the propagation of electromagnetic waves in certain directions and in specified frequency ranges, can lead to direct applications of PCs like filters, reflectors, waveguides, or cavities. Waveguides are key components in photonic integrated circuits, as they connect the different functional elements, such as sources, modulators, multiplexers, or detectors. In addition to the passive components like sharp bends or beam splitters, waveguides with a special functionality can also be designed and fabricated [30]. Since any small variation in

the waveguide design or in the material properties may lead to a large variation in the dispersion and propagation properties of the waveguide mode, lots of functionalities can be imagined and realized in PC waveguides, provided a suitable design is found. In particular, the concept of PC-based dispersion compensators (DCs) shows several pronounced advantages over the DCs currently used in the telecommunications, e.g., significant reduction of the device size and cost, as well as several possibilities of tuning the material properties after fabrication enabling to switch the dispersion properties, or simply to adjust them to the desired value in order to compensate some deviations arising from experimental imperfections.

To summarize, the aim of this work is the theory, the design and the fabrication of waveguides in silicon-based PPCs, with regard to an application as dispersion compensator. The DC to be realized will be integrated into a silicon-on-insulator (SOI) chip, in order to make it entirely compatible with other integrated optical devices.

## 1.2 Dispersion Compensators: Background

In order to understand the requirements of PC-based DCs, it is first necessary to delve briefly into the field of optical fibers and conventional dispersion compensating devices.

### 1.2.1 Why Do We Need Dispersion Compensators?

Since the prediction and first experimental fabrication of optical fibers in 1970 [31, 32], optical fibers have experienced major improvements and diversity to satisfy the continuously increasing demand in data transmission [33]. As they allow long-distance wavelength division multiplexing (WDM) transmission, the emergence of single-mode fibers (SMFs) in the early 1980's and of optical amplifiers in 1989 entailed a radical change in transmission systems. In parallel to the large improvements in reducing losses and costs, as well as in enhancing the mechanical and temporal stability of SMFs, developments were performed to increase bandwidth and capacity. However, the transmission capacity and distance in WDM systems are still limited by several intrinsic material properties. In particular, when a pulse comprising a span of wavelengths is sent through an optical fiber to transmit information, the short-wavelength components propagate faster than the long-wavelength components, leading to a broadening of the pulse. This effect, which is due to the dependence of the refractive index on the wavelength (fig. 1.3a), is called chromatic dispersion and becomes more crucial with increasing bit-rate and bandwidth. Indeed, the pulse may be broadened to the point that it eventually interferes with neighboring pulses in the pulse train, resulting in transmission errors. Typically, the dispersion within a conventional SMF is 17 ps/nm/km at 1.55  $\mu\text{m}$  wavelength (fig. 1.3b), following the equation:

$$D = \frac{d(\frac{1}{v_g})}{d\lambda} = -\frac{\lambda}{c} \cdot \frac{d^2n}{(d\lambda)^2} \quad (1.1)$$

where  $v_g = d(\omega)/d(k)$  is the group velocity of the wave;  $\omega$ ,  $k$ ,  $\lambda$ ,  $n$ , and  $c$  are the angular frequency, the wave vector, the wavelength in the medium, the refractive index of the material, and the speed of light in vacuum, respectively.

Due to intrinsic material losses within the optical fibers, the signal has to be re-amplified regularly by repeaters in order to allow long-distance transmission. In conventional transmission systems, the optical pulse is converted into an electrical signal before amplification. Due to these

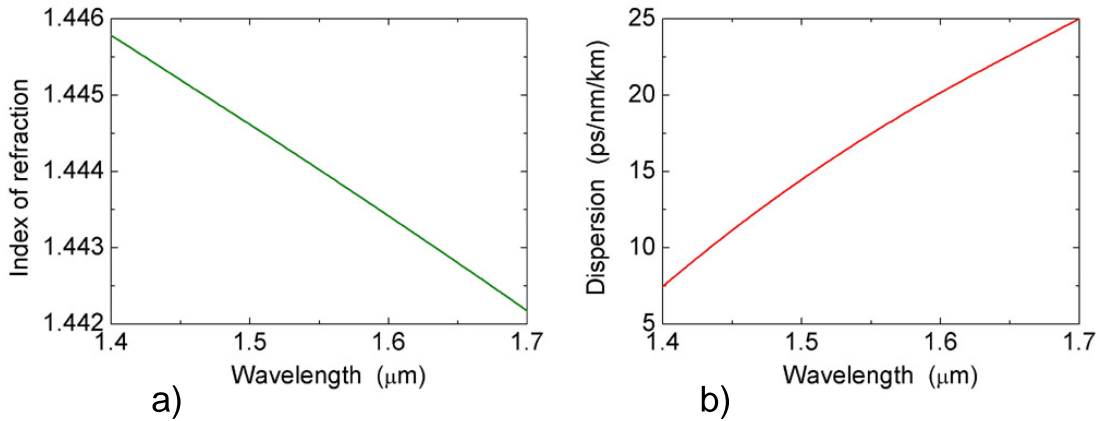


**Figure 1.3:** a) Variation of the refractive index and b) dispersion of light in a standard optical fiber around 1.55  $\mu\text{m}$  wavelength.

opto-electrical and electro-optical conversions, pulsed signals broadened by the dispersion are completely reshaped and the initial signals are regenerated. As a consequence, the transmission distance is unlimited, provided the repeaters are placed close enough to each other. However, this system is not convenient because the electrical signal limits the transmission capacity and speed. In systems using optical amplifiers as repeaters, transmitted signals are amplified with almost no changes in shape, so that long-distance data transmission requires dispersion compensation. The use of dispersion-shifted fibers with zero-dispersion around 1.55  $\mu\text{m}$  wavelength is one obvious solution to the problem of signal broadening. However, this is not always cost effective, in particular for conventional fiber networks that are already installed. Therefore, dispersion compensating devices are crucially needed for low-cost and high-capacity transmission over long distances, as well as in the Metronet.

## 1.2.2 Currently Used Dispersion Compensators

To date, there are mainly two different types of DCs used in telecom applications [33, 34], as illustrated in fig. 1.4. Beside the dispersion compensating fibers (DCFs), which are the most commonly used DCs in optical communication systems, fiber Bragg gratings (FBGs) have emerged in the last ten years and are starting to be introduced into optical networks.

The first DCFs were designed to compensate for the dispersion of a conventional SMF working at one wavelength around 1.55  $\mu\text{m}$  [35]. Since then, various practical DCFs were developed with a large negative dispersion  $D$  of -50 to -100 ps/nm/km at 1.55  $\mu\text{m}$  and a positive dispersion slope, allowing only single-wavelength dispersion compensation. However, the commercialization of WDM systems with wide bandwidths required the design of new types of DCFs, which should compensate for the dispersion slope together with the dispersion value. Such fibers should have a large negative dispersion value  $D$  along with a large negative dispersion slope  $S$ . This is achieved by modulating the refractive-index profile of the optical fiber, and by doping the fiber core with germanium. Typically, about 20 km DCF are necessary to compensate for the dispersion in 100 km SMF. However, since WDM transmission is very sensitive to higher-order material effects, the exact compensation of the dispersion slope is necessary, which has not been achieved so far. The unavoidable residual dispersion after compensation leads to severe limitations in terms of capacity of data transmission. One solution to overcome this drawback is the design and introduction into the transmission line of a complementary device, which should

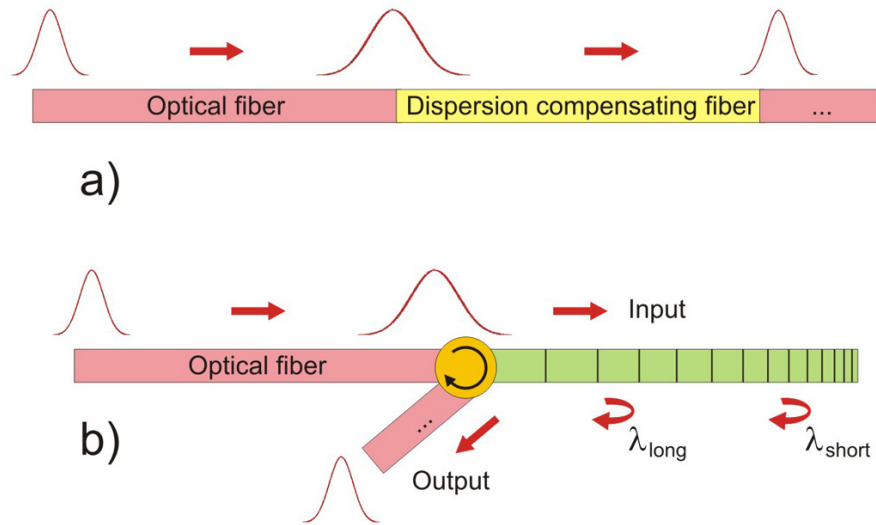


**Figure 1.4:** Schematics of the two main types of DCs currently commercially available. a) Dispersion compensating fiber (DCF) and b) fiber Bragg grating (FBG).

compensate for the residual pulse broadening beyond the DCF ability. Among the several solutions currently studied [36, 37, 38], PC-based devices are good candidates.

In FBGs, the photosensitivity of Ge-doped fibers is used to create a periodic perturbation of the refractive index in the fiber core [34]. The fiber core consists of a chirped 1D photonic crystal where the 1D photonic band gap is gradually blue-shifted along the fiber, so that the short-wavelength components travel longer than the long-wavelength components before being reflected. This device is used in reflection mode and needs a circulator at the entry to separate the input broadened data pulse from the output recompressed pulse. The longer the grating, the greater the compression factor and the wider the bandwidth of the device. Typically, several meters FBG are necessary to compensate for the dispersion of 100 km standard SMF. Although the high flexibility in fabrication allows, in principle, to achieve any dispersion slope and value, long-length devices are still challenging to fabricate, which delays the insertion of these devices into optical networks.

Although a great deal of work has been carried out to improve the fabrication processes as well as the properties of these two types of dispersion compensating devices [39, 40], both of them still present two common disadvantages: they are bulky and hard to tune or trim. Since their tuning range is very small (mainly done by temperature [41]), both devices are very sensitive to small imperfections due to the fabrication process.

Using photonic crystal waveguides as DCs, these two problems could potentially be overcome. While DCFs (resp. FBGs) have usually lengths in the km-range (resp. m-range), the same compensation can be achieved within a PC waveguide with only a few millimeters length, which would appreciably reduce the device cost. Furthermore, fine tuning of the dispersion properties of PC-based DCs after fabrication is possible by different means, in order to adjust them to the desired values. By tuning the overall material properties of either the dielectrics (e.g., by carrier injection) or an infiltrated material inside the pores (e.g., electro-optic or birefringent material), the dispersion can be adjusted.

## 1.3 Photonic-Crystal-Based Dispersion Compensators: Principle

Before presenting the principles of PC-based DCs, a brief review of the basic properties of photonic crystals is essential. We will first remind the reader of the properties of bulk 2D PCs and the introduction of defects into the lattice to build waveguides, and then discuss the concept of using the particular dispersion within PC waveguides for dispersion compensation.

### 1.3.1 Two-Dimensional Photonic Crystals

In general, 2D PCs consist of a lattice of parallel rods or pores embedded in a matrix with a different dielectric constant. This can be either air pores in a dielectric material or dielectric rods in air, ordered in a square or hexagonal lattice, so that the dielectric constant is homogeneous in the direction parallel to the rod axis - generally defined as  $z$ -direction - and periodic in the  $(x,y)$ -plane:

$$\varepsilon(\vec{r}) = \varepsilon(\vec{r} + \vec{R}) \quad (1.2)$$

where  $\vec{R}$  is any linear combination of the two unit vectors  $\vec{a}_1$  and  $\vec{a}_2$  of the 2D PC lattice:

$$\vec{R} = l\vec{a}_1 + m\vec{a}_2 \quad (1.3)$$

where  $l$  and  $m$  are integers.

As in solid state physics, this  $(\vec{r}, t)$ -space is bound to a reciprocal space  $(\vec{k}, \omega)$  with the following relation:

$$\vec{b}_i = \frac{2\pi}{V} \vec{a}_j \times \vec{a}_k \quad (1.4)$$

where  $\vec{b}_i$  is a primitive reciprocal lattice vector,  $\vec{a}_j$  and  $\vec{a}_k$  are primitive lattice vectors in the real space with  $i \neq j \neq k$  ( $i, j, k = 1, 2, \text{ or } 3$ ), and  $V = \vec{a}_i \cdot (\vec{a}_j \times \vec{a}_k)$  is the volume of the primitive cell in the real space.

In 2D and 3D, this reads:

$$\vec{a}_i \cdot \vec{b}_j = 2\pi\delta_{i,j} \quad (1.5)$$

where  $\delta_{i,j}$  is the Kronecker symbol.

Fig. 1.5 exhibits three examples of PC lattices for the case of 2D systems. The most commonly studied 2D lattices are the square [42], the hexagonal [43] and the honey-comb lattices [44, 45], the later being equivalent to a hexagonal lattice with a two-atom basis.

As in all electromagnetism systems, light propagation in PCs is governed by the four macroscopic Maxwell equations. They are (in the SI system):

$$\vec{\nabla} \cdot \vec{B} = 0 \quad (1.6)$$

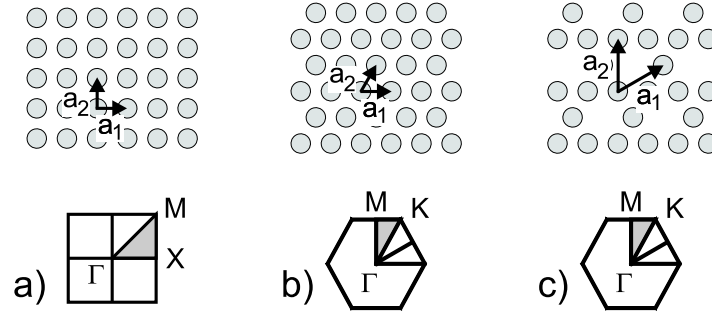


**Figure 1.5:** The most commonly studied 2D PC lattices and their first Brillouin zone. The irreducible Brillouin zone with the high-symmetry points is indicated in grey. a) square, b) hexagonal, and c) honeycomb lattices.

$$\vec{\nabla} \cdot \vec{D} = \rho \quad (1.7)$$

$$\vec{\nabla} \times \vec{H} - \frac{\partial \vec{D}}{\partial t} = \vec{J} \quad (1.8)$$

$$\vec{\nabla} \times \vec{E} + \frac{\partial \vec{B}}{\partial t} = 0 \quad (1.9)$$

where  $c$  is the speed of light,  $\vec{E}$  and  $\vec{H}$  are the macroscopic electric and magnetic fields,  $\vec{D}$  and  $\vec{B}$  are the displacement and magnetic induction fields, and  $\rho$  and  $\vec{J}$  are the free charge and current densities, respectively.

Due to the periodicity in PCs, the eigenfunctions  $\vec{E}$  and  $\vec{H}$  of the system can be written in the form of Bloch states. In the case that the magnetic field  $\vec{H}$  is used as the variable, this reads:

$$\vec{H}_{n, \vec{k}}(\vec{r}) = e^{i \vec{k} \cdot \vec{r}} \cdot \vec{u}_{n, \vec{k}}(\vec{r}) \quad (1.10)$$

where  $n$  is the band index,  $\vec{k}$  the wave vector, and the function  $\vec{u}_{n, \vec{k}}$  has the periodicity of the PC lattice:

$$\vec{u}_{n, \vec{k}}(\vec{r}) = \vec{u}_{n, \vec{k}}(\vec{r} + \vec{R}) \quad (1.11)$$

If the materials constituting the photonic crystal are assumed to be linear in their optical properties, isotropic, non-magnetic, and free of charges, the following wave equation ("master equation") can be obtained by combining Maxwell equations:

$$\vec{\nabla} \times \left( \frac{1}{\epsilon(\vec{r})} \vec{\nabla} \times \vec{H}(\vec{r}) \right) = \frac{\omega^2}{c^2} \cdot \vec{H}(\vec{r}) \quad (1.12)$$

this is an eigenvalue problem where the eigenvectors  $\vec{H}(\vec{r})$  are the eigenmodes, and the eigenvalues  $(\omega/c)^2$  are proportional to the squared frequency of these modes,  $c$  being the speed of light.

Furthermore, the transversality requirement:

$$\vec{\nabla} \cdot \vec{H}(\vec{r}) = 0 \quad (1.13)$$

has to be fulfilled.

By solving the master equation (1.12) for  $k$ -vectors along the irreducible Brillouin zone of the photonic crystal, the band structure of the PC is obtained, giving the allowed frequency values  $\omega$  for each wave vector  $k$ . In the case of 2D PCs, because all (x,y)-planes of periodicity is a mirror plane of the system, the polarizations decouple, i.e., the modes can be separated into transverse-electric (TE) modes having only  $H_z$ ,  $E_x$ , and  $E_y$  as non-zero components, and transverse-magnetic (TM) modes with the only non-zero components  $E_z$ ,  $H_x$ , and  $H_y$ . Since TE (resp. TM) modes have their magnetic (resp. electric) field oriented along the pore axis, they are often also called H (resp. E) modes. The band structures for TE and TM polarizations are usually different, because the electric field (resp. magnetic field) for TE and TM polarizations is oriented in different directions relatively to the dielectric interfaces within the photonic crystal [3]. A good overview on the band structures and basic properties of 2D PCs consisting of various materials arranged in the three different types of lattices presented in fig. 1.5 can be found in [46]. In the rest of this section, we focus on PCs consisting of a hexagonal lattice of circular air pores in silicon.

Fig. 1.6 gives an example of a band structure in the case of a hexagonal lattice of air pores in silicon with a relative radius  $r/a = 0.366$ , where  $a$  is the lattice constant of the photonic crystal. As will be discussed later in chapter 3, this particular relative-radius value yields the most stable PC properties. The band structure calculation was performed using the MIT package, a block-iterative frequency-domain code [47] with a grid of 64 points per lattice constant yielding good convergence of the results. For this relative radius value, a large TE band gap exists from 0.231 to 0.355 in normalized frequency  $\omega a/2\pi c$  (grey region in fig. 1.6). No TM band gap exists for this special set of parameters.

The variation of the photonic band gap position with the relative pore radius - the so-called gap map - for the hexagonal lattice of air pores in silicon is shown in fig. 1.7. In this system the TM band gap opens up only for a relative radius larger than 0.4, and overlaps with the TE band gap, leading to a complete band gap. The largest gap-midgap ratio - the ratio between band-gap width and midgap frequency - of the complete band gap is 16.3 % for a pore radius  $r/a = 0.478$ . However, such very large relative radius values are quite difficult to achieve experimentally. Therefore, most of the work based on the existence of a band gap in 2D PCs has focused on the TE band gap only, which is still quite large for smaller radii, e.g., at  $r/a = 0.366$  the gap-midgap ratio for TE modes is as large as 42.5 %.

### 1.3.2 Waveguides in Two-Dimensional Photonic Crystals

To build DCs, it is crucial to create waveguides within the PC lattice. The following section presents the basic properties and the designs of the standard types of PC waveguides.

If the periodicity of the PC is broken, a defect is created, with localized defect states. For an appropriate design of the defect, some of these states ought to be located within the band gap of

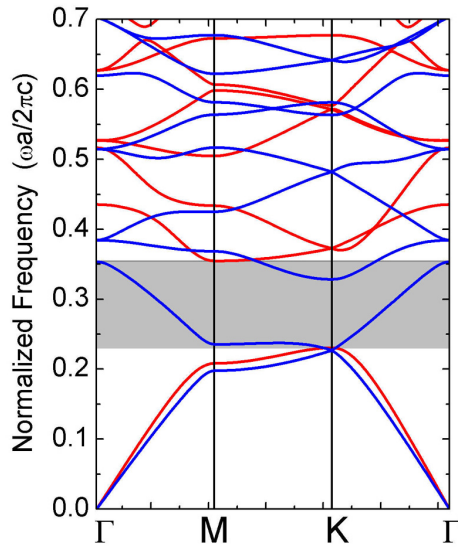


**Figure 1.6:** Band structures for TE (red lines) and TM (blue lines) polarizations of a 2D PC consisting of a hexagonal lattice of air pores in silicon. The air pores have a relative radius  $r/a = 0.366$ , and the dielectric constant of the silicon is  $\epsilon = 11.6$ . The grey region corresponds to the band gap for TE modes. The k-path considered is indicated in fig. 1.5b (MIT package calculation [47]).

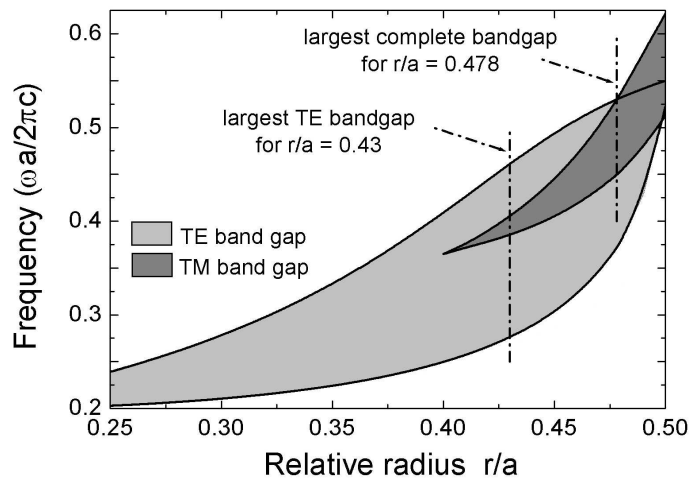


**Figure 1.7:** 2D gap map (normalized frequency  $\omega a/2\pi c$  versus relative pore radius  $r/a$ ) for a hexagonal lattice of air holes in silicon ( $\epsilon = 11.6$ ). The position of the largest gap-midgap ratios for the complete band gap as well as for the TE polarization are indicated (MIT package calculation [47]).

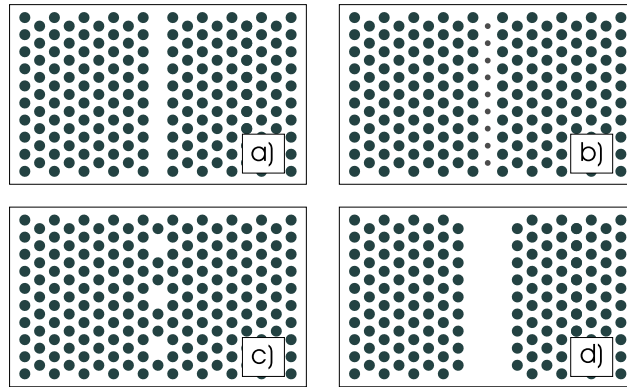


**Figure 1.8:** Four examples of waveguides in 2D hexagonal photonic crystals. a) W1 waveguide (i.e., waveguide having a width of one pore row) consisting of a row of missing pores, b) W1 waveguide consisting of a row of pores with smaller diameter, c) coupled-cavity-waveguide, and d) W3 waveguide (i.e., three pore-rows wide).

the PC [3]. Therefore, a line defect acts as a waveguide, since light cannot escape into the PC at this frequency and is thus guided along the line defect.

Fig. 1.8 shows some examples of linear waveguides in 2D PCs. Among the several waveguide designs that have been studied, the most common ones are the  $W_n$  waveguides and their variants - where  $n$  is the width of the waveguide in terms of pore rows - and the coupled-cavity waveguide. The latter consists of a chain of cavities placed periodically and close enough to each other to couple to the neighboring ones [48, 49, 50]. The overlap of the confined cavity modes induces photon hopping, which leads to light propagation. The  $W_n$  waveguide is formed by changing the pore radius of  $n$  pore lines or removing them completely. Most efforts are carried out on W1-based (or even narrower) waveguides, because they are single-mode in a large frequency range within the band gap [51, 52, 53]. However, they show several disadvantages in terms of coupling issues and high propagation losses, especially in the case of PPCs. In contrast, larger waveguides like W3 or W5 are multi-mode with much lower coupling- and propagation losses [54, 55].

To remind of the basic waveguide properties, we will concentrate on the simple case of a W1 waveguide consisting of one row of missing pores in the  $\Gamma$ -K direction. This design will be considered again in chapter 3.

The introduction of a line defect induces a symmetry breaking, since the translation symmetry exists only in the direction parallel to the defect. Therefore, the new Brillouin zone is one-dimensional, and the band structure of the 2D PC has to be projected onto the  $k$ -path  $\Gamma$ -J of the new Brillouin zone [52, 56], where the J-point is at the edge of the Brillouin zone (corresponding to  $k = \pi/a$ ). Fig. 1.9 shows the band structure for TE modes of the W1 waveguide consisting of a row of missing pores in the  $\Gamma$ -K direction, the PC consisting of a hexagonal lattice of air pores in silicon with relative radius  $r/a = 0.366$ . The band structure for the corresponding bulk PC has already been presented in fig. 1.6. The grey regions in fig. 1.9 correspond to the continuum of projected bands of the bulk PC. The comparison with fig. 1.6 shows that there is a TE band gap in the normalized frequency region from 0.231 to 0.355, where several defect states are located. However, not all of these defect states are guided due to the presence of the photonic band gap. In such a structure, two guiding mechanisms coexist [56]. The first mechanism

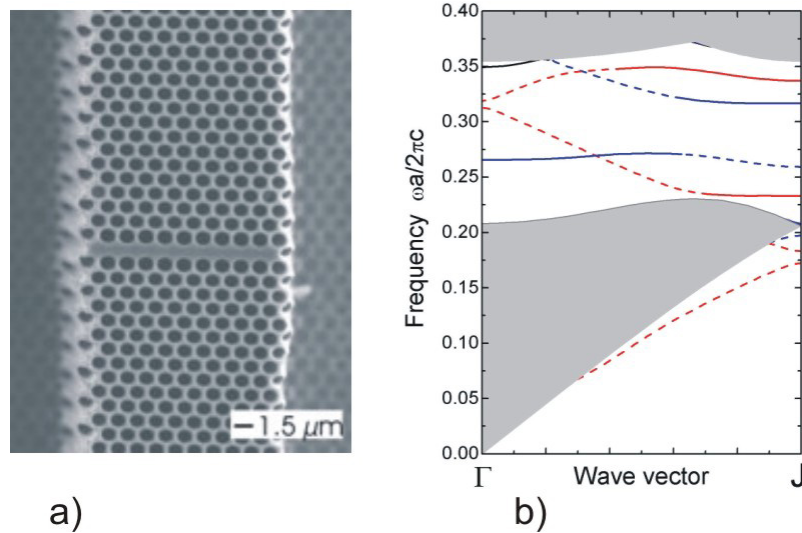


**Figure 1.9:** a) Scanning Electron Microscope (SEM) picture (courtesy of A. Birner) and b) band structure for the TE polarization of a linear waveguide in a 2D PC. The band structure has been calculated for a PC consisting of a hexagonal lattice of air pores in silicon with relative radius  $r/a = 0.366$ . The linear defect is made of a row of missing pores in the  $\Gamma$ -K direction. The defect modes are sorted into index-guided (dashed lines) and photonic-band-gap guided modes (solid lines) as well as into laterally odd (red lines) and even modes (blue lines). Due to interactions between the bands having the same symmetry, the guiding mechanism of the bands can change (MIT package calculation [47]).

is based on the existence of the photonic band gap, and the second one is the classical index guiding due to the effective index contrast between the waveguide and its surrounding.

Since their existence is based on the index contrast, index-guided modes (dashed lines) exist below the first band of the bulk PC. When they reach the J-point at the limit of the first Brillouin zone, they are folded back and continue to increase in the direction of the  $\Gamma$ -point. Fig. 1.10 shows a comparison between the field distributions at the J-point of the two index-guided modes of fig. 1.9 and those of the corresponding 2D ridge-waveguide having the same width and the same effective indices in core and cladding as the photonic crystal waveguide. There is a good agreement between the fields of both systems, taking into account that the index-guided modes inside the PC waveguide are perturbed by the periodicity of the pores, which leads to the stop gap between the modes at the J-point.

Unlike the index-guided modes, the photonic-band-gap-guided modes (solid lines in fig. 1.9) exist only within the band gap of the PC. Their guiding mechanism is based on the absence of allowed states in the surrounding PC, and therefore presents a metallic-like behavior. Furthermore, in contrast to index-guided modes, they exist also in waveguides, where the core has a lower effective index as the surrounding PC [52]. Fig. 1.11 shows the  $H_z$ -field distributions of the three lowest photonic-band-gap-guided defect modes at the J-point having normalized frequencies  $\omega a/2\pi c = 0.233, 0.317$  and  $0.337$ , respectively.

As can be noticed in fig. 1.9, index-guided and photonic-band-gap-guided modes of the same symmetry interact when approaching each other, resulting in avoided crossings. It means that the distinction claimed between index- and band-gap guidance is not always rigorous. Moreover, it is possible to combine both by inserting a slab waveguide in the middle of a PC [52, 57]. However, for the coupling of light from an external waveguide into a PC waveguide, the guiding mechanism plays an important role, as will be discussed in chapter 3.

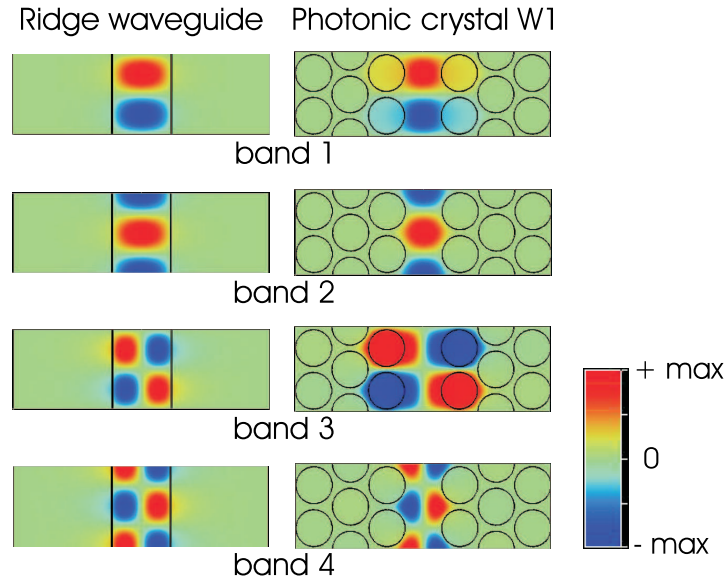


**Figure 1.10:** Comparison between the  $H_z$ -field distributions at the J-point of the four lowest indexed modes in the PC waveguide presented in fig. 1.9 (right) and in the corresponding ridge waveguide (left) having the same width and the same effective indices in the core ( $\varepsilon = 3.4$  for silicon) and the claddings ( $\varepsilon = 1.55$  for the system silicon/air pores with  $r/a = 0.43$ ). This  $\varepsilon$  value was determined considering the inverse of the tangent of the fundamental bulk mode at the  $\Gamma$ -point in the corresponding band structure). The black lines on the left mark the silicon core of the ridge waveguide while the black circles on the right indicate the position of the air pores of the PC (MIT package calculation [47]).

### 1.3.3 Photonic Crystals-Based Dispersion Compensators

To obtain high absolute negative dispersion, a very low group velocity within the PC devices has to be achieved. This can be obtained either in a coupled-cavity waveguide (CCW) or at the band edge of a mini-stopgap of a  $W_n$  waveguide. Up to date, very few DCs based on PCs have been reported in the literature, and all of them were based on CCWs. In 2002, Hosomi *et al.* [58] predicted that a waveguide based on coupled cavities in a square lattice had dispersion properties suitable for dispersion compensation. A similar study in the case of the hexagonal lattice was published a few months later by Martínez *et al.* [59]. This type of waveguide can yield a linear negative dispersion of about 10 ps/nm/mm in the wavelength range  $1550 \text{ nm} \pm 5 \text{ nm}$ . This is four orders of magnitude larger than the dispersion achieved in DCFs. First experimental results by Chai and coworkers [60] seem to confirm these predictions.

The coupling strength of the cavities in CCWs can be described by following an analogy to the tight-binding theory used in solid-state physics. Provided that the interactions between cavities occur only between neighboring defects along the waveguide, the dispersion relation of an infinitely long CCW can be expressed as [58, 59]:

$$\omega(k) = \Omega[1 + \kappa \cos(k\Delta)] \quad (1.14)$$

where  $\Omega$  is the angular eigenfrequency of an isolated cavity,  $\Delta$  the distance between two consecutive cavities, and  $\kappa$  the coupling constant, i.e., the parameter representing the overlap of the field distributions of two neighboring cavities. With a little algebra, this finally leads to the

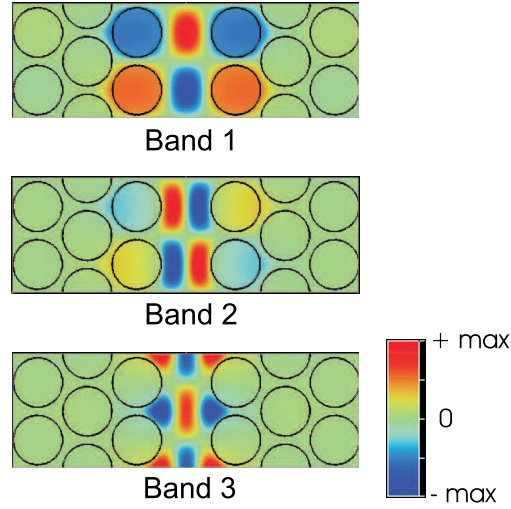


**Figure 1.11:**  $H_z$ -field distributions of the three lowest photonic-band-gap-guided defect modes of the W1 waveguide presented in fig. 1.9. The black circles indicate the position of the air pores of the PC (MIT package calculation [47]).

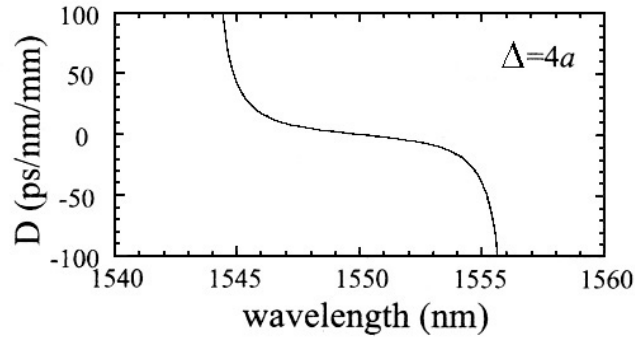


**Figure 1.12:** Dispersion of a coupled-cavity waveguide in a square lattice of silicon rods in air. Each cavity consists of a missing rod and the distance  $\Delta$  between two neighboring cavities is  $4a$  (by Hosomi *et al.* [58]).

following relation for the dispersion parameter  $D$ :

$$D = \frac{d(v_g^{-1})}{d\lambda} = \frac{1}{2\pi c\Delta} \eta(\eta + 1)^2 (\kappa^2 - \eta^2)^{-3/2} \quad (1.15)$$

where  $\eta = (\lambda_0/\lambda) - 1$  and  $\lambda_0$  is the resonance wavelength of the cavity. The resulting negative dispersion slope is very smooth and has an antisymmetrical shape with an almost linear region in its center, as illustrated in fig. 1.12. However, this derivation assumes that all the cavities have the same resonance wavelength  $\lambda_0$ . In realistic devices containing hundreds of coupled cavities, there will be tolerances in the precision due to the device fabrication. Whereas the transmission in the ideal case should be 100 %, off-resonance propagation in a resonant structure leads to significant losses, back reflections, and coupling problems.

In addition to these experimental limitations, DCs based on CCWs show two further major disadvantages. First, the dispersion slopes are always quite similar, because light propagation is

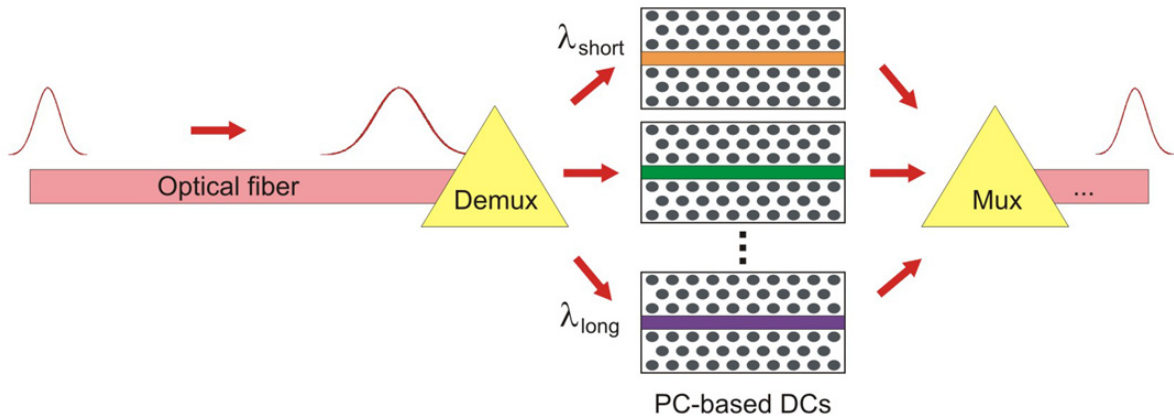


**Figure 1.13:** Schematic diagram of a PC-based DC with a WDM system.

based on the tight-binding mechanism. Therefore, a fine adjustment of the dispersion properties to the desired slope is quite difficult, despite the large flexibility in cavity design. The second problem encountered with CCWs is the possible high radiation loss. Since the wave vector range suitable for dispersion compensation is in the middle of the  $k$ -path, the device always works above the light line. Although the radiation losses in CCW-based DCs have not been quantified yet, we expect them to be non-negligible.

Therefore, to design DCs with low propagation losses and high flexibility in the dispersion slope, we choose  $Wn$  waveguides as our system of interest, which have never been investigated for applications to dispersion compensation. Unlike the case of CCWs, the principle of low group velocity inside  $Wn$  waveguides is based on Bragg scattering. Bragg scattering occurs either because the wave is scattered at the corrugations of the PC waveguide, or because this latter mode interferes with another mode of the same symmetry, creating a mini-stopgap. This configuration is a non-resonant situation since the low group velocity is an effect of the onset of interference. Very low group velocity can be achieved in the vicinity of a mini-stopgap or at the band edge. Consequently, a carefully chosen design should yield a band suitable for dispersion compensation below the light line, close to the edge of the first Brillouin zone, allowing lossless light propagation. Note that in the case of  $Wn$  waveguides the dispersion slope may vary very strongly with any small change in the design or the material parameters. On one hand, this is much more challenging; but on the other hand, this feature may open the door to DCs with high tuning ability.

### 1.3.4 Requirements

For the design of the PC-based DCs, some basic requirements must be considered, which are elucidated point by point as follows:

1. Light has to be guided in the vertical direction within the waveguide to reduce intrinsic losses as much as possible. Furthermore, the device must be integrated into a chip, and compatible with other integrated optical devices [61], such as a PC-based wavelength demultiplexer that should separate the incoming optical signal from the SMF into single-wavelength channels before dispersion compensation, as illustrated in fig. 1.13. The system fulfilling both requirements is a 2D PPC. Although the principle of a DC based on a  $Wn$  PPC waveguide is clear, the intrinsic properties of PPCs have to be well understood for a precise control of the device

functionality. Therefore, in chapter 2, after selecting the material system, the properties of the bulk PPC will be studied in detail.

2. In chapter 3, we will focus on the design of the DC, including the selection of a preliminary waveguide design suitable for dispersion compensation, and some improvements to satisfy the requirements on low propagation losses. We will also present different ways of tuning the material properties to vary the relevant dispersion. Concerning the coupling issues, which are crucial for the device functionality, we will address them at the end of chapter 3. Most importantly, we will propose new solutions for a better coupling of light into the PC, leading to the development of a complete design of an integrated functional DC.

3. In chapter 4, we will finally discuss the experimental fabrication of such a device using dry etching techniques. An insight into the full process, including lithography, mask deposition and opening, and structuring of the different layers by plasma etching, will be the main topic of this chapter.

## 2. Study of the Bulk Photonic Crystal Slab

The aim of the work presented in this chapter is the study of the properties of the bulk planar photonic crystal (PPC). A complete understanding of the PPC behavior is necessary to design a reliable device. Therefore, after selecting a material system, the influence of the different geometric parameters on the PPC properties will be discussed. We will also show that quite unexpected intrinsic properties of the PPC may have significant consequences on the device functionality, confirming that a very careful 3D study of the PPC behavior is necessary.

### 2.1 Selection of the Material System

Since 2D photonic crystals cannot provide light confinement in the direction parallel to the pore axis, a way to avoid out-of plane losses is the use of PPCs. PPC structures consist of a thin 2D photonic crystal (core) surrounded by two layers of lower effective refractive index (claddings) that provide an index guiding by total internal reflection in the direction normal to the plane of the crystal, as in a planar waveguide. Different examples of PC slabs are shown in fig. 2.1. The first one, the so-called "air-bridge" structure, has already been extensively studied [51, 62]. It consists of a thin 2D PC in a high-index membrane surrounded by air (fig. 2.1a). In this case, the index contrast between core and cladding is very high and light is strongly confined within the core. However, this type of suspended structure can not be easily integrated into a chip.

The second example (fig. 2.1b) is a PC slab made in a heterostructure, usually consisting of III-V semiconductor materials. In this case, the index-contrast between core and cladding is low, and the mode profiles are quite extended, such that the pores should penetrate deeply into the cladding layers [63, 64]. Due to limitations associated with the fabrication processes, this type of PPC has usually only a very thin upper cladding, yielding an asymmetrical mode profile. This mode-profile asymmetry is often partly compensated by choosing a lower-cladding material with a lower dielectric constant than that of the upper cladding, in order to avoid strong additional losses.

The third type of structure (fig. 2.1c) is a hybrid case often found in SOI-based systems [53, 62, 65]. The lower cladding usually consists of an oxide layer, not necessarily structured, while in most cases the upper cladding consists of air only. Although this PC can be integrated into a chip more easily than a membrane, the asymmetry of the mode profile within the structure may lead to additional losses, as in system b). In the case of a structured oxide layer, the effective refractive index in the cladding is close to 1. Therefore, the structure turns out to be simultaneously easily integrated and almost symmetrical. The ideal structure would be a system with two structured oxide claddings, leading to integrability, high light confinement, and perfectly symmetrical mode profiles all at the same time (fig. 2.2). Furthermore, the presence of the two structured claddings with low index should lead to low scattering losses from an experimental point of view. Indeed, even if Bloch modes are theoretically guided and lossless, the experimental structures are never perfect and scattering losses always occur due to irregularities, (e.g., the roughness of the pore walls). Such losses are expected to be smaller in structures

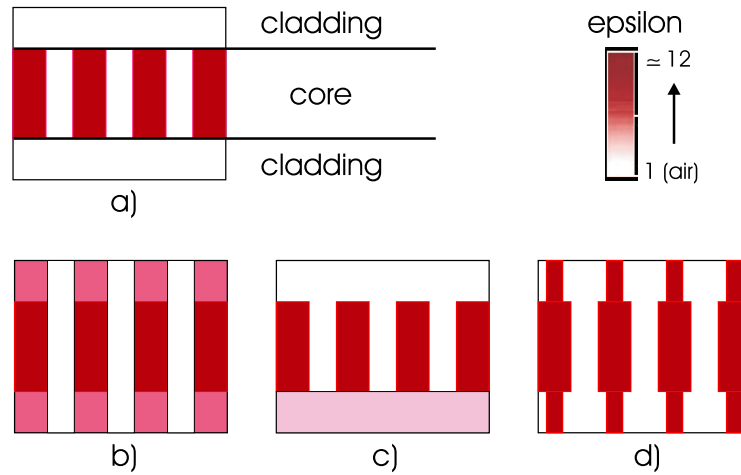


**Figure 2.1:** Four examples of PC slabs (side view): a) air-bridge structure with high index contrast between core and cladding, e.g., Si membrane, b) low-index contrast heterostructure, e.g., AlGaAs/GaAs/AlGaAs system, c) asymmetrical structure with two different claddings, commonly based on the SOI system, usually with an upper air cladding, and d) modulated-pores structure achieved, e.g., in macroporous silicon.

with high vertical index contrast [66], such as SOI-based PPCs. However, the structuring of high-aspect-ratio silicon oxide at a submicron scale remains a challenge, suggesting that this type of system with two structured oxide claddings is very difficult to fabricate.

The above three examples commonly have the effective index contrast between core and cladding being obtained by taking another material to build the claddings as in the core. In the last case (fig. 2.1d), the effective index contrast is obtained by modulation of the pore diameter in the same material. In the cladding, the air filling fraction is higher, and the effective refractive index is thus lower. This kind of structure can be obtained in macroporous silicon [67] and offers a large degree of freedom concerning the pore modulation and depth. However, large modulations cannot be achieved very easily, indicating that this type of PPC has a limited index variation between core and cladding, giving rise to properties similar to case b).

Therefore, the insulator-on-silicon-on-insulator (IOSOI) system shown in fig. 2.2 is the most promising design for future applications, because it allows the integration of the PPC onto a chip and offers simultaneously the possibility to have a symmetrical mode profile and limited radiation losses. Furthermore, this structure could be realized at low cost via the standard silicon technology. Taking these features into account, we select the IOSOI structure with two structured claddings as our material system of interest to build the PPC-based DCs.

## 2.2 Effects of the Vertical Confinement

### 2.2.1 Higher-Order Modes

Since PPCs are a combination of 2D PCs and planar waveguides, they support modes of different orders, as illustrated in fig. 2.3, taking an IOSOI PPC with relative silicon thickness  $h/a = 0.65$  and relative pore radius  $r/a = 0.46$  as an example. The first-order modes are the

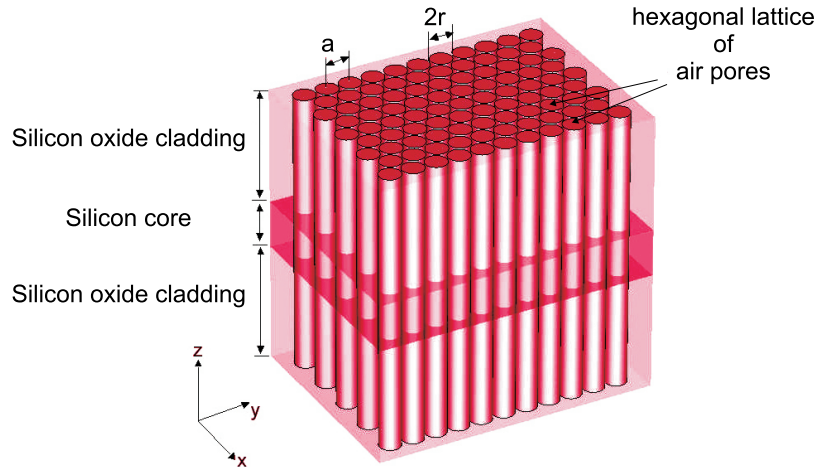


**Figure 2.2:** PC slab consisting of a silicon core and two structured silicon oxide claddings (insulator-on-silicon-on-insulator (IOSOI) structure) with air pores arranged in a hexagonal lattice.

fundamental modes, without nodes in the vertical direction. In fig. 2.4, the  $H_z$ -field distributions of the two lowest first-order TE-like bands at the M-point are compared with the corresponding field distributions of an infinite 2D PC. These modes are highlighted in fig. 2.3 by red and blue circles, respectively. It can be seen that the  $H_z$ -field is localized within the silicon slab, decreasing exponentially toward the claddings. Within the silicon, the field distributions of the PPC are very similar to those of the corresponding infinite 2D PC.

As in the case of planar waveguides, higher-order modes with nodes in the vertical direction also exist in the PPC, having cutoff frequencies decreasing with the increase in the slab thickness or in the dielectric contrast between core and cladding. Their field distributions in the  $(x,y)$ -plane in the middle of the slab are quite similar to the field distributions of the corresponding first-order modes. However, they may become more complicated with moving in the  $z$ -direction. Their interactions with the first-order modes can lead to radical changes in the band structure compared to the corresponding infinite 2D PC, as illustrated in fig. 2.3. In fig. 2.3, the slope of the lowest bands is very similar to that of the corresponding bands in the infinite 2D case, except for a shift toward higher frequencies due to the vertical confinement. The lowest second-order TE-like mode appears at the  $\Gamma$ -point at a relative frequency of 0.73, and decreases very strongly toward the M and K points. This mode is highlighted by the orange circle in fig. 2.3 and its  $H_z$ -field distribution with the two vertical nodes is presented in fig. 2.5. An interaction between this lowest second-order mode and the second first-order mode results in the notable feature observed along the M-K-path for frequencies around 0.55. For higher frequencies, the number of higher-order modes increases and the band structure becomes very complicated.

Although the existence of higher-order modes is well known, their nature and potential influence on the PPC properties have not been well addressed yet in the literature. Therefore, a more detailed study of the consequences of the presence of higher-order modes will be given later in this chapter.

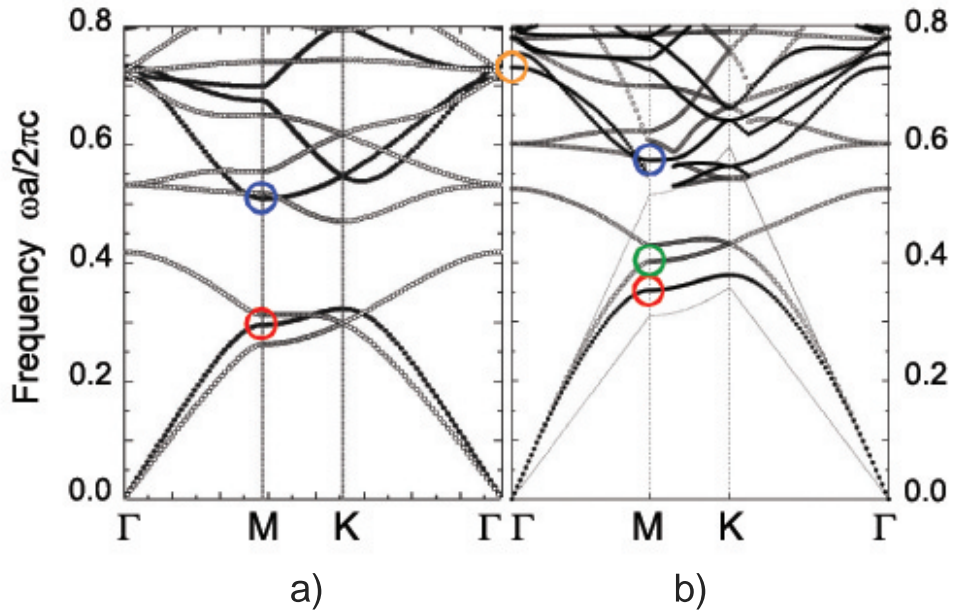


**Figure 2.3:** Comparison between the band structures of TE-like modes (black dots) and TM-like modes (open circles) of a) an infinite 2D PC of air pores in silicon and b) a PPC consisting of a silicon slab with relative thickness  $h/a = 0.65$  and two structured oxide claddings. In both cases, the air pores are arranged in a hexagonal lattice with a relative radius  $r/a = 0.46$ . The colored circles indicate the modes having their field distributions presented in fig. 2.4 - 2.6. The band structures were calculated using the MIT package [47] in case a) and a 2D effective plane-wave method by L.C. Andreani [68] in case b).

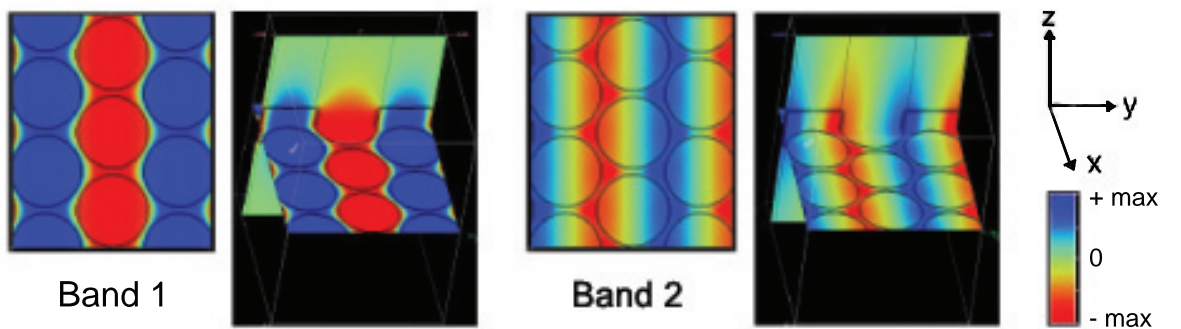


**Figure 2.4:** Comparison between the field distributions at the M point of the first (left) and second (right) TE modes of the infinite 2D PC (horizontal cross section) and the corresponding first-order TE-like modes of the PPC presented in fig. 2.3 (horizontal  $((x,y)$ -plane) and vertical  $((y,z)$ -plane) cross sections). The black circles and the vertical lines indicate the position of the air pores, and the horizontal black lines indicate the position of the silicon slab. The modes are highlighted in fig. 2.3 by red and blue circles, respectively (MIT package calculations [47]).

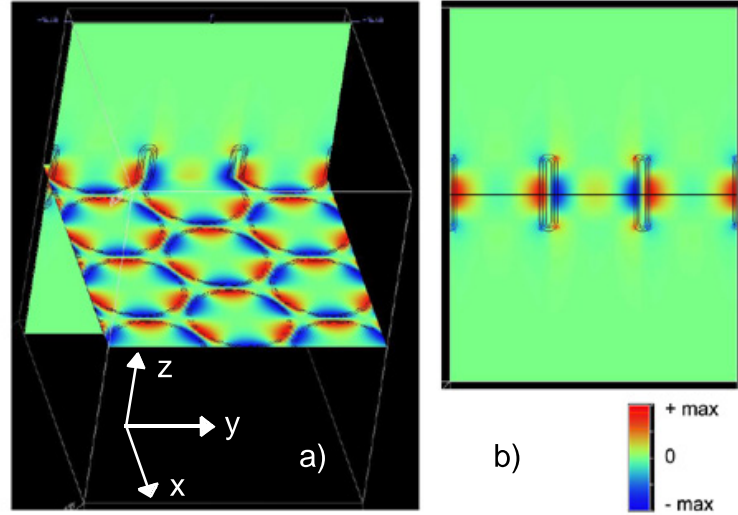


**Figure 2.5:**  $H_z$ -field distribution of the lowest second-order mode at the  $\Gamma$ -point for the band structure presented in fig. 2.3b. a) Horizontal and vertical cross sections, and b) vertical cross section only. The black circles and the vertical lines indicate the position of the air pores, and the horizontal black lines indicate the position of the silicon slab. The mode is highlighted in fig. 2.3 by an orange circle (MIT package calculation [47]).

## 2.2.2 Polarization Mixing

Because of the finite height of the structure, polarization mixing occurs and the modes are not purely TE (resp. TM)-polarized anymore. On the other hand, if the  $(x,y)$ -plane in the middle of the slab is a mirror plane of the structure, i.e., if both claddings are identical as in the case of the IOSOI system, the modes can be separated into vertically even (with their  $H_z$  and  $E_{xy}$  components having symmetrical field distributions with respect to the mirror plane) and odd modes (antisymmetrical field distribution). Fig. 2.6 illustrates the symmetry property of the modes, taking the  $H_z$ -field component of the two lowest modes shown in fig. 2.3b at the M-point as examples. The lowest mode (indicated by a red circle) has a symmetrical  $H_z$ -field distribution, and therefore, is designed as even mode. The second mode, highlighted by a green circle in fig. 2.3b, has an antisymmetrical  $H_z$ -field distribution, and therefore, is designed as odd mode.

It has been shown that, in the  $(x,y)$ -mirror plane itself, the modes are purely TE (resp. TM)-polarized [69]. Therefore, the approximation that even modes are TE-polarized and odd modes are TM-polarized is often made. Consequently, the terminologies TE (or H) and TM (or E) modes are often found to refer to even and odd modes, respectively. However, this is true only for first-order modes, and only in the mirror plane itself. Moving away from the center of the slab, a non-zero  $E_z$ -field (resp.  $H_z$ -field) component appears for TE-like (resp. TM-like) modes, clearly indicating a polarization mixing.

Here, we should point out that up to date no complete band gap for all in-plane directions has been found in odd modes of PPCs with high vertical index contrast and a hexagonal lattice [68]. In the rest of this study, we will thus pay our attention only to modes with vertically even symmetry with respect to the  $(x,y)$ -plane in the middle of the silicon core. The absence of a complete band gap for both mode symmetries should not lead to any additional loss as long as the PPC structure is completely symmetrical. Since incoming TE-polarized light has an

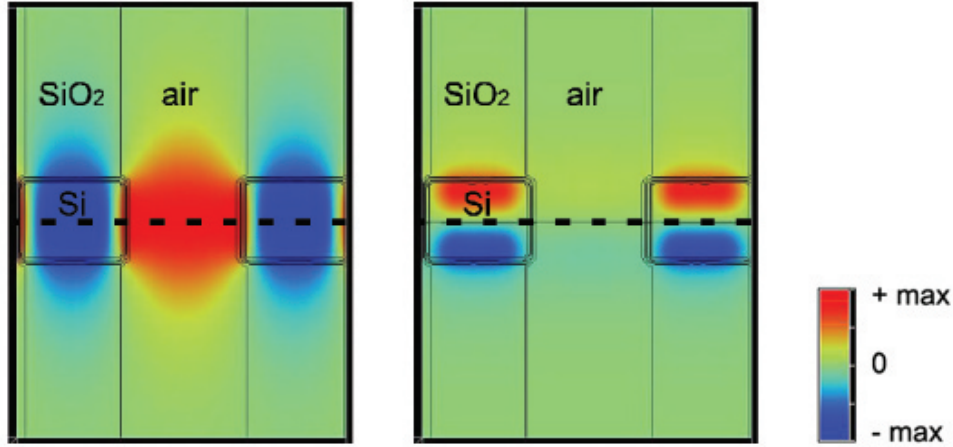


**Figure 2.6:**  $H_z$ -field component of the two lowest modes in the PC slab presented in fig. 2.3b at the M point (the modes are highlighted in fig. 2.3b by a red and a green circles, respectively). If we consider the (x,y)-mirror plane in the middle of the core layer, indicated by the dashed line, the first band (left) has a vertically even symmetry and the second one (right) a vertically odd symmetry. The non-zero  $H_z$ -field component in the case of the odd (i.e., TM-like) mode indicates a small proportion of TE polarization for this mode, and is a sign for the polarization mixing that occurs in PPCs (MIT package calculation [47]).

even symmetry, it can excite only vertically even modes. From an experimental point of view, however, PPC structures are often asymmetrical with respect to the (x,y)-plane in the middle of the slab. For instance, the upper cladding is usually thinner than the lower one, or missing, mainly due to fabrication limitations. Even if the symmetry breaking is small in SOI-based systems [70], some odd-like modes may be slightly excited by an incoming TE-polarized wave. This may lead to losses or non-zero transmission within the even band gap.

The gap map representing the frequency dependence of the even modes as a function of the relative radius of the pores for an IOSOI PPC with relative core thickness  $h/a = 0.4$  is given in fig. 2.7. Compared to fig. 1.7, fig. 2.7 shows that the largest gap-midgap ratio is smaller and is obtained for slightly smaller relative radius values for the IOSOI PPC (39 % for  $r/a = 0.41$ ) than for the infinite 2D case (50 % for  $r/a = 0.43$ ). The difference in the optimum radius may be explained by the finite core thickness in the PPC. Due to the small penetration of the fields into the claddings, the average effective index seen by the modes is slightly lower in the PPC than in the infinite 2D case. This effect may be compensated by a smaller pore radius. The smaller gap size is probably a consequence of the polarization mixing. Since the non-zero  $E_z$ -field is concentrated mostly in the low-index regions for both bands, the energy gap between them may be lower than that of the infinite 2D case having a zero  $E_z$ -field component.

### 2.2.3 2D-3D Transition

The core thickness plays a crucial role in the properties of PPCs. If the thickness of the core approaches zero, the PPC constitutes only a small perturbation of the cladding system. Therefore, the band structure is very close to the 2D band structure of the cladding system - in our case an hexagonal array of air pores in silicon dioxide, as presented in fig. 2.8a. If the core thickness increases, (fig. 2.8b), the PPC cannot be considered as a perturbation anymore. The system

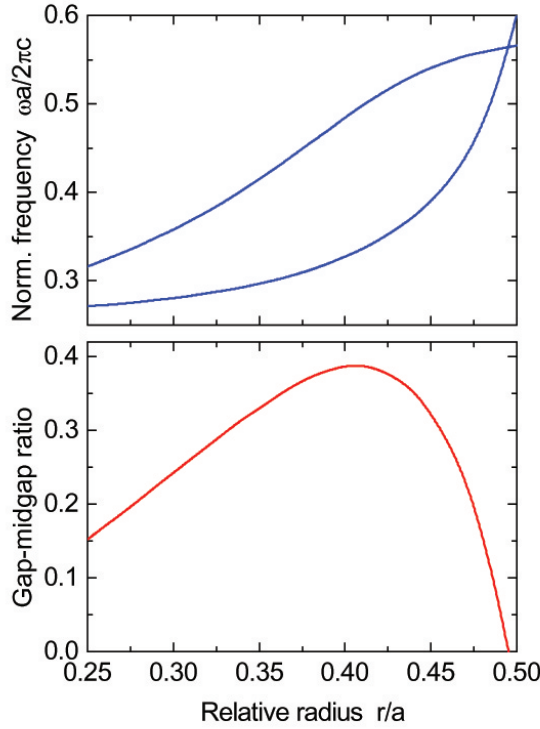


**Figure 2.7:** Upper panel, the gap map (variation of the band gap frequencies with the relative pore radius) of the IOSOI PPC with relative core thickness  $h/a = 0.4$ . Lower panel, the variation of the gap-midgap ratio. Only the modes with vertically even symmetry are shown (MIT package calculation [47]).

shows a full 3D behavior, i.e., higher-order modes appear at high frequencies. Due to the higher average dielectric constant of the PPC, the frequency of the bands decreases. With further increasing of the core thickness, the cutoff frequency of the higher-order modes decreases very fast. Meanwhile, the modes become more numerous and closer to each other, suggesting that the interactions between modes become stronger. This characteristics results in the very flat bands presented in fig. 2.8c. For very thick slabs (having thicknesses larger than  $20a$ ), the band structure tends to become continuous, and the first-order modes converge towards the limiting case of the infinite 2D PC of air pores in silicon (fig. 2.8d).

## 2.2.4 Planar Waveguide Approximation

For thick slabs, higher-order modes can exist within the first-order band gap of the PPC. If these modes happen to have the appropriate symmetry properties to be excited by an incoming light beam, they can limit the band gap or even destroy it completely. Reducing the effective vertical index contrast  $\Delta n$ , the cutoff frequencies of the higher-order modes increase. A first guess to determine the cutoff frequency of the lowest second-order mode is to use the planar waveguide approximation. In this very simple approximation, we calculate the cutoff frequency of the second mode in a planar waveguide where each layer has the same effective refractive index as the PPC, using the following relation:

$$\frac{h}{\lambda_0} = \frac{1}{2 \cdot \sqrt{n_2^2 - n_1^2}} \quad (2.1)$$

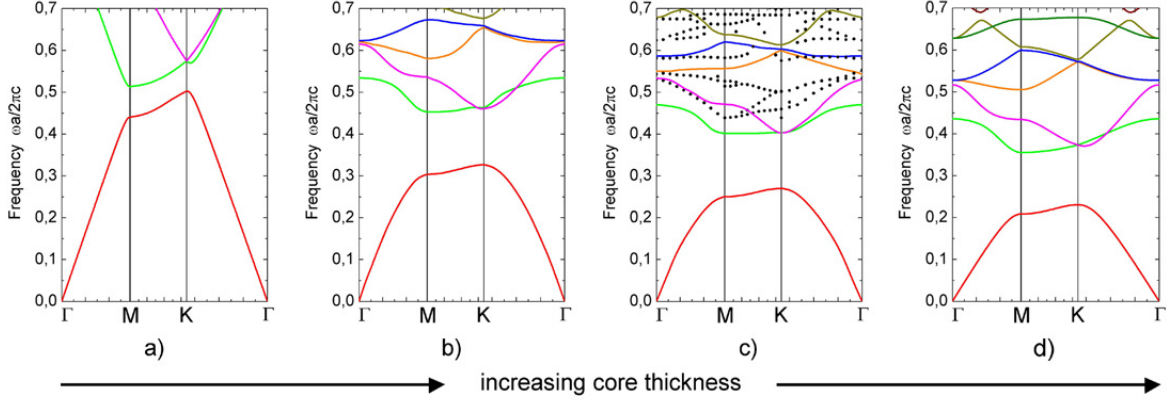


**Figure 2.8:** Variation of the band structure with the silicon thickness of an IOSOI-based PC slab with relative radius  $r/a = 0.366$  and two infinite structured oxide claddings. a) Limiting case of an infinite 2D photonic crystal made of a hexagonal lattice of air pores in silicon dioxide, b) IOSOI-based PC slab with relative core thickness  $h/a = 0.3$ , c) IOSOI-based PC slab with relative core thickness  $h/a = 0.75$ , and d) limiting case of an infinite 2D photonic crystal made of a hexagonal lattice of air pores in silicon. The two limiting cases, a) and d), correspond to a core thickness equal to zero and infinity, respectively. The colored lines show the first-order modes, which correspond to the modes existing in the infinite 2D cases. Higher-order modes are shown by black dots. The band structures were determined combining the results of the MIT package [47] and FDTD calculations by C. Hermann and O. Hess [71].

where  $h$  is the thickness of the core,  $\lambda_0$  the cutoff wavelength, and  $n_1$  and  $n_2$  the effective indices in the claddings and in the core, respectively, and for a PPC:

$$\frac{h}{\lambda_0} = \frac{h}{a} \cdot \frac{a}{\lambda_0} \quad (2.2)$$

with  $h/a$  being the relative thickness of the slab and  $a/\lambda_0 = \omega_0 a/2\pi c$  the normalized cutoff frequency of the mode. To determine the effective refractive indices of the different layers constituting the PPC, we consider the light line (i.e., the lowest band) of the 2D systems corresponding to core and claddings, respectively, and then take the inverse of its tangent at the  $\Gamma$ -point. Indeed, in the long-wavelength limit, the photonic crystal can be regarded as an effective medium with average dielectric constant. Taking the IOSOI PPC ( $\varepsilon_{Si} = 11.6$ ,  $\varepsilon_{SiO_2} = 2.1$ ) with a relative radius  $r/a = 0.366$  as an example, the effective refractive indices are  $n_2 = 2.57$  in the core and  $n_1 = 1.25$  in the claddings. This leads to a cutoff frequency of  $\omega_0 a/2\pi c = 0.56$  for the first second-order mode, in the case of a relative silicon thickness  $h/a = 0.4$ . The corresponding band structure is presented in fig. 2.9. It can be seen on the band structure that the lowest second-order mode has a cutoff frequency around  $\omega_0 a/2\pi c = 0.57$ , that is very close to the value calculated using the planar waveguide approximation. Therefore, this very simple method gives already a good guess of the cutoff frequency of higher-order modes in photonic crystal slabs. However, this approximation is valid only for slabs that are thin enough for the bands to be quite unperturbed. With increasing slab thickness, the bands are getting closer and more numerous, and the number of interactions between them increases, leading to perturbations of the band structure and variations of the mode positions.

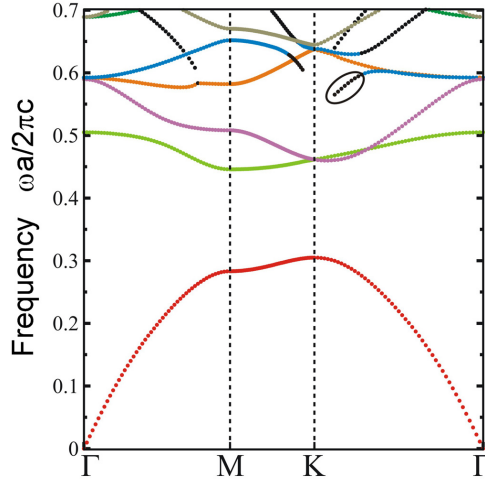


**Figure 2.9:** Band structure for even modes of the IOSOI PPC with a relative core thickness  $h/a = 0.4$  and two structured oxide claddings. The relative radius of the pores is  $r/a = 0.366$ . The colored lines show the first-order modes, and the black dots the higher-order modes. The lowest higher-order mode is highlighted by a black circle (2D effective plane-wave calculation by L.C. Andreani [68]).

## 2.2.5 Selection of the Slab Thickness

Fig. 2.10 presents the gap map depending on the relative core thickness for an IOSOI PPC having a relative radius  $r/a = 0.366$ . The red and blue curves show the variations of the two lowest first-order modes, i.e., the modes limiting the band gap in the infinite 2D case. The green curve indicates the cutoff frequency of the lowest second-order mode having a laterally odd symmetry. The frequency of this mode decreases much faster with increasing core thickness than that of the first-order ones. While entering the band gap at the M point, it interacts with the second first-order mode and shifts this mode up to higher frequencies, resulting in the small feature observed for relative thicknesses around  $h/a = 0.95$ . For larger thicknesses, the band gap is then limited from the top by this second-order mode. Fig. 2.11 presents the  $H_z$ -field distribution of this mode at the M-point. As can be recognized from its in-plane field distribution, it has a clear origin in the fundamental TE-polarized mode from the infinite 2D case. It has to be noticed that this mode is not the lowest second-order mode. Some other modes exist with lower cutoff frequencies, as could be deduced from the planar waveguide approximation. However, they are not taken into account because they do not have the proper symmetry to disturb the fundamental band gap of the PPC. Indeed, light incident from an external source (e.g., plane wave), has a laterally odd symmetry, which correspond to laterally even  $H_z$ -field distribution, since always the  $E_{\parallel}$  or  $H_{\perp}$ -field components have to be considered to define the mode symmetry. Therefore, only higher-order modes with laterally odd symmetry can be excited and are of importance.

If we consider the fundamental band gap for the first-order modes at very small core thicknesses (tending to zero), we can verify that it converges towards the band gap of the infinite 2D system of air pores in silicon oxide, constituting the claddings. The band structure for this system has been shown in fig. 2.8a. At the other end of the gap map, the band gap for first-order modes converges towards that of the infinite 2D system of air pores in silicon, constituting the core, as can be verified comparing with fig. 2.8d.

As a conclusion of this section, we choose to work with a silicon thickness  $h/a = 0.3-0.5 a$ . Indeed, as can be recognized in fig. 2.10, the gap size for this relative thickness is very large (above 35 %) and the cutoff frequency of the lowest second-order mode of importance is quite

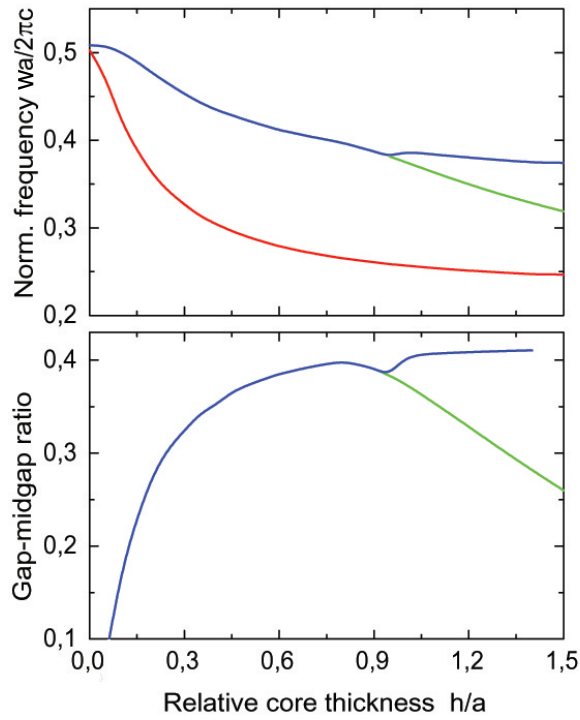


**Figure 2.10:** Upper panel, the gap map (variation of the eigenmodes frequency  $\omega a/2\pi c$  with the relative core thickness  $h/a$ ), and lower panel, the gap size of the IOSOI-based PC slab having a relative radius  $r/a = 0.366$ . The red and blue lines show the variations of the first and second first-order modes, respectively, and the green line shows the cutoff frequency of the lowest second-order mode (MIT package calculation [47]).

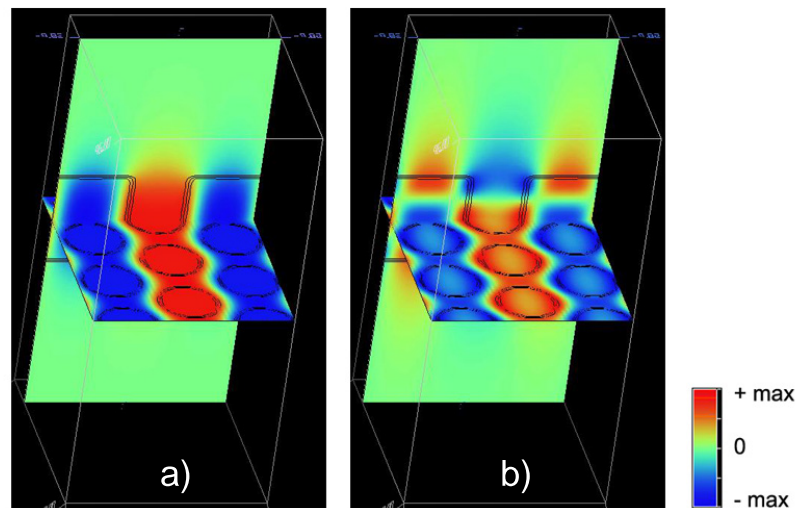


**Figure 2.11:** Comparison between the  $H_z$ -field distribution of a) the lowest first-order mode and b) the lowest second-order mode having a laterally odd symmetry at the M point. Both modes originate in the fundamental TE-polarized mode from the infinite 2D case. The IOSOI-based PPC considered has a relative radius  $r/a = 0.366$ . In the case of thin slabs, the band gap is limited from above at the M point by the second first-order mode. For thicker slabs the band gap is limited by the second-order mode (MIT package calculation [47]).

high. Working with larger thicknesses up to  $0.8 a$  would not bring any significant improvement in terms of gap size, but would enlarge the risk of having a higher-order mode within the band gap. Indeed, from an experimental point of view, the cutoff frequency of higher-order modes may be shifted toward slightly lower values, since the limitations of experimental fabrication always lead to deviations of the parameters compared to the theoretical values.

## 2.3 Light Line and Resonant Modes

In addition to the existence of higher-order modes, another consequence of the finite slab thickness of PPCs is the role of the light line. The condition of total internal reflection at the core-cladding interface, leading to pure vertical confinement of light within the core, is not fulfilled for all wave vectors. The boundary between the  $(\omega-k)$ -sets satisfying this condition and those yielding radiation losses in the vertical direction is given by the light line of the cladding system. Therefore, it is crucial for future applications to know the position of the light line, as well as to determine how strong the radiation losses are in the regions of the band structure where the condition of total internal reflection is not fulfilled. This study, which has never been performed to date for the IOSOI system, is presented in the following section.

### 2.3.1 Guided Modes and Resonant Modes

We can define the light line as the lowest band of the 2D system constituting the cladding. In the case of a symmetrical PPC system where only the band structure for even - or TE-like - modes is taken into account, the light line is the fundamental TE band of the cladding system. If the structure is asymmetrical, the absolute lowest band has to be considered, i.e., the fundamental TM band in the case of a hexagonal lattice. This is again due to polarization mixing. As illustrated in fig. 2.12, the band structure of the PPC can then be divided into two different regions. Below the light line, no state is allowed in the cladding. Therefore, the modes of the PPC, which happen to lie in this region, are totally internally reflected at the interface between core and cladding and confined within the silicon slab. These modes are pure Bloch modes, they are lossless in the case of an ideal structure where no scattering occurs. They are commonly defined as guided modes. If the PPC is symmetrical, the fundamental mode has no cutoff frequency and lies always below the light line. Consequently, the system always supports at least one guided mode. In the case of asymmetrical structures, the fundamental mode has a finite cutoff. The stronger the asymmetry, the higher the cutoff frequency of the mode. Therefore, it may happen that the lowest mode lies entirely above the light line, and no guided mode exists at all [72].

Above the light line, allowed states exist in the cladding. The modes lie within the light cone, i.e., the continuum of leaky modes of the planar waveguide. Due to their possible coupling with these modes, the PPC modes are defined as resonant or quasi-guided, because they have intrinsic radiation losses related to out-of-plane diffraction. Their lifetime is variable, it can be very long (weak radiation losses), but also very short (strong radiation losses) [73]. It has been shown that radiation losses for resonant modes are expected to be approximately proportional to the square of the vertical index contrast,  $(\Delta\varepsilon)^2$  [74]. In III-V-based heterostructures, intrinsic losses are thus much lower than in SOI-based waveguides. On the other hand, the amount of modes existing below the light line also depends on the dielectric contrast between core and cladding as well as on the slab thickness [12, 68]. The smaller the thickness, the less modes exist below the light line. By analogy, if the vertical dielectric contrast is low, (as it is usually the

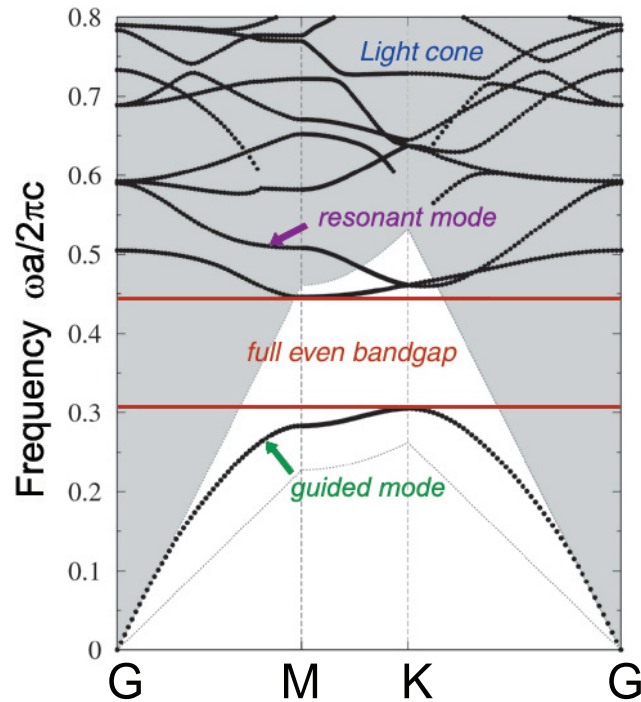


**Figure 2.12:** Band structure of a photonic crystal slab consisting of a silicon core and two structured silicon dioxide claddings (IOSOI structure) with air pores arranged in a hexagonal lattice, vertically-even modes only. The relative core thickness is  $h/a = 0.4$  and the relative pore radius is  $r/a = 0.366$ . Above the light line of the cladding system (grey region), the modes are resonant, their lifetime can be very short. Only below the light line (white region), the modes are guided and lossless. 2D effective plane-wave calculation taking as basis the eigenmodes of the corresponding planar waveguide, by L.C. Andreani [68].

case in PPCs based on III-V-semiconductor heterostructures), it is usual that the fundamental mode is the only guided mode [75]. Therefore, the band gap of such systems usually lies almost completely above the light line. If some defects are introduced into the lattice, the defect modes always have radiation losses, even if these losses are low. In contrast, in the IOSOI system, a large part of the band gap lies below the light line, as can be seen in fig. 2.12. Therefore, in this "working area" the defect modes are purely lossless and therefore suitable for waveguiding purposes. However, it is sometimes necessary to work above the light line, as will be discussed later in chapter 3 concerning the coupling issues. Thus, it is important to determine the position of the resonant modes and how strong the radiation losses are in the case of the IOSOI system. This issue is addressed in the following.

### 2.3.2 Computation of Resonant Modes

The computation of resonant modes and their radiation losses is quite difficult, and, therefore, a lot of theoretical work on photonic crystal slabs has focussed on guided modes only [12, 13]. Due to the finite height of the system, 3D calculations are necessary to calculate the band structure. However, several 3D codes - like the MIT package widely used in this work - assume a periodicity in all three dimensions, which is not convenient for a photonic crystal slab. Indeed, due to the fictive periodicity in the vertical direction, additional coupling between resonant

modes occurs. Furthermore, at the edge of the artificial vertical Brillouin zone, modes are folded back into the first Brillouin zone, disturbing completely the band structure. Therefore, only guided modes can be calculated correctly, because they do not "feel" the fictive vertical periodicity. A way to solve this problem, (also used by other groups [62]), is to calculate the band structure twice with two different supercell heights, in order to change the fictive vertical periodicity. Therefore, the amount and the frequency of the artificial modes induced by the fictive vertical periodicity are different in the two simulations. By overlapping both band structures, only the modes that really exist in the PPC are coinciding and can be selected out. Many band structures in this work were determined using this method. However, the multitude of interactions between the "real" modes of the slab and the artificial ones makes this task very difficult and time-consuming. Furthermore, only the band structure can be calculated, not the radiation losses.

There are some easier ways to determine the position of resonant modes. In the case of heterostructures with very low vertical index contrast, the band structure is quite similar to that of an infinite 2D PC having the average dielectric constant of the different layers constituting the heterostructure. Therefore, many band structures of PPCs based on III-V semiconductors are approximated by 2D simulations [76]. This approximation is not possible in the case of structures with high vertical index contrast, like our IOSOI PPC. For this system, the most commonly used method is the 3D finite-difference time-domain (FDTD) method with open boundary conditions on the top and the bottom of the structure [71, 73, 77]. This method is widely used in this study and presents the advantage to yield further information on the lifetime of the modes. Indeed, using a FDTD method, the radiation losses of resonant modes can be determined from the width of the peaks in the Fourier spectrum. The larger the peaks, the higher the losses and the shorter the lifetime of the modes. Nevertheless, this method is not without disadvantages, e.g., modes with very strong radiation losses often have very flat peaks that are not detected at all and do not appear in the simulation results, leading to incomplete band structures.

Another beautiful and fast method is to perform 2D plane-wave calculations taking as a basis the eigenmodes of a planar waveguide, where each layer has the same effective refractive index as the PPC system [68] (see fig. 2.12 for example). Since this method relies on a planar waveguide approximation, the frequency of higher modes can not be determined with high accuracy. However, it presents the advantage of fast computation and allows the simultaneous computation of the band structure and the radiation losses. Using this plane-wave method with complex frequencies, the radiation losses can be deduced directly from the imaginary part of the frequency. In the following, we will use this method to determine the radiation losses of our IOSOI PPC, qualitatively as well as quantitatively.

### 2.3.3 Determination of Radiation Losses

Fig. 2.13 shows the results of a simulation using the 2D plane-wave method with effective indices presented above, for the IOSOI PPC with relative slab thickness  $h/a = 0.4$  and relative pore radius  $r/a = 0.366$ . The X-Y plane of the 3D graph represents the variations of the real part of the frequency, depending on the wave vector, in the  $\Gamma$ -M and  $\Gamma$ -K directions (solid lines). This corresponds to the band structure already shown in fig. 2.9. Each value of the real frequency is associated to an imaginary part, which is shown along the Z-Axis (symbols). For clarity, only the three lowest bands are shown. As expected, the imaginary part of the frequency for the first band (red curve and symbols), which is below the light line, is zero. It is in agreement with the fact that guided modes are lossless. This can be verified also for the part of the second and third bands lying below the light line in the vicinity of the M and K points

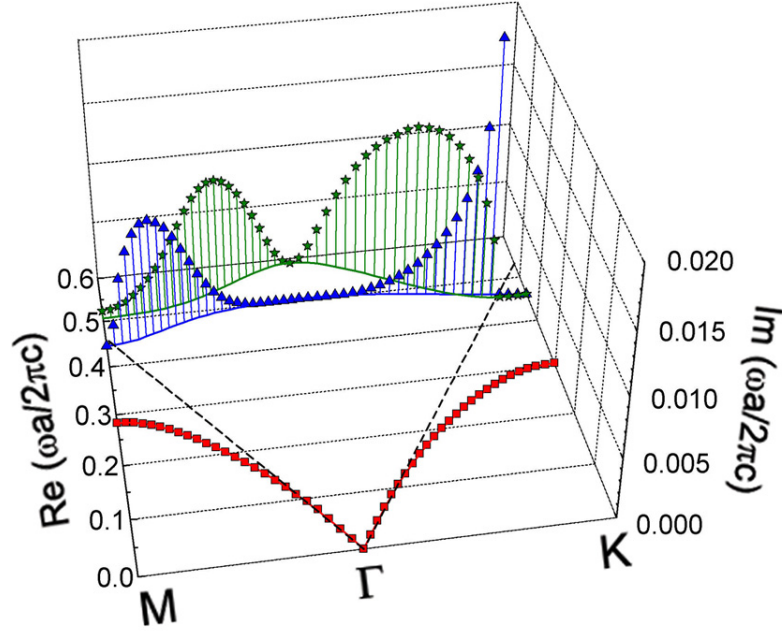


**Figure 2.13:** Band structure (real part of the frequency eigenvalues, solid lines in the X-Y plane) and intrinsic radiation losses (imaginary part, symbols along the Z-Axis) of the same PPC as in fig. 2.9. The position of the light line, delimiting the regions of guided and radiative modes in the X-Y plane, is indicated by a black dashed line. For each band, the color of the real part (solid line) and imaginary part of the frequency (symbols) is the same. For clarity, the real frequency values are connected with the associated imaginary parts by thin vertical lines (2D effective plane-wave calculation, with complex frequencies, taking as basis the eigenmodes of the corresponding planar waveguide, by L.C. Andreani [78]).

(blue and green curves and symbols, respectively). For the parts of these two bands lying above the light line, the imaginary part of the frequency varies, indicating a strong dependence of the radiation losses on the wave vector. Due to symmetry concerns, the radiation losses of bands lying above the light line are often decreasing to zero at the high-symmetry points  $\Gamma$ , M, and K [73]. This can be verified in fig. 2.13. In particular, at the  $\Gamma$ -point, only modes having the symmetry of the dipole can couple to the radiation field at normal incidence [78]. Therefore, the two higher bands shown in fig. 2.13 are lossless with an infinite lifetime at the  $\Gamma$ -point.

Considering the damping factor  $e^{-Im(\omega)t}$ , where  $Im(\omega)$  is the imaginary part of the non-normalized angular frequency and the time  $t$  may be written in the form  $a/v_g$ , the radiation losses  $L_r$  in dB per lattice constant  $a$  can be calculated:

$$L_r = 20 \log(|e^{-Im(\omega)t}|) = 20 \log(e) \cdot \left| \frac{Im(\omega a/2\pi c) \cdot 2\pi}{(v_g/c)} \right| \quad (2.3)$$

Dividing equation 2.3 by  $a$  yields the radiation losses per unit of length. Fig. 2.14 presents the radiation losses of the second and third bands shown in fig. 2.13. It can be verified again that the radiation losses decrease to zero when the modes are below the light line around the M and K-points, as well as at the  $\Gamma$ -point. The average losses for both bands are as high as  $10^3$  to  $10^4$  dB/mm and tend to infinity for the third band at the M-point, since this mode lies above the light line and its group velocity tends to zero. It has to be noticed that equation 2.3 is not mathematically valid at the high-symmetry points and should be considered carefully.

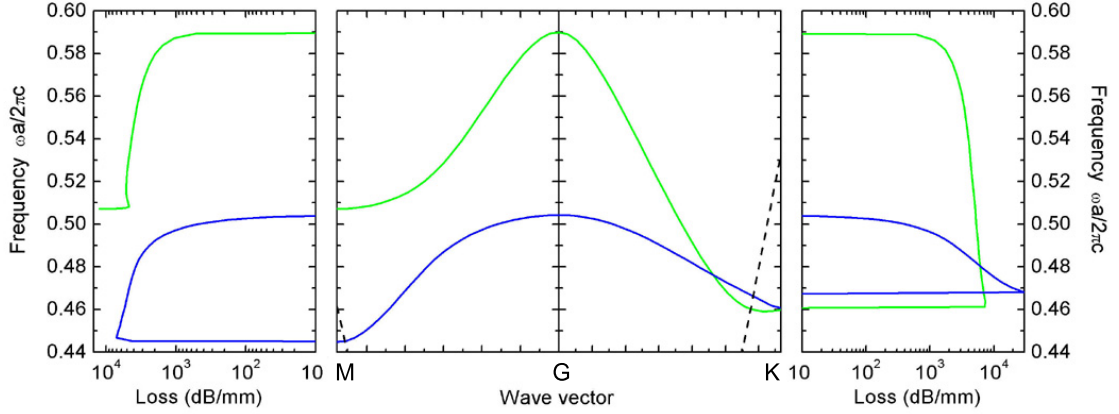


**Figure 2.14:** Band structure (center) and intrinsic radiation losses in dB/mm in the  $\Gamma$ -M (left) and  $\Gamma$ -K (right) directions of the same PPC as in fig. 2.13 for the second (blue lines) and third (green lines) modes. The dashed black lines represent the light line. The lattice constant  $a$  is assumed to be 500 nm.

However, the tendency observed in fig. 2.14 at the high-symmetry points is in good agreement with physical expectations.

## 2.4 Discussion of the Band Structure

So far, we have reviewed the basic properties of PPCs and studied them in more details for the special case of the IOSOI system. However, it turns out that PPCs show additional characteristics, which have been ignored in the literature up to now. Since such characteristics may play a crucial role in the functionality of several devices, we will address them in the following sections.

### 2.4.1 Origin of the Modes

Due to the finite height of the PPC, some additional modes appear in the band structure compared to the infinite 2D case, e.g., even modes with a TM origin or odd modes with a TE origin. These modes have been rarely taken into account in the work performed by several groups on PPCs. Fig. 2.15 shows the band structure of the IOSOI PPC with relative thickness  $h/a = 0.4$  and two semi-infinite structured oxide claddings, the relative radius of the air pores being  $r/a = 0.366$  (vertically even modes only). Among the bands presented in fig. 2.15, some modes with a clear TM origin exist. If we consider the field distributions of bands 3 and 5 (blue modes) at the M point, shown in fig. 2.16, we can notice that the  $E_z$ -field component has a maximum on both sides of the slab. The zero  $E_z$ -field component in the middle of the slab confirms that the modes are purely TE-polarized in this plane. However, the  $H_z$ -field component has a field distribution which does not correspond to any  $H_z$ -field distribution found in the infinite 2D case for the TE polarization. On the other hand, comparing the  $E_z$ -field distributions with those of the TM bands in the infinite 2D case, we can identify that band 3 and band 5 originate in the first and second TM-polarized band of the infinite 2D case, respectively. The slope of these bands, as well as their degeneracy at the K point, confirm this assumption, as can be verified comparing with the two lowest TM bands presented in fig. 1.6. This phenomenon is

a property of planar waveguides and was also demonstrated by Ochiai and Sakoda [73], in the case of PPCs, using group theory.

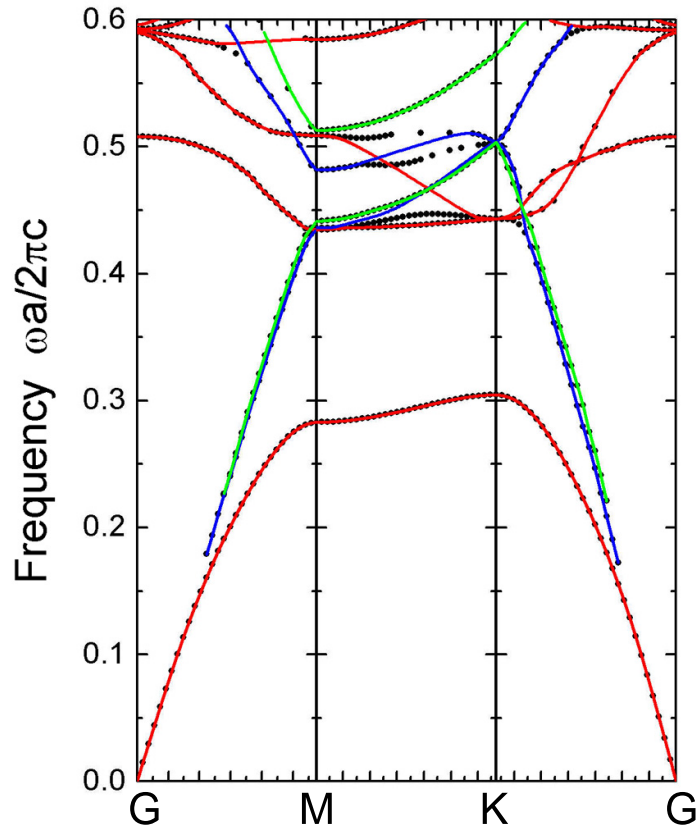


**Figure 2.15:** Band structure of a planar photonic crystal consisting of a silicon slab with relative thickness  $h/a = 0.4$  and two semi-infinite structured oxide claddings. The air pores are arranged in a hexagonal lattice with a relative radius  $r/a = 0.366$ . The black dots indicate the real bands, taking into account the interactions between modes having the same symmetry. For clarity, the slope of the bands without interactions has been extrapolated (colored solid lines). The red and blue curves highlight the bands with 2D TE and TM origin, respectively, whereas the cladding modes are shown in green. The band structure was determined combining the results of calculations with both the MIT package [47] and a 3D FDTD method [71].

Most of the TE-like modes with TM origin have a laterally even symmetry with respect to the  $(k-z)$ -plane and thus do not disturb the band structure. However, some of the modes have an odd symmetry and therefore can be excited by an external light beam, and interact with the PPC modes of interest. This is the case of the second band with TM origin (band 5, higher blue mode) along the  $\Gamma$ -K path.

Since the lowest band has an even symmetry, its presence within the band gap does not disturb the properties of the PPC. Therefore, the existence of these modes with TM origin has no significant influence on the functionality of devices based on the band gap, such as dispersion compensators.

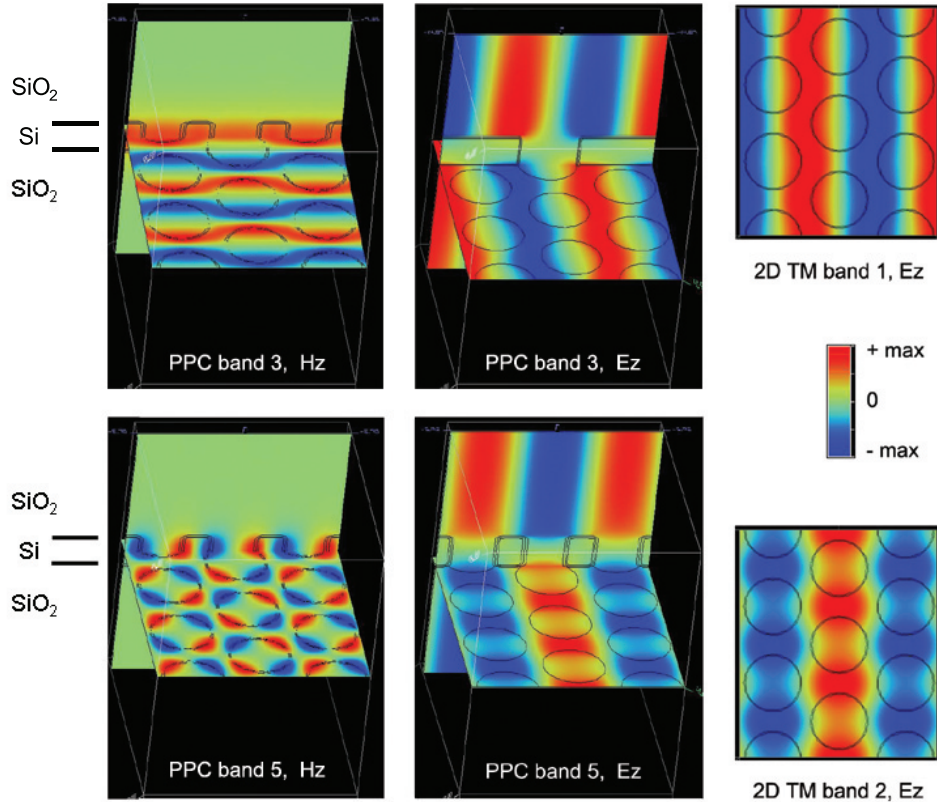


**Figure 2.16:**  $H_z$  and  $E_z$ -field distributions of the band 3 and 5 of the photonic crystal slab presented in fig. 2.15 (blue curves) at the M point. The  $E_z$ -field distributions are compared with the  $E_z$ -field component of the two lowest TM-polarized modes in the infinite Si-based 2D PC shown in fig. 1.6. The black circles and vertical lines indicate the position of the air pores, whereas the horizontal black lines indicate the position of the silicon slab (MIT package calculation [47]).

## 2.4.2 Cladding Modes and Surface Modes

In addition to the even (or TE-like) modes with TM origin, another type of modes can be seen in fig. 2.15, which are specific for PPCs: the cladding modes (green lines). Cladding modes are not only bounded to the core, but also to the surrounding cladding. Almost the whole energy of these modes is confined within the claddings. This phenomenon is demonstrated in fig. 2.17, which presents the  $H_z$ -field distribution of the lowest cladding mode of fig. 2.15, as well as the  $H_z$ -field distribution of the corresponding mode in an IOSOI PPC having the same parameters and a finite cladding of thickness  $d = 1.5 a$ . Comparing with fig. 2.4, we can verify that the lowest cladding mode has the same field distribution within the cladding as the lowest PPC mode within the core, where the term "PPC modes" designs the modes bounded to the core. Similarly, the second cladding mode has the same field distribution within the cladding as the second PPC mode within the core, and the same holds for all cladding bands. Furthermore, all the cladding modes are well confined within the cladding, indicating bounded states, as can be verified in fig. 2.17b.

Note that the entire discussion in this chapter holds for the case of infinitely extended claddings. However, in experimental systems, the claddings always have a finite thickness. The finite cladding thickness has no significant consequences on the PPC modes of interest, since they

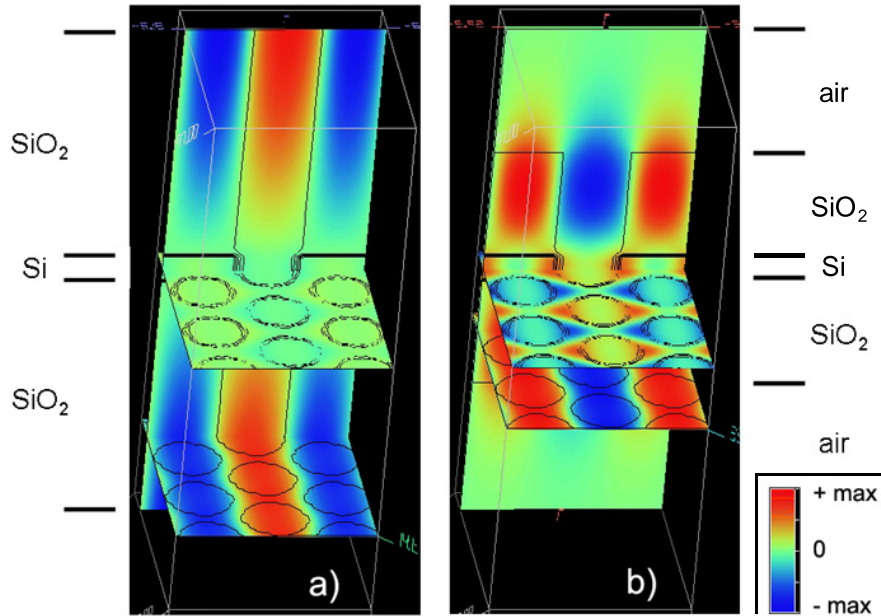


**Figure 2.17:** a)  $H_z$ -field component of the lowest cladding mode shown in fig. 2.15 and b)  $H_z$ -field component of the corresponding mode in an IOSOI PPC having the same parameters and a finite cladding of thickness  $d = 1.5 a$ . The black circles and vertical lines indicate the position of the air pores, whereas the thick and the thin horizontal black lines indicate the position of the silicon slab and of the oxide claddings, respectively (MIT package calculation [47]).

are well confined within the silicon core. Nevertheless, the position of the cladding modes in frequency is influenced by the cladding thickness, in the same manner as the PPC modes vary with the slab confinement. The thinner the cladding, the higher the frequency of the cladding modes. Fig. 2.18 presents the variations of the band structure with increasing cladding thickness for the IOSOI PPC with relative slab thickness  $h/a = 0.4$  and relative pore radius  $r/a = 0.366$ . Due to interactions between the bands, the variations of the cladding mode position induce changes in the whole band structure.

As can be seen from fig. 2.18, another band exists, following exactly the air light line. The origin of this mode is unclear, while it could be a surface mode propagating at the air/PPC interface. The frequency of this mode is constant and such a mode can be found in any design assuming finite claddings as well as in membrane structures. Because of their laterally odd symmetry, both the surface mode and the lowest cladding modes may interact with the odd modes of the PPC. We will not further discuss the consequences of the existence of the surface mode. Indeed, if we look at the band structure, this mode seems to interact with PPC modes in a similar way to the lowest cladding mode. Therefore, we believe that the discussion presented below on the lowest cladding mode also holds for the surface mode.

The variations of the cladding mode position at the M-point within the band gap, when the dielectric constant of the cladding layer is increased, are shown in fig. 2.19. Since the PBG is limited from above by the second PPC mode (blue line) at the M point, the cladding mode (green line) crosses the second PPC band for low cladding dielectric constants ( $\epsilon_{clad} \leq 2.5$ ), as illustrated in the left panel. By contrast, for larger cladding dielectric constants ( $\epsilon_{clad} \geq 2.5$ ), the two bands do not cross each other, as illustrated in the right panel. In the case of the IOSOI system, the dielectric constant of the cladding is 2.1. Therefore, the two bands cross each other. As will be discussed below, this fact will have a crucial importance.

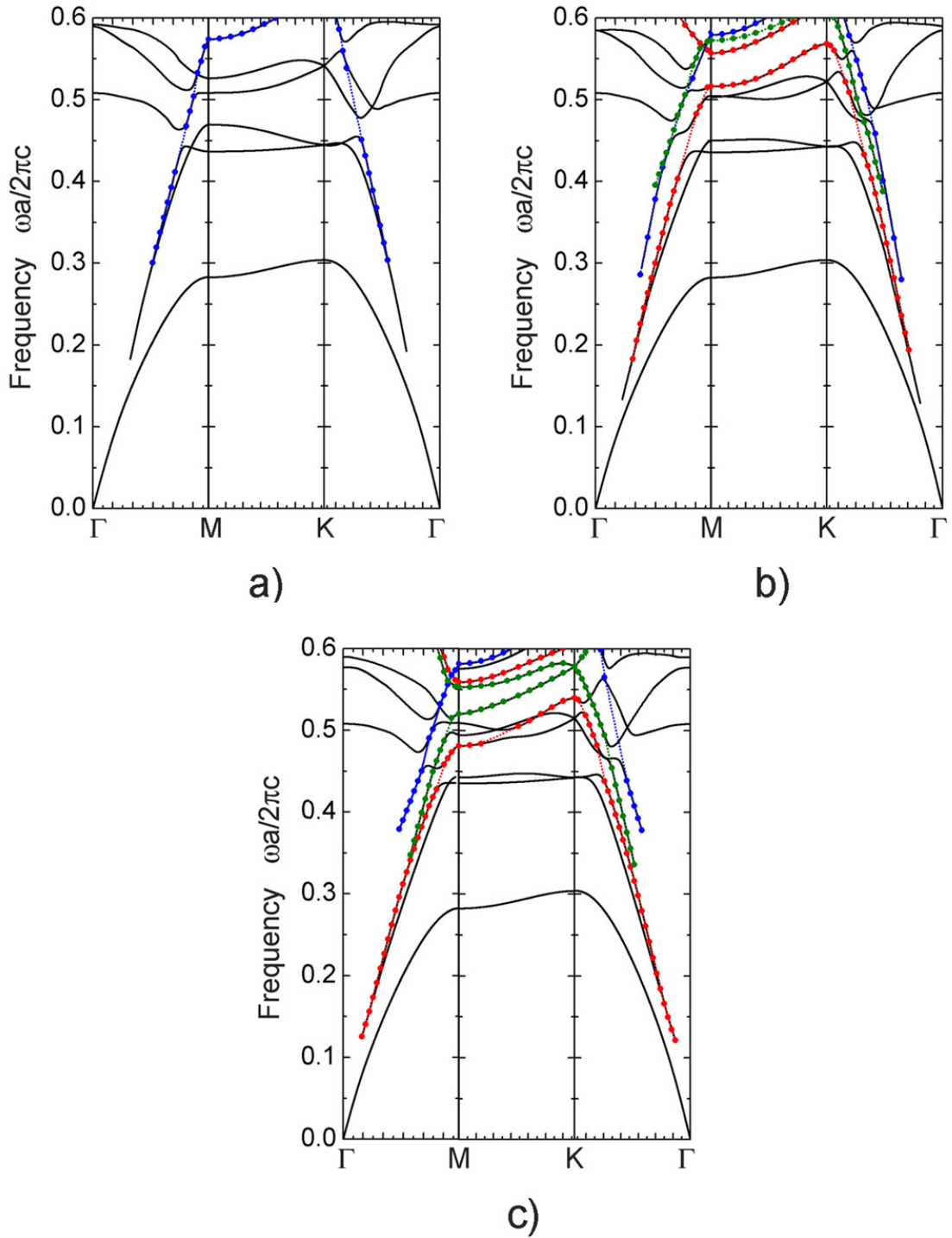


**Figure 2.18:** Variation of the band structure with the oxide thickness of an IOSOI-based photonic crystal slab with relative slab thickness  $h/a = 0.4$ , relative radius  $r/a = 0.366$ , and two finite structured oxide claddings (MIT package calculations [47]). a) Cladding thickness  $d = 0.5 a$ , b) cladding thickness  $d = 1.0 a$  and c) cladding thickness  $d = 1.5 a$ . All the modes with a vertically even symmetry are shown. The black solid lines show the complete band structure for even modes, taking into account the interactions between the modes. For clarity, the slope of the cladding and surface modes without interactions have been extrapolated and are highlighted by colored dots and dashed lines. The red and green dots highlight the slope of the cladding modes with TE and TM origin, respectively, whereas the blue dots reveal the surface mode. Note that the cutoff frequency of these modes cannot be determined precisely using the MIT package.

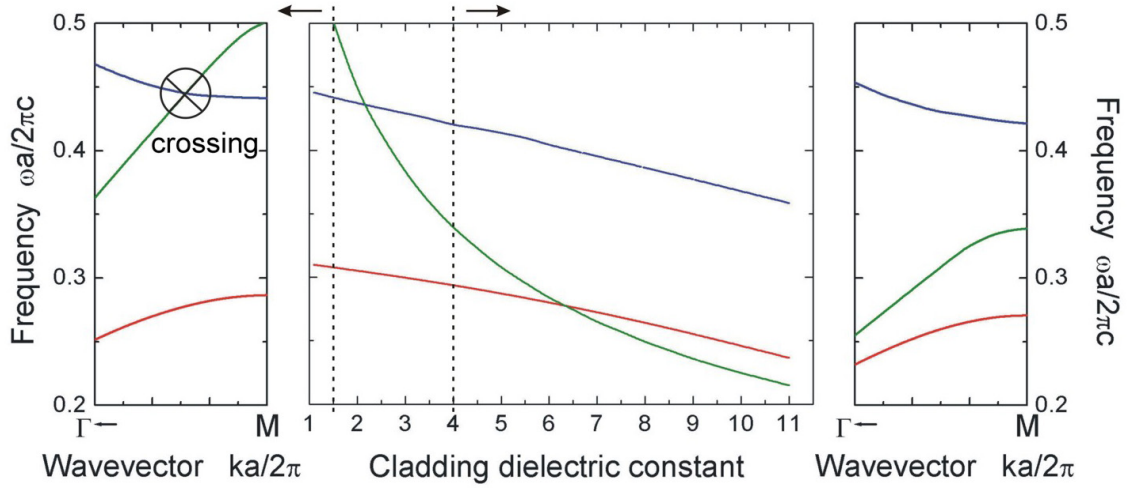


**Figure 2.19:** Gap map (central panel, variation of the eigenmodes frequency  $\omega a/2\pi c$  with the dielectric constant of the cladding material) of a silicon-based PC slab having a silicon core with relative thickness  $h/a = 0.4$  and a relative radius  $r/a = 0.366$ . The claddings are assumed to be semi-infinite. The red and blue curves show the variations of the lowest and second PPC bands limiting the band gap from the bottom (at the K-point) and the top (at the M-point), respectively. The position of the cladding mode at the M-point is shown (green curve), to put into evidence its position relatively to the second PPC mode. The left and right panels show the corresponding band structures for the two systems with cladding dielectric constants  $\epsilon_{clad} = 1.5$  and  $\epsilon_{clad} = 4.0$ , respectively (MIT package calculation [47]).

### 2.4.3 Consequences on the Planar-Photonic-Crystal Properties

Since the energy of the cladding mode is concentrated in the oxide, this mode should be only weakly excited by an external light beam focussed onto the PPC core. Similarly, it should interact only weakly with PPC modes having the same symmetry. Therefore, we could expect that the presence of this mode has a negligible influence on the PPC properties. However, the transmission and reflectivity computations, presented in the following, show that this mode has a deep impact on the PPC properties.

Fig. 2.20a shows the band structure of an IOSOI PPC along the  $\Gamma$ -M path. The PPC has a relative thickness  $h/a = 0.3$ , a relative pore radius  $r/a = 0.366$ , and two finite oxide claddings with thickness  $d = 1 a$ . The computation has been performed using a FDTD code by C. Hermann and O. Hess [71]. For a better comparison with the transmission calculation, only the modes that can be excited by an external light source are shown, i.e., the modes with laterally odd symmetry. The corresponding transmission through such a PPC having a width of 21 lattice constants is presented in fig. 2.20b.

In this simulation, different interesting phenomena can be verified. First, the lowest band of the PPC (red line) corresponds to high transmission. Since this mode is located entirely below the light line (grey line), it confirms the fact that modes below the light line are guided and lossless. The well-defined Fabry-Perot oscillations are a sign for the propagating nature of this mode. To fit to a common experimental case, where the PPC is included within a planar waveguide, we consider the incident wave in the transmission calculation to be the fundamental mode of the corresponding planar waveguide. The coupling losses between the PPC and the planar waveguide have been taken into account in the transmission. Therefore, the transmission of the lowest PPC mode is not equal to 1. If we also know the reflectivity of the PPC, the average total losses of the PPC can be deduced from the transmission and reflectivity calculations following

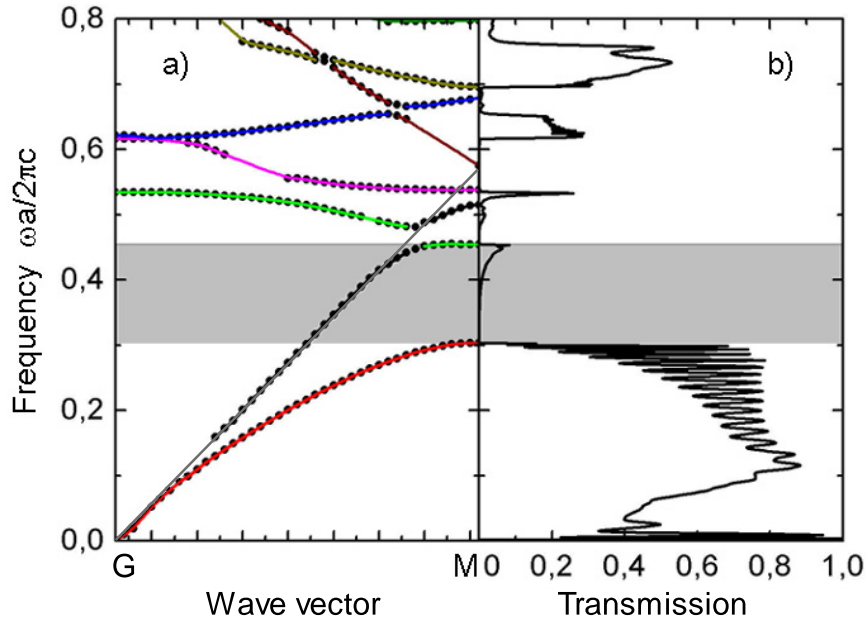


**Figure 2.20:** a) Band structure of an IOSOI PPC with relative thickness  $h/a = 0.3$ , relative pore radius  $r/a = 0.366$ , and finite claddings with relative thickness  $d/a = 1$ . b) Transmission through such a PPC having a width of 21 lattice constants (FDTD calculation by C. Hermann and O. Hess [71]).

the simple equation

$$R + T + L = 1 \quad (2.4)$$

where T is the transmission, R the reflectivity, L the losses, and the material absorption is assumed to be negligible. Fig. 2.21 presents the reflectivity, transmission, and losses for the same PPC as in fig. 2.20. Despite the strange features arising from FDTD artifacts for frequencies below 0.1, we can verify that the coupling losses are around 20 % for the lowest PPC mode.

The lowest cladding mode (black line in fig. 2.20) rises up above the first PPC mode and interacts with the second band with TE origin (green line), resulting in a large avoided crossing. This corresponds to the mini-stop-gap observed in transmission in the normalized frequency range  $\omega a/2\pi c = 0.45-0.48$ . Another gap, between the second and third PPC modes, can be observed for frequencies around 0.54. Between these two stop-gaps, the cladding mode and the second slab mode coexist. Since the second slab mode can be easily excited by the external source, the reflectivity is quite low. However, in this frequency range, this band is above the light line and has a short lifetime (see fig. 2.14). Therefore, the corresponding transmission is almost zero and the whole signal coupled to this mode is lost. The higher PPC modes, existing at frequencies above 0.55, lie entirely above the light line. Some of them have a very short lifetime and strong radiation losses, leading to small transmission. Others possess longer lifetime, leading to higher transmission. Moving to higher frequencies, the number of bands increases, and the reflectivity thus tends to decrease and the losses to raise.

Because the incident light source is very well confined within the core of the planar waveguide, the cladding mode should be only weakly excited and should not contribute to the transmission. This can be verified in the lower part of the band gap, where the cladding mode is the only existing mode. In this frequency range  $\omega a/2\pi c = 0.3-0.4$ , no transmission occurs while the reflectivity is very high, indicating that the cladding mode does not couple to the incident signal.

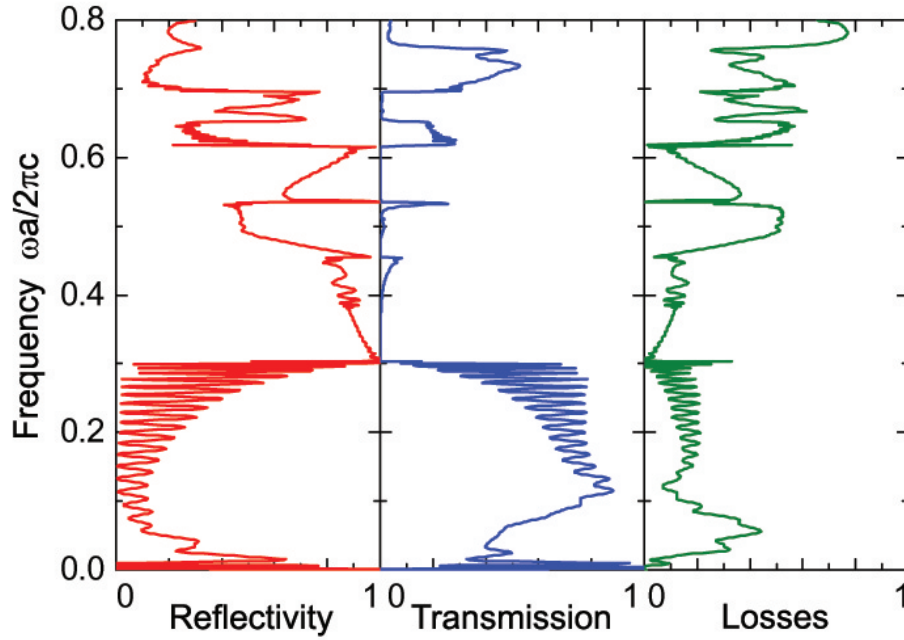


**Figure 2.21:** Reflectivity  $R$  (red curve), transmission  $T$  (blue curve) and radiation losses  $L$  (green curve) for the PPC presented in fig. 2.20 (FDTD calculation by C. Hermann and O. Hess [71]).

However, we clearly see a transmitted signal at higher frequencies around  $\omega a/2\pi c = 0.4-0.45$ , although the cladding mode is still the only mode existing. This phenomenon is not due to a direct coupling of light to the cladding mode. To better understand the role of the cladding mode in the transmission, we compare the transmission for different PPC lengths through an IOSOI PPC with relative thickness  $h/a = 0.4$ , as exhibited in fig. 2.22b. The relative pore radius is  $r/a = 0.366$ , and the claddings have a relative thickness  $d/a = 1.2$ . The length of the PPC is 21, 41, and 81 crystal rows in the  $\Gamma$ -M direction, respectively. As shown in the inset of fig. 2.22b, the transmission within the band gap does not depend on the length of the PPC. Furthermore, Fabry-Perot oscillations are clearly visible. It means that the transmitted signal is due to a propagating mode, which is vertically confined and thus do not present any radiation losses. Overlapping the band structure for this PPC having a cladding thickness  $d = 1.2 a$  with the band structure of the same PPC having a cladding thickness  $d = 0.8 a$  (fig. 2.22a), we can notice differences in the slope of the modes for the two cladding thicknesses. This feature can only be due to interactions with the cladding mode. Especially for the second PPC mode and the cladding mode, the deviations between the bands already start for wave vectors in the middle of the  $\Gamma$ -M path. In the case of the cladding mode, these wave vectors correspond exactly to the frequency, at which the transmission within the band gap starts (around  $\omega a/2\pi c = 0.35$ ). This proves that the interaction between the cladding mode and the second PPC mode is responsible for the transmission [79].

This study brings us to the following conclusion: when the cladding mode and the second PPC mode come closer to each other so as to cross, their identical symmetry results in a strong interaction, leading to a very large anti-crossing. Around this anti-crossing, we have verified that the field distributions of both modes are mixed. In particular, this means that the field distribution of the cladding mode has a non-negligible proportion of the electromagnetic field of the second PPC mode. As a consequence, the cladding mode has energy concentrated not only within the oxide cladding, but also within the silicon core. Therefore, this mode can be slightly excited by the external light source, leading to transmission within the band gap.

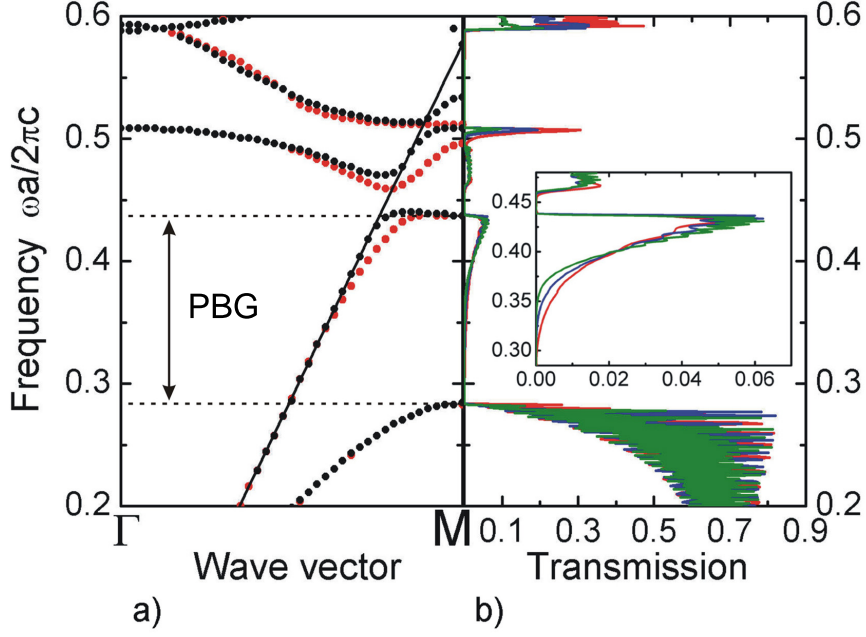


**Figure 2.22:** a) Band structures of IOSOI PPCs with relative thickness  $h/a = 0.4$ , relative pore radius  $r/a = 0.366$ , and finite claddings with thickness  $d = 1.2 a$  (red dots) and  $0.8 a$  (black dots), respectively. The black solid line indicates the position of the air light line. b) Transmission through the PPC with cladding thickness  $d = 1.2 a$  having a width of 21 (red curve), 41 (blue curve), and 81 (green curve) lattice constants, respectively. The inset shows an enlargement of the transmission within the band gap (FDTD calculation by C. Hermann and O. Hess [71]).

Since the field mixing becomes stronger when approaching the anti-crossing, the transmission becomes more pronounced at the upper edge of the band gap. To verify this explanation, we calculate the Poynting vector of the electromagnetic field in the  $\Gamma$ -M direction for two different frequencies within the band gap. The Poynting vector  $\vec{S}$  represents the energy flow for a given mode in a given direction, following the equation:

$$|\vec{S}| = |\vec{E} \times \vec{H}| \quad (2.5)$$

Fig. 2.23 presents the norm of the Poynting vector in the  $\Gamma$ -M direction through a vertical section of the PPC for the two frequencies  $\omega a/2\pi c = 0.4$  and  $0.43$ . Comparing these two results, it is clear that the energy flow within the silicon core is much higher for the frequency  $0.43$  than for  $0.4$ , indicating a higher proportion of the second PPC mode. Furthermore, the total energy is much higher for the frequency  $0.43$  than for  $0.4$ , which is a sign for a higher transmitted signal.

All above elucidations clearly address the role played by the lowest cladding mode. Now we turn to investigate the consequences of its presence within the band gap on the functionality of devices based on the existence of the PBG.

If we consider the three-layer system oxide/silicon/oxide surrounded by air (the case in the transmission calculations presented above), the presence of the cladding mode reduces the usable size of the PBG by a factor of two. In particular, waveguide modes will only be confined along the line defect, if they exist in the lower half of the band gap. If they are located in the upper half, a possible coupling of light to the cladding mode will lead to losses in the plane of the PPC. However, since the cladding mode is below the air light line, no losses in the vertical

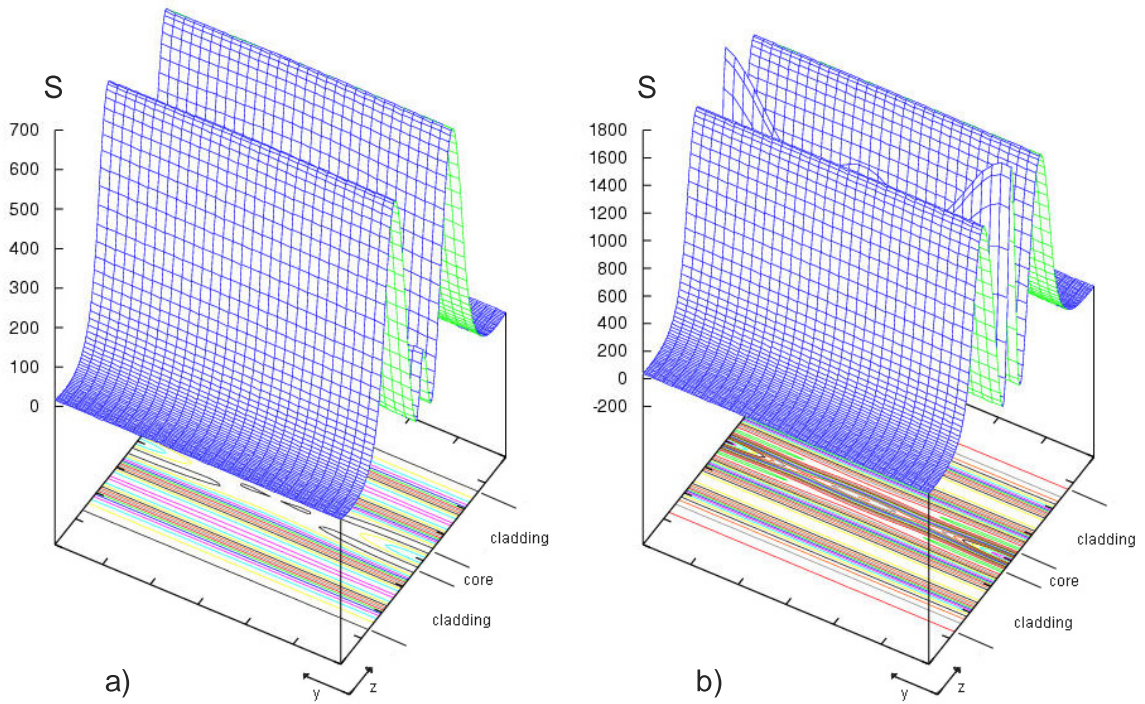


**Figure 2.23:** Absolute value of the Poynting vector  $S$  through a vertical ( $y$ - $z$ )-plane representing the energy flow in the  $\Gamma$ - $M$  direction for the IOSOI PPC of fig. 2.22 with cladding thickness  $d = 1.2 a$ . The relative frequencies investigated are a)  $\omega a/2\pi c = 0.4$  and b)  $\omega a/2\pi c = 0.43$  (FDTD calculation by C. Hermann and O. Hess [71]).

direction are expected. This case is illustrated in fig. 2.24a, which shows the  $H_z$ -field intensity in a vertical cross section through the PPC at a frequency  $\omega a/2\pi c = 0.4$ .

In most experimental situations, the structure described above is located on the top of a higher-effective-index substrate, oxide or silicon, as illustrated in fig. 2.24b. This changes the situation drastically, because the cladding mode is not guided anymore by total internal reflection at the interface to the substrate. The cladding mode radiates into the substrate and therefore provides a significant loss channel for frequencies within the band gap. Fig. 2.24b shows a cross-section of the  $H_z$ -field intensity of the cladding mode in the presence of a  $\text{SiO}_2$  substrate for the relative frequency  $\omega a/2\pi c = 0.4$ . In this case, the lower cladding no longer guides energy, while there is still guiding in the top cladding and significant intensity within the core. Therefore, for this system, we expect a much lower transmission within the band gap, since a large part of the energy coupled to the cladding mode is radiated into the substrate. This may be the reason why the existence of the cladding mode has never been detected experimentally so far.

From an experimental point of view, there exist some more variations to this material system. Most structures do not have an upper cladding [65, 80] (fig. 2.24c), or, additionally, the air holes are often drilled only through the Si layer [53, 62], leaving the underlying oxide cladding unstructured (fig. 2.24d), as already discussed in fig. 2.1. The theoretical analysis of those systems is more complicated, because TE-like and TM-like modes cannot be separated anymore due to the mirror symmetry breaking in the  $z$ -direction. However, the effect described above still exists, as confirmed in fig. 2.24c and d. In all cases, magnetic field strength with significant contribution in the core for frequencies within the band gap is clearly visible. The qualitative effect as a loss mechanism when put on a substrate exists as well. Consequently, for application to dispersion compensation, as for any application based on the existence of the band gap, it is

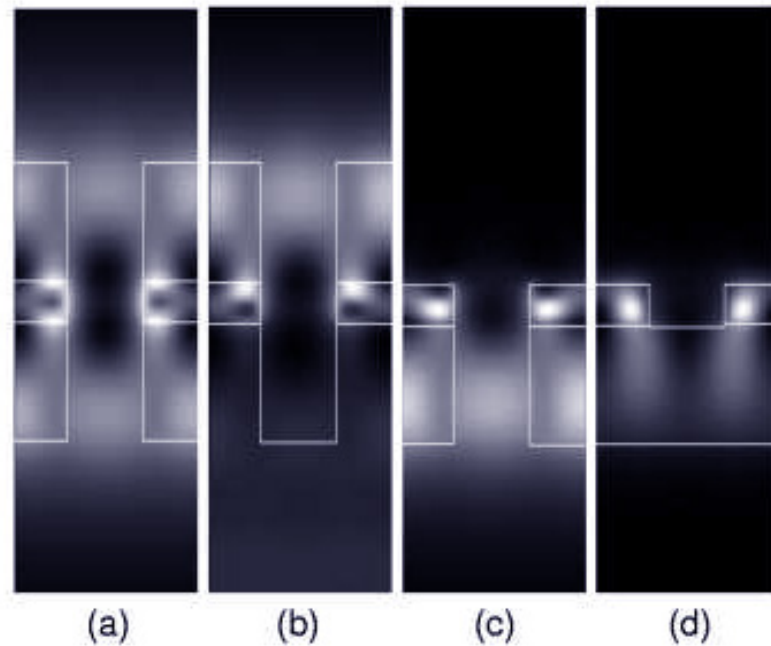


**Figure 2.24:** Magnetic field intensity for a relative frequency  $\omega a/2\pi c = 0.4$  in a vertical (y,z)-plane normal to the  $\Gamma$ -M direction. White and dark regions represent high and zero intensities, respectively. The different dielectric structures are sketched with white lines. a) Three-layer system oxide/silicon/oxide surrounded by air, b) three-layer system oxide/silicon/oxide placed on an oxide substrate, c) asymmetrical system without upper oxide cladding surrounded by air, and d) asymmetrical system without upper oxide cladding and with unstructured lower cladding surrounded by air (FDTD calculation by C. Hermann and O. Hess [71]).

necessary to localize our defect modes in the lower part of the PBG, where no transmission due to the cladding mode occurs [79].

## 2.5 Conclusions

To conclude, an extended study of the properties of the bulk PPC has been performed in this chapter. It includes a qualitative as well as quantitative study of the effects of the finite PPC thickness on the band structure and on the PPC behavior. Issues like higher-order modes, variations of the band structure with the different geometrical parameters, or radiation losses have been addressed.

Moreover, we have highlighted the fact that this detailed study is necessary if we intend to design devices and to understand their behavior. In particular, an important loss mechanism within the band gap of the PPC has been put into evidence, which can not be avoided in high-index-contrast structures with claddings like SOI-based PPCs. Although this effect has not been quantified yet, it is in any case not negligible and has to be taken into account while designing the device.

# 3. Design of the Dispersion Compensator

The challenge in designing photonic-crystal-based dispersion compensators consists of three issues which have to be addressed simultaneously. The device should have a very high absolute negative dispersion of  $\sim 100$  ps/nm/mm over at least 40 GHz, it should exhibit low losses during pulse propagation, and it should be tunable. Furthermore, since the DC should be a part of a larger optical circuit, we should also pay attention to the coupling of light between the DC and the other devices. Starting from the bulk design determined in the previous chapter, the procedure is first to create different waveguides in the PPC, and to choose the design yielding the best dispersion slope. Next, the properties of this waveguide will be studied in more details. A design will be proposed that satisfies all requirements: high dispersion, low propagation losses, tunability and good light coupling.

## 3.1 Dispersion Properties

### 3.1.1 Selection of the Waveguide Type

If a line defect is introduced into a photonic crystal slab lattice, the same phenomenon occurs as in the case of infinite 2D photonic crystals [56]. For an appropriate design of the waveguide, some defect states are located within the band gap of the photonic crystal, so that light is confined along the line defect in the plane of the crystal in this frequency range. Combining this in-plane confinement with the vertical confinement due to the index contrast in the vertical direction, 3D light confinement is possible within waveguides in PPCs [51, 52, 53, 62, 63, 64]. However, this 3D light confinement is possible only below the light line, which corresponds to a very small range of wave vectors. As can be recognized in fig. 3.1, which presents the projected band structure of the bulk PPC along the  $\Gamma$ -K direction, the wave-vector range of interest is at the most  $ka/2\pi = 0.4$ - $0.5$  in the case of the IOSOI PPC with relative core thickness  $h/a = 0.4$  and relative pore radius  $r/a = 0.366$ . Therefore, for the selection of the waveguide design, the defect mode properties will be considered only in the limited wave-vector range  $ka/2\pi = 0.4$ - $0.5$ .

In order to choose a waveguide design suitable for dispersion compensation, several different designs will be considered and the group velocity of all defect modes having a convenient symmetry will be calculated. Then the mode yielding the most interesting group velocity variations will be selected.

Strictly speaking, 3D calculations are necessary to calculate the band structure of the different defect designs. However, we are confronted by two major problems, as illustrated in fig. 3.2. The computations with the FDTD method are quite difficult to perform in case of very low group velocities, because it requires calculations of the eigenmode frequency with high accuracy. This leads to extremely long computation times. Using the MIT package for 3D waveguide computations, the vicinity of the light cone may disturb the bands already in the guided region, because of the several artificial modes existing above the light line, which interact with the "true" ones.

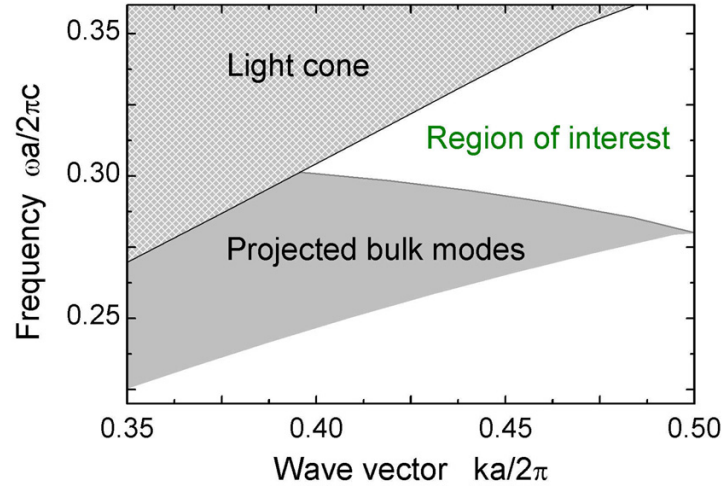


**Figure 3.1:** Projected band structure of bulk PPC modes onto the new 1D Brillouin zone. The PPC consists of an IOSOI structure with relative core thickness  $h/a = 0.4$ , relative pore radius  $r/a = 0.366$ , and two infinitely extended oxide claddings.

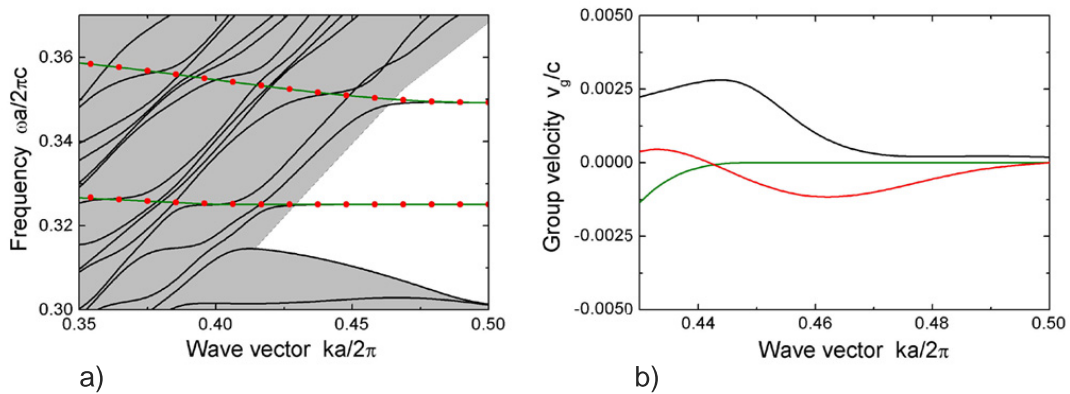


**Figure 3.2:** Comparison between the results of 2D (red) and 3D (black) waveguide computations performed with the MIT package [47] and 3D calculations using a FDTD method (green) [71]. a) Band structure, and b) group velocity of the lowest defect mode. The waveguide structure consists of a W1 waveguide in an IOSOI PPC with relative thickness  $h/a = 0.3$  and relative pore radius  $r/a = 0.366$ .

Following the method already presented in section 2.3 in the case of bulk PPCs, the exact slope of the defect modes can be determined. However, this is again extremely time-consuming. In fig. 3.2, the comparison between the results of 3D calculations performed with both MIT and FDTD codes and 2D calculations performed with the MIT package put into evidence these two problems.

The comparison done in fig. 3.2 between 2D and 3D calculations highlights also the fact that the slope of the defect modes in the guided region of the PPC is quite similar to that of the defect mode in the corresponding infinite 2D PC. This is due to the high confinement of the light within the PPC core. Therefore, the selection of the preliminary waveguide design will be done with 2D calculations. Although some variations are expected between 2D and 3D calculations for a given waveguide design, they are small compared to the difference in dispersion slope between two different types of waveguides.

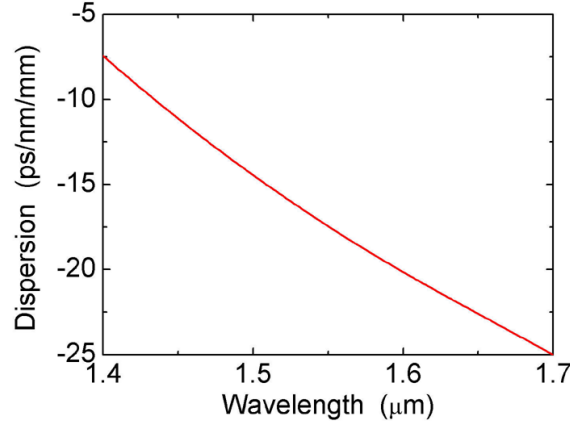


**Figure 3.3:** Ideal slope of the dispersion in a PC waveguide suitable for dispersion compensation. The dispersion is negative and almost linear with a slightly concave slope, i.e.,  $\Delta D(\lambda_{small}) > \Delta D(\lambda_{long})$ . In this particular example, the device allows for the exact dispersion compensation of 1 km SMF within 1 mm PPC waveguide.

As already presented in fig. 1.3, the dispersion in a standard optical fiber is positive and increases almost linearly with a slightly concave slope, i.e.,  $\Delta D(\lambda_{small}) > \Delta D(\lambda_{long})$ . Therefore, the dispersion within our DC has to be negative and decreasing almost linearly, with a similar slightly concave slope, i.e.,  $\Delta D(\lambda_{small}) > \Delta D(\lambda_{long})$ . This slope is shown schematically in fig. 3.3. To determine the dispersion in the photonic crystal waveguide from the band structure, equation 1.1 is used:  $D = d(v_g^{-1})/d\lambda$ , where the wavelength  $\lambda = 2\pi c/\omega$  and the group velocity  $v_g = d\omega/dk$  can be directly deduced from the defect band under consideration. Consequently, to yield a negative dispersion, both the absolute group velocity and the band frequency should either decrease, or increase, with increasing wave vector, as illustrated in fig. 3.4 (violet and green curves, respectively). To select the waveguide design suitable for dispersion compensation, we will consider the group velocity variations of the defect bands for each design. The absolute group velocity of the selected band should be as small as possible and either increase, or decrease, continuously within a large wave vector range.

Several waveguide designs have been considered, such as W1 and W3 waveguides with rows of missing pores and/or smaller pores. A detailed study of the band structures and the group velocity variations for each design is presented in the Appendix. To select the waveguide design, two main properties must be considered. First, the group velocity has to be low, yielding high dispersion, and both the group velocity and the band frequency should decrease (resp. increase) with increasing wave vector within a large wave-vector range. Secondly, the waveguide has to be single-mode in the frequency range of interest. As can be deduced in the Appendix, this latter condition is fulfilled only for the W1 waveguides. Indeed, all the W3 waveguides under study are multi-mode. Considering now the group velocity, we notice that it is much smaller ( $\leq 10^{-3}c$ ) for the W1 waveguide made of one row of missing pores than for the W1 waveguide made of one row of smaller pores, as can be observed in fig. 6.2 and fig. 6.6 of the Appendix, respectively. Furthermore, from an experimental point of view, the W1 waveguide made of one row of smaller pores may be quite difficult to fabricate, because it requires much smaller pore radii for building the waveguide than in the surrounding lattice. Therefore, we select the W1 waveguide made of one row of missing pores as our preliminary design for the DC.

In the following section, we will perform a more detailed 3D analysis of the properties of this selected design.

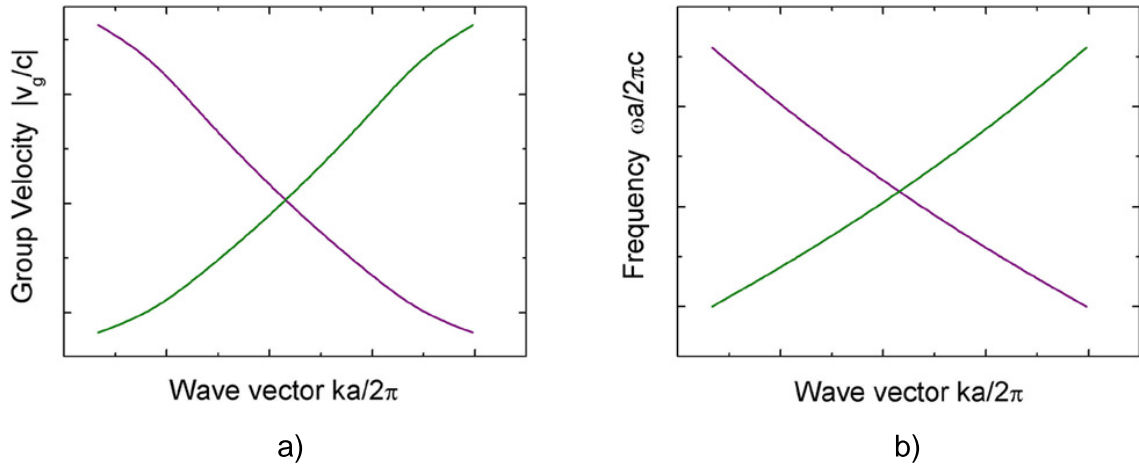


**Figure 3.4:** Ideal slopes of a) the absolute group velocity and b) the frequency, corresponding to the dispersion shown in fig. 3.3 (schematic). To yield a negative dispersion, it is necessary that the group velocity increases with increasing frequency, i.e., either both the absolute group velocity and the band frequency should decrease with increasing wave vector (violet curves), or both of them should increase with increasing wave vector (green curves).

### 3.1.2 Study of the Selected Design

After the preliminary selection of the waveguide design based on 2D calculations, the next step is to verify the properties of this waveguide with an extended 3D analysis.

Fig. 3.5 shows the band structure of a W1 waveguide in an IOSOI PPC, calculated using the MIT package [47]. The PPC consists of a silicon core with relative thickness  $h/a = 0.4$  surrounded by two structured silicon oxide claddings assumed to be semi-infinite. The pores have a relative radius  $r/a = 0.366$ . The corresponding band structure for the bulk photonic crystal has been shown in fig. 2.9. The waveguide is made of one row of missing pores in the  $\Gamma$ -K direction. In fig. 3.5, the lower grey region corresponds to the continuum of the projected bulk bands, and the upper grey region to the light cone. The defect modes below the region of projected bulk modes are index-guided, as in the case of the infinite 2D photonic crystal discussed in section 1.3.2. Furthermore, the field distributions (1, 2 and 3) in the  $(x,y)$ -mirror plane in the middle of the silicon slab shown in fig. 3.5 are very similar to the corresponding ones presented in fig. 1.10. This is related to the fact that the defect modes are very well confined within the silicon core, as can be seen in the vertical cross sections shown in fig. 3.5. Above the projected bulk modes, the defect modes lie within the band gap of the photonic crystal. They are vertically confined as long as they lie in the white region below the light line. Only in the case of periodicity breaking, like waveguide bends, some intrinsic losses have to be expected below the light line, that depend on a complex way on several parameters such as dielectric contrast and defect design. We do not consider this particular case here, since in this work we focus on straight waveguides. For in-plane confinement, both guiding mechanisms coexist, as in the case of infinite 2D waveguide structures: either the modes are index-guided (like band 5) or they are guided due to the existence of the photonic band gap (like band 4). Again, comparison between the field distributions of these two defect modes and the two corresponding ones presented in fig. 1.9a and the band 4 in fig. 1.10 shows strong similarities [56].

From the discussion of sections 2.4.2 and 2.4.3, we could expect that some cladding modes

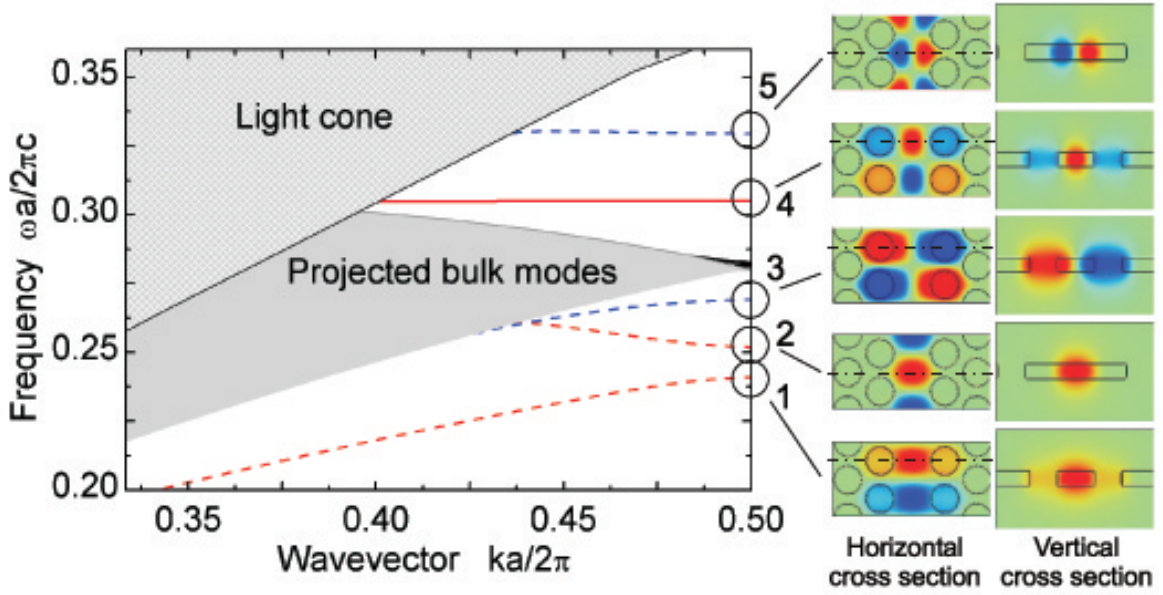


**Figure 3.5:** band structure (left) of a W1 waveguide consisting of one row of missing pores in a photonic crystal slab. The photonic crystal is fabricated in a silicon core with relative thickness  $h/a = 0.4$  surrounded by two structured silicon oxide claddings (MIT package calculation [47]). The pores are arranged in a hexagonal lattice, and have a relative radius  $r/a = 0.366$ . The lower grey region corresponds to the continuum of projected bulk bands, and the upper grey region to the light cone. The defect modes are sorted into index-guided (dashed lines) and photonic-band-gap guided modes (solid lines) as well as into laterally odd (red lines) and even modes (blue lines).  $H_z$ -field distributions (right) of the five defect modes which are vertically guided at the boundary of the first Brillouin zone (J-point). The horizontal cross sections show the field distributions in the  $(x,y)$ -mirror plane in the middle of the silicon slab, the black circles indicating the position of the pores. The vertical cross sections show the field distributions in the  $(x,z)$ -planes containing the intensity maxima, the black lines indicating the position of the silicon slab. For each band, the position of the  $(x,z)$ -plane containing the intensity maxima is highlighted by a dashed line in the horizontal cross section of the field distribution.

are also existing in the waveguide band structure. We already know from fig. 2.15 that the lowest bulk cladding mode exists within the band gap of the PPC. As in the case of the PPC bulk modes, the projection of the cladding mode should lead to a continuum of states within the frequency range where this mode is existing. The lower limit of this continuum is highlighted by a green line in fig. 3.6. Furthermore, due to the effective index contrast between the defect line and the surrounding patterned region, we can also imagine cladding defect modes, which are lying below the lowest bulk cladding mode and guided by total internal reflection along the defect. As shown in fig. 3.6, such cladding modes do really exist. Since the two cladding defect modes visible in fig. 3.6 (red lines) are lying below the lowest bulk cladding mode and within the band gap of the photonic crystal, they are confined laterally. Furthermore, due to their position below the air light line, they are also confined vertically in the ideal case of an IOSOI PPC suspended in air. Of course, from an experimental point of view, the system is always placed on the top of a silicon oxide or silicon substrate having a higher effective index. In this case, the cladding defect mode is not confined vertically anymore at the interface between the lower cladding and the substrate, and constitutes a loss mechanism if the mode is excited. The field distribution of the lowest cladding defect mode is shown in fig. 3.7. Comparison between the field distribution of this mode within the cladding, and the field distribution of the lowest PPC defect mode shown in fig. 3.5 in the core, shows very strong similarity. It confirms that

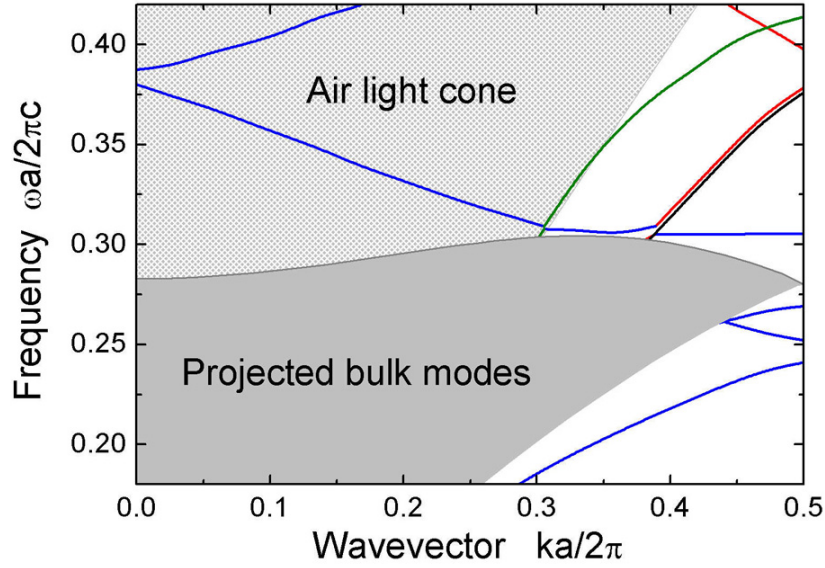


**Figure 3.6:** Band structure of the same W1 as in fig. 3.5. Only the modes with laterally odd symmetry are shown. The PPC defect modes are shown in blue, whereas the cladding defect modes are shown in red. The black and green lines indicate the light line of the patterned oxide cladding in the W1 waveguide and the lower limit of the projected bulk cladding mode, respectively. Note that the cutoff frequency of the cladding modes can not be determined with high accuracy with the MIT package [47].

this mode is the lowest index-guided cladding defect mode. Furthermore, if we consider a PPC with finite cladding thickness (fig. 3.7b and 3.7c), we can verify that the mode is bounded to the three-layers system oxide/silicon/oxide and the main part of its energy is confined within the cladding.

The cutoff frequency of the lowest cladding defect mode cannot be accurately determined using the MIT package. However, if its cutoff frequency is low enough, this mode may interact slightly with the PPC defect mode of interest, leading to a small anti-crossing, as can be recognized in fig. 3.6. This interaction between the two bands does not seem to have any negative consequence on the DC functionality. On the contrary, it presents a great advantage. For small wave vectors, in the region where the PPC defect mode is index-guided, the band is decreasing very fast. After the anti-crossing with the PBG-guided mode rising from the lower region of projected bulk modes, the defect mode is very flat and reaches a minimum before increasing very slightly. Due to this non-monotone slope, the waveguide should not be single-mode in the frequency range where the defect band is very flat, and consequently, it should not be suitable for dispersion compensation. However, the interaction with the cladding defect mode leads to a very small stop-gap, which covers the frequency range of interest. Therefore, the waveguide is single-mode in this frequency range (assuming that the projected bulk cladding mode is not excited).

We focus now on the lowest PBG-guided mode (band 4 in fig. 3.5), corresponding to the band selected for dispersion compensation with 2D computations (see fig. 6.2 in the Appendix). If we calculate the group velocity with a full 3D computation, we notice some differences to the 2D case, as shown in fig. 3.8a. The group velocity is slightly higher (up to  $5 \cdot 10^{-3}c$ ), but it has a convenient slope within a larger wave vector range. Indeed, the group velocity is first increasing in the wave vector range  $ka/2\pi = 0.40-0.43$ , and then decreasing again for normalized wave vectors larger than 0.43. Since the defect band is increasing, the group velocity should also increase to yield negative dispersion. Therefore, the wave vector range suitable

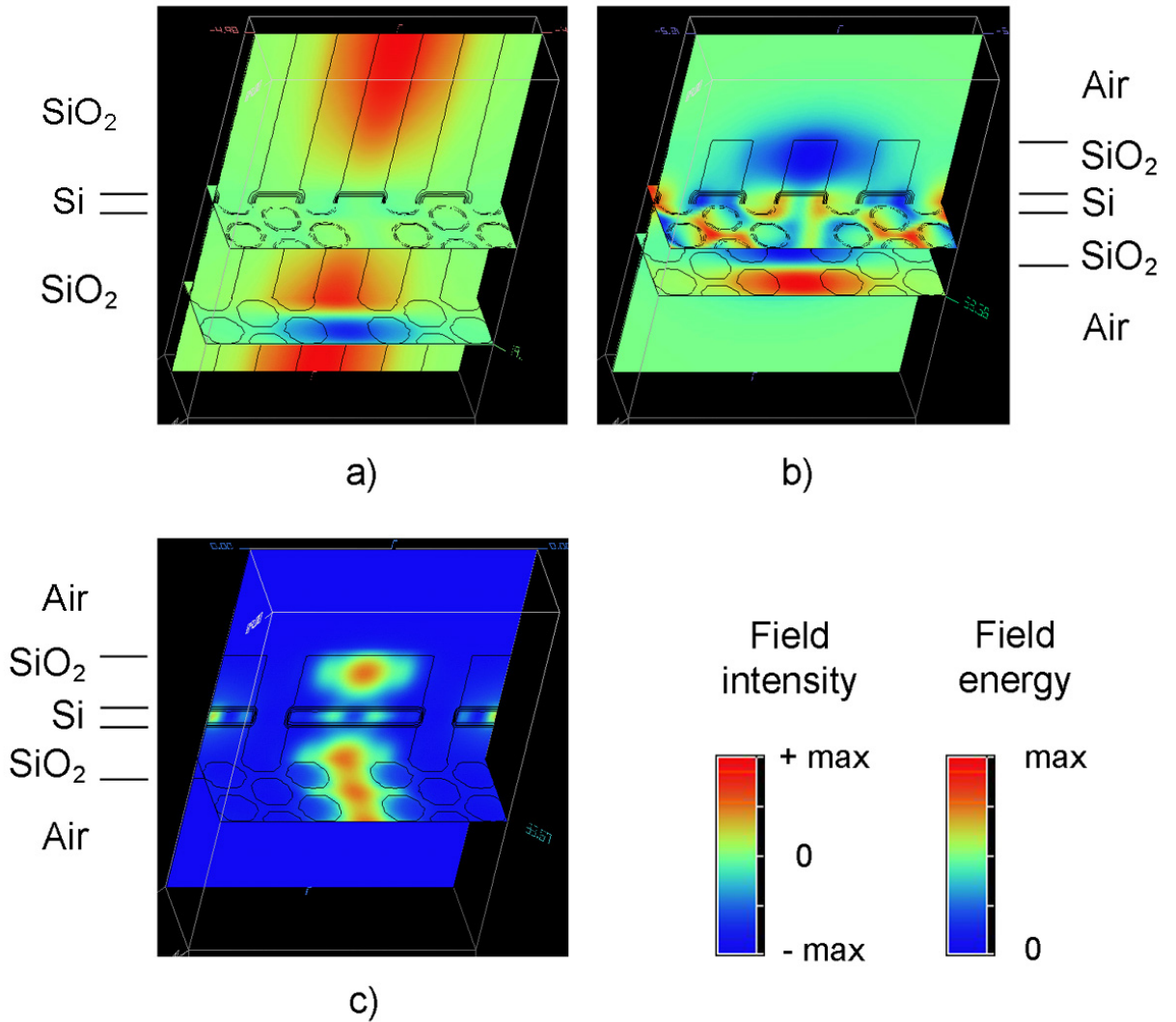


**Figure 3.7:** a)  $H_z$ -field distribution of the lowest cladding defect mode shown in fig. 3.6 at the J-point. b)  $H_z$ -field distribution and c) total energy density of the same mode in an IOSOI PPC waveguide having the same parameters as in case a) and a finite cladding thickness of  $d = 1.5 a$ . The black circles and vertical lines indicate the position of the air pores, whereas the horizontal black lines indicate the position of the silicon slab and of the two silicon oxide claddings (MIT package calculation [47]).

for dispersion compensation is  $ka/2\pi = 0.40$ - $0.43$ . As shown in fig. 3.8b, the corresponding dispersion is highly negative, with a value  $D$  of  $-7\,000$  ps/nm/mm at  $1550$  nm wavelength and a total dispersion compensation  $\Delta D$  of  $20\,000$  ps/nm/mm over the  $40$  GHz bandwidth. This could compensate for the dispersion of  $1$  km SMF ( $17$  ps/nm) within only few  $\mu\text{m}$  of PPC waveguide. This is even higher than the typical dispersion value obtained in CCW waveguides, comparing with fig. 1.12. However, like in the case of CCWs, the dispersion slope is convex, i.e.,  $\Delta D(\lambda_{small}) < \Delta D(\lambda_{long})$ , leading to a large residual dispersion after compensation. Furthermore, the bandwidth, in which the dispersion slope is almost linear, is smaller than the desired bandwidth ( $0.2$  nm in the region of negative dispersion, instead of the desired  $0.4$  nm). It means that further improvements of the design will be necessary to fulfill the requirements on the bandwidth and on the dispersion slope. An example of design improvement will be discussed later in this chapter.

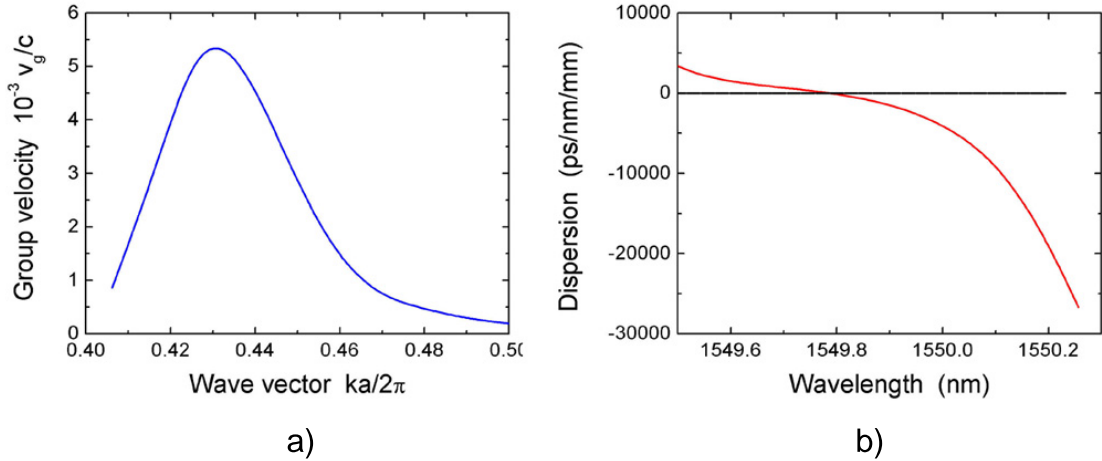


**Figure 3.8:** a) Group velocity and b) dispersion within the PPC waveguide presented in 3.5. The lattice constant ( $a = 474$  nm) is chosen in order to position the 0.4 nm-bandwidth (40 GHz) around the central wavelength 1550 nm in the guided region of the defect mode.

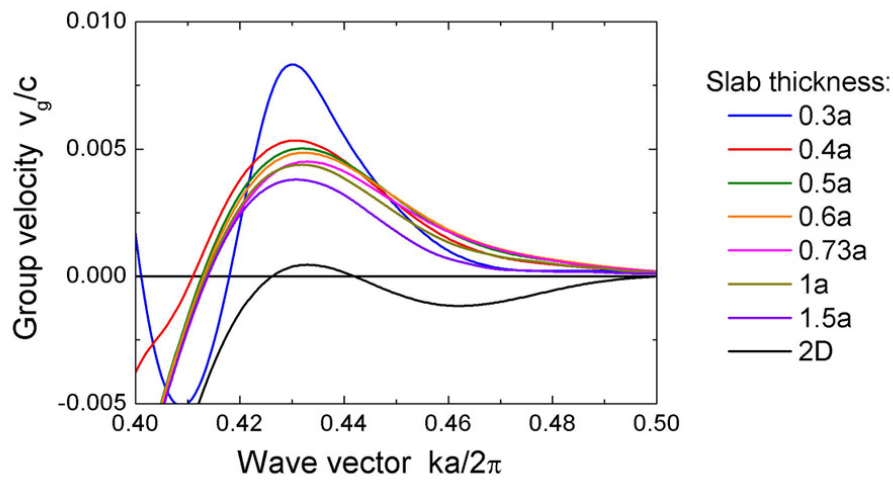


**Figure 3.9:** Variations of the group velocity with the relative core thickness for the lowest defect mode of the W1 waveguide in an IOSOI PPC with relative pore radius  $r/a = 0.366$ . The oxide claddings are supposed to be semi-infinite.

From an experimental point of view, it is crucial to know how robust the dispersion slope is towards variations of the geometrical parameters of the PPC. The variations of the group velocity with the slab thickness, pore radius, and cladding thickness are presented in fig. 3.9, 3.10, and 3.11, respectively.

Fig. 3.9 shows that the group velocity value decreases very slightly with increasing slab thickness for thicknesses  $h/a > 0.4$ . The negative value observed for the limiting case of infinite slab thickness is probably due to an interaction with another band, that is coming closer to the defect band of interest with increasing slab thickness. For thin slabs with relative thickness below  $0.4 a$ , the group velocity value increases in a much stronger way. This result means that we have to work with relative thicknesses slightly above  $0.4 a$ , such that small deviations of the experimental thickness from the theoretical value do not lead to any consequent change in the group velocity (resp. dispersion) value. For a relative thickness deviation from  $0.4$  to  $0.5 a$ , the

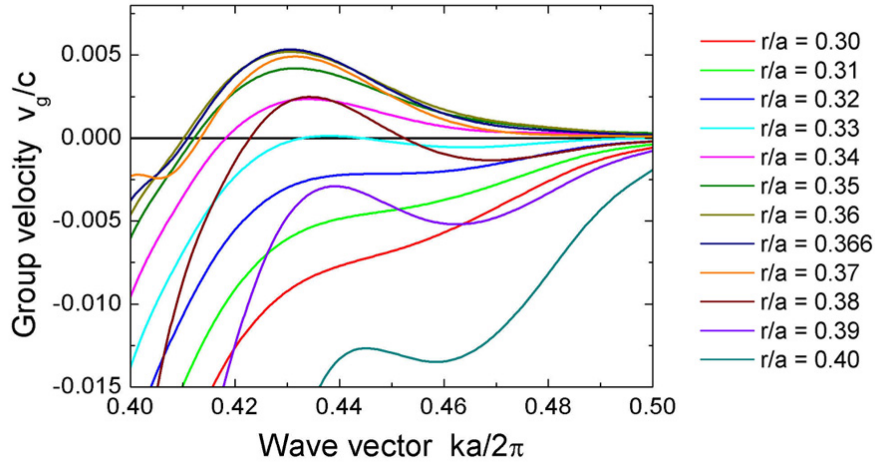


**Figure 3.10:** Variations of the group velocity with the relative radius for the lowest defect mode of the W1 waveguide in an IOSOI PPC with relative thickness  $h/a = 0.4$ . The oxide claddings are supposed to be semi-infinite.

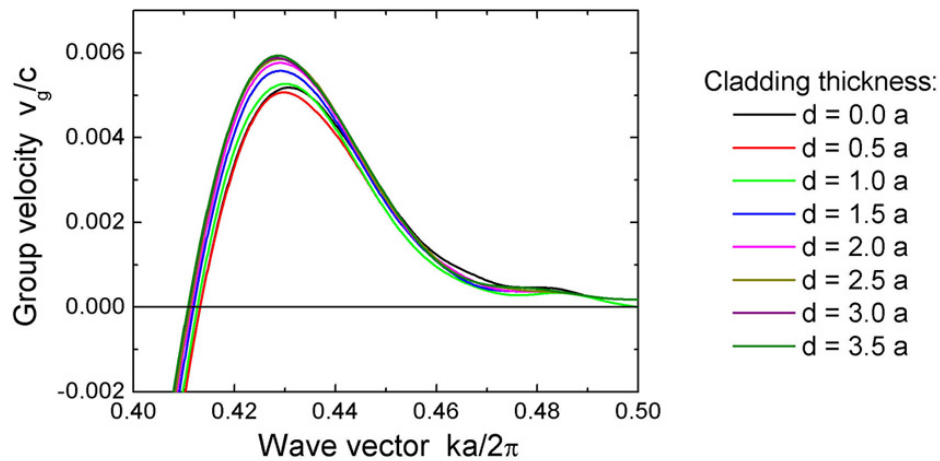


**Figure 3.11:** Variations of the group velocity with the relative cladding thickness for the lowest defect mode of the W1 waveguide in an IOSOI PPC with relative thickness  $h/a = 0.4$  and relative pore radius  $r/a = 0.366$ .

variation of the group velocity at its maximum around  $ka/2\pi = 0.43$  is less than 9 %.

If we consider now the variations of the group velocity with increasing pore radius, we can observe a quite different behavior (fig. 3.10). Indeed, for small radii, the group velocity is negative and almost linear in the wave vector range  $ka/2\pi = 0.43-0.50$ . Its absolute value decreases with increasing radius to become almost zero for  $r/a = 0.33$ . For relative radii above 0.33, the group velocity is positive with a maximum for relative wave vectors around 0.43. It increases up to  $5.2 \cdot 10^{-3}$  for a relative radius  $r/a = 0.366$ , and then turns down again very fast to negative values with a strongly modulated slope. This result means that the most stable group velocity (resp. dispersion) slope and value are obtained for a relative radius  $\sim 0.366$ . For relative radii between 0.36 and 0.37, the largest deviation in group velocity is less than 9 %.

The variations of the group velocity with increasing cladding thickness are presented in fig.

3.11. Since the defect mode is well confined within the silicon slab, its slope is not very sensitive to the cladding thickness. When the cladding thickness is increased from zero (corresponding to a membrane structure) to infinity, the variation of the group velocity at its maximum for relative wave vectors around 0.43 is less than 16 %. Therefore, the cladding thickness is not a crucial parameter in this special case.

## 3.2 Propagation Losses

Once we have selected a preliminary waveguide design, it is important to determine the propagation losses through this waveguide and to improve the design if necessary, in order to minimize the losses. In addition to the losses due to experimental imperfections, two main sources of losses play a role in the waveguide: the radiation losses above the light line and the losses resulting from a coupling between the defect mode and the bulk modes. These two types of losses will be addressed below.

### 3.2.1 Radiation Losses

In section 2.3, we have already shown that working above the light line leads to tremendous losses. However, the introduction of a line defect into the PC lattice should lead to variations of the losses compared to the case of a bulk PPC. In the following, we will quantify the radiation losses for the W1 waveguide consisting of one row of missing pores in an IOSOI PPC.

Similarly to bulk modes, above the light line the defect modes become resonant, i.e., they are still guided in the plane along the line defect but they are leaky in the vertical direction. Due to intrinsic radiation losses, the light transmission through waveguides based on defect modes above the light line can be quite low. Fig. 3.12a shows the band structure of a photonic crystal waveguide having a relative silicon thickness  $h/a = 0.3$ , all the other parameters being the same as in fig. 3.5. The corresponding transmission through this waveguide with  $30a$  (resp.  $40a$ ) length is presented in fig. 3.12b. The calculation takes into account light in- and out-coupling to the photonic crystal waveguide through a ridge waveguide having the same width and the same effective indices, leading to coupling losses of around 50 %. The relative frequency range shown ( $\omega a/2\pi c = 0.32-0.44$ ) corresponds to the photonic band gap of the crystal. Only the two defect bands with laterally odd symmetry are shown in the band structure, separated by a mini stop gap for relative frequencies around 0.405. Considering the light line of the cladding system (black line), we can verify that the first defect mode is guided only in the wave vector range  $ka/2\pi = 0.4-0.5$ , which corresponds to a very small frequency range. The main part of the lower defect band in fig. 3.12 (for wave vectors below 0.4), contributing to the transmission, is resonant. From the difference in transmission between the two waveguide lengths, the attenuation due to radiation losses is estimated to be in the order of 100 dB/mm for a lattice constant of 500 nm. This estimation is in good agreement with theoretical predictions [81] as well as experimental measurements on W1 waveguides in silicon [82].

As in the case of bulk modes, the radiation losses can be calculated directly using the effective-index plane-wave method with complex frequencies. Fig. 3.13a and 3.13b show the band structure and the imaginary part of the frequency, respectively. Using equation 2.3, the intrinsic losses within the photonic crystal waveguide can be deduced. They are plotted in fig. 3.13c. It can be recognized that the losses of the lowest defect mode are in the order of 100 dB/mm on average, as predicted from the transmission calculation. When the wave vector increases

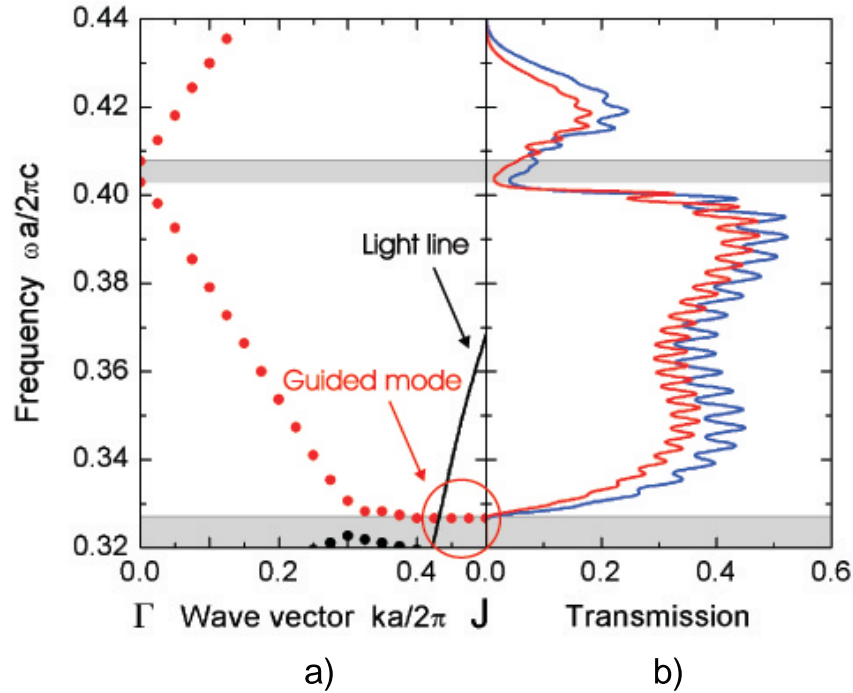


**Figure 3.12:** a) Band structure for laterally odd modes of a photonic crystal waveguide having a relative silicon thickness  $h/a = 0.3$  and all other parameters like in fig. 3.5 (3D FDTD calculation with open boundary conditions on the top and the bottom of the structure, by C. Hermann [71]). Only the relative frequency range between 0.32 and 0.44 is shown, corresponding to the photonic band gap of the crystal. The grey regions correspond to the frequency regions within the photonic band gap where no defect mode exists. b) Transmission through the waveguide with 30 (blue line) and 40 (red line) lattice constants length, respectively. The light is coupled in and out through a ridge waveguide having the same width and the same effective indices as the photonic crystal waveguide.

towards the J point, the band crosses the light line and becomes guided. As expected, this corresponds to a very fast decrease of the losses. Above the light line, at the other band edge, while reaching the mini-stop gap at the  $\Gamma$ -point, the slowing down of the group velocity leads to a large increase of the radiation losses. The same phenomena is observed at the lower limit of the band gap for relative frequencies around 0.335 (corresponding to the black mode in the band structure).

Considering now the upper defect mode, the transmission is very low, as illustrated in fig. 3.12. This mode is entirely resonant and shows strong radiation losses ( $\approx 200$ -300 dB/mm). This value is confirmed in fig. 3.13.

Comparing fig. 3.13 with fig. 2.14, we can notice that the radiation losses in the W1 waveguide are much lower than in the case of the bulk modes. This can be explained by the fact that in the W1 waveguide, the modes are confined laterally within the waveguide and do not extend a lot into the patterned regions. Since radiation losses occur essentially in the air pores, the losses are lower in our W1 waveguide made of one row of missing pores than in the bulk lattice.

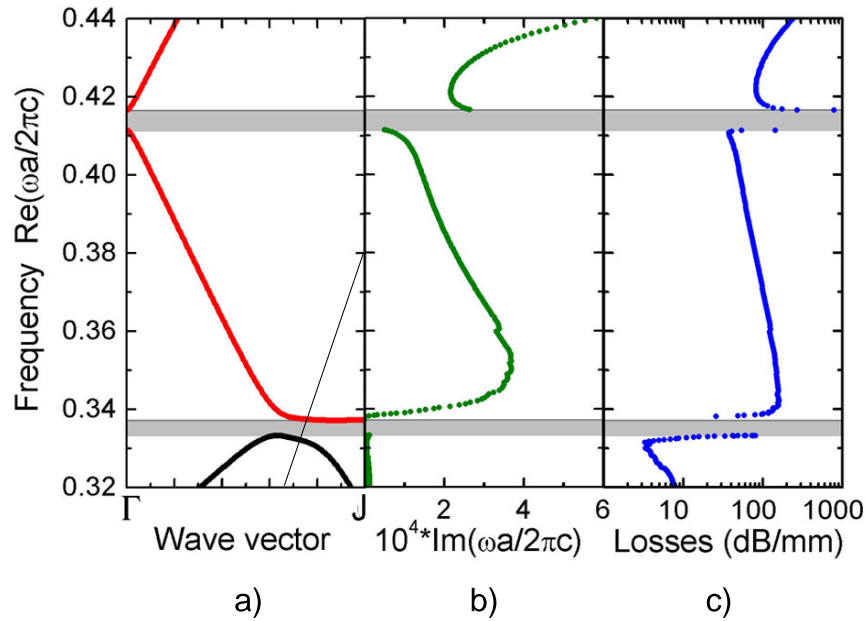


**Figure 3.13:** a) Band structure of the same photonic crystal waveguide as in fig. 3.12. The black mode is the bulk mode limiting the band gap from the bottom and the red modes are the two defect modes with laterally odd symmetry. The straight black line indicates the position of the light line. b) Imaginary part of the frequency and c) corresponding intrinsic losses (2D plane-wave calculation with effective indices [68, 81]). The small frequency shift observed while comparing with fig. 3.12 comes from the fact that the two methods used converged towards slightly different values.)

### 3.2.2 Coupling to Bulk Modes

Considering fig. 3.5, we can notice that the defect band is located very close to the lower edge of the band gap in the region of guided modes. Therefore, it may be leaky due to coupling to the bulk modes, and is very sensitive to fabrication disorder. Indeed, small deviations of the experimental parameters from the theoretical values could lead to a shift of the defect mode towards slightly lower frequencies, and to its coupling with the bulk modes limiting the band gap from the bottom. Consequently, to minimize the propagation losses, it is necessary to avoid the risk of coupling to bulk modes and to shift the defect mode towards slightly higher frequencies.

A way to shift the defect mode towards the middle of the band gap is to reduce the defect width [53]. Due to the higher confinement, the frequency of the defect modes increases. The position of the mode within the band gap can be also controlled by varying the diameter of either the holes constituting the line defect or of the holes surrounding the defect [83]. The higher the air fraction around the defect, the higher the frequency of the defect modes.

Due to the periodicity breaking in the  $x$ -direction normal to the defect, line defects with reduced width cannot be studied with codes assuming periodic boundary conditions on all lateral sides of the computational supercell, like the MIT package or the FDTD code widely used in this work. They can be studied, e.g., using a FDTD method with perfectly matched layers boundary conditions on the sides of the computational supercell parallel to the propagation direction ( $(y, z)$ -interfaces if the propagation direction is the  $y$ -direction) [53]. However, such a code was not available. Therefore, in the following, we focus our attention on the W1 waveguide with increased pore radius along the defect.

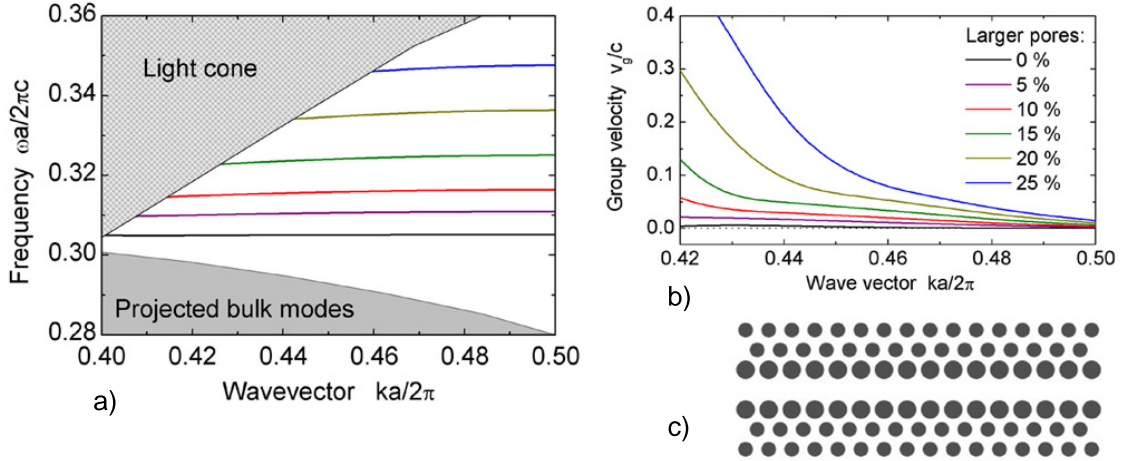


**Figure 3.14:** Variations of a) the defect band position and b) its group velocity when the radius of the pore row on both sides of the W1 waveguide is increased. The defect band considered is the lowest defect band within the band gap of the W1 waveguide consisting of one row of missing pores, in an IOSOI PPC with relative core thickness  $h/a = 0.4$  and relative pore radius  $r/a = 0.366$ . The claddings of the PPC are assumed to be infinite. (MIT package calculation [47]). c) Design of the waveguide (schematics).

The variations of the defect band position and its group velocity, when the radius of the pore row on both sides of the W1 waveguide is increased, are presented in fig. 3.14. The defect band considered is the lowest defect band within the band gap of the W1 waveguide consisting of one row of missing pores, in an IOSOI PPC with relative core thickness  $h/a = 0.4$  and relative pore radius  $r/a = 0.366$ . The claddings of the PPC are assumed to be infinite. As can be observed in fig. 3.14, a change as small as 5 % (resp. 10 %) of the pore radius along the defect induces already a large shift of 0.006 (resp. 0.011) of the defect band towards higher relative frequencies. This shift would be very convenient if the group velocity slope would not vary in an even stronger way. Indeed, for a pore radius variation of 5 % (resp. 10 %), the group velocity value increases by a factor of 4 (resp. 20) in the relative wave vector range around 0.43. Furthermore, for pore radius variations larger than 10 %, the maximum in group velocity for relative wave vectors around 0.43 disappears, and, consequently, the dispersion is positive within the whole wave vector range.

Because of the strong increase of the band curvature, the increase of the pore radius along the line defect is limited. We select an increase of 5 % (corresponding to a relative radius  $r/a = 0.385$ ) as a good compromise between low group velocity, negative dispersion, and low risk of coupling to the bulk modes.

As shown in fig. 3.15, the small increase in the pore radius along the defect results simultaneously in an improved dispersion slope. The dispersion value for this design is -30 ps/nm/mm at 1.55  $\mu\text{m}$  wavelength, for a total dispersion compensation  $\Delta D$  of 35 ps/nm/mm over the 40 GHz bandwidth. This allows to compensate for the dispersion of 1 km SMF (17 ps/nm/km) within 0.5 mm of PPC waveguide. This dispersion value is low but more convenient than the high value obtained for the initial design, since the resulting larger waveguide length leads to a device that is more stable and robust against any experimental deviations.

Although the dispersion slope is still slightly convex, it is almost linear over a larger wavelength range than in the case of the initial design, which exceeds the necessary 0.4 nm-bandwidth. Therefore, the properties of this new design are closer to the device requirements in terms of

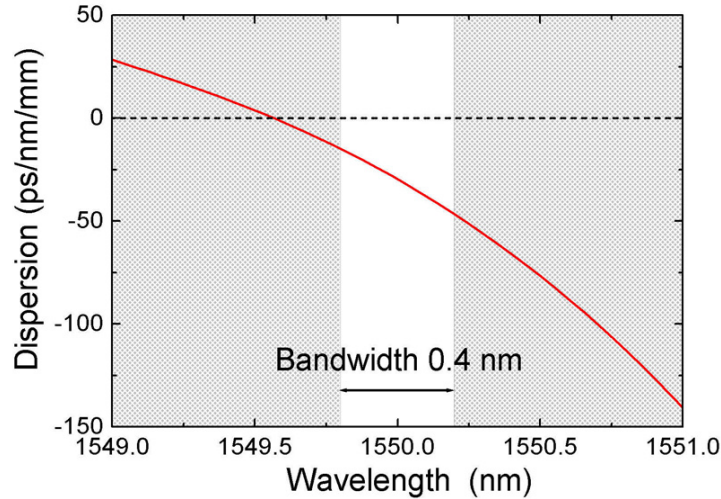


**Figure 3.15:** Dispersion in the W1 waveguide made of one row of missing pores in an IOSOI PPC with relative thickness  $h/a = 0.4$  and two structured oxide claddings assumed to be semi-infinite. The relative radius of the pores is  $r/a = 0.366$ , with an increase of 5 % (corresponding to a relative radius  $r/a = 0.385$ ) for the pore row on both sides of the waveguide.

dispersion slope and propagation losses, and are more convenient for applications to dispersion compensation. More importantly, it proves that the W1 waveguide made of one row of missing pores is a design suitable for dispersion compensation, which could certainly be improved further to satisfy all device requirements. However, we will not perform any further improvement of the design yet, since the aim of this study is to prove that W1 waveguides in PPCs can be used *in principle* for applications to dispersion compensation. In that sense, this design is already satisfying.

After fabrication, the variation of the defect mode position can also be achieved through different ways of tuning, as will be presented in the next section.

### 3.3 Tunability

Since the fabrication tolerances are always higher than the precision necessary for pulse reshaping, the device needs to be tuned after fabrication to the required wavelength range. To date, tuning and trimming of dispersion compensators is carried out by mechanical stress. However, the possible range is very limited and this represents a reliability issue. Photonic crystals offer the unique possibility that their dispersion properties can be tuned after fabrication without altering the temporal stability of the material properties. Indeed, the particular location of the field intensity, as well within the dielectric as within the pores (fig. 3.5), allows different ways of tuning the dispersion properties of the photonic crystal waveguides after fabrication. Electrical or optical injection of free carriers allows the adjustment of the refractive index of the dielectric (here silicon). Tuning can also be achieved by infiltration of electro-optic or birefringent materials into the pores of the PPC. In the following, these two ways of tuning will be discussed: tuning by infiltration of liquid crystals into the pores, and tuning by free carriers injection.

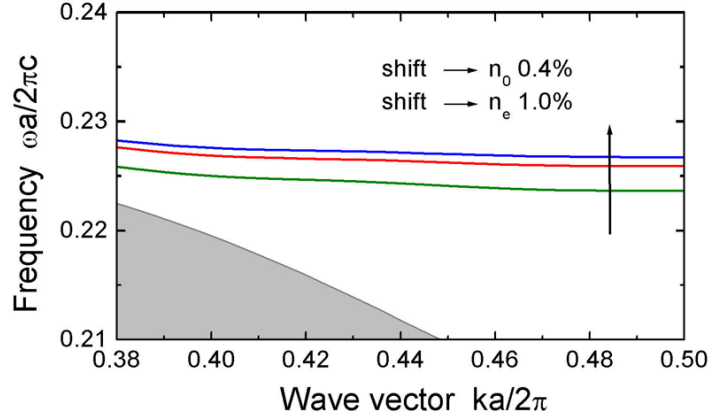


**Figure 3.16:** Variations of the band structure of a W1 waveguide made of one row of missing pores in an infinite 2D PC of filled pores in silicon. The pores with radius  $r/a = 0.366$  are filled with liquid crystals having a refractive index  $n_i = 1.55$  in the isotropic phase (red lines),  $n_o = 1.5$  and  $n_e = 1.67$  in the nematic phases along the ordinary (blue lines) and extraordinary axis (green lines), respectively (MIT package calculation [47]).

### 3.3.1 Liquid Crystal Infiltration

By infiltration of electro-optic or birefringent materials into the holes of the dielectric structure, tuning can be achieved. In particular, liquid crystals can lead to a significant change of the dispersion properties. Our study of the tuning effect has been first performed for deep 2D photonic crystals in macroporous silicon, theoretically as well as experimentally [90, 91]. By tilting the alignment of the liquid crystals from the isotropic phase (with refractive index  $n_i = 1.55$ ) to the nematic phase (with refractive index  $n_o = 1.5$  and  $n_e = 1.67$  along the ordinary and extraordinary axis, respectively), an absolute change in the refractive index of at least  $\Delta n = 0.1$  can be achieved. In the case of infinite 2D PCs, the corresponding variations of the defect bands position is shown in fig. 3.16. A shift of the defect band up to 1 % in relative frequency can be achieved. However, such a large shift is not very convenient, because it leads to a corresponding shift of the bandwidth. In the region suitable for dispersion compensation, the defect band is so flat that the bandwidth is very small. If the defect band position is shifted too much at a given wavelength, the band is not excited anymore in the flat region of interest, leading to a completely different dispersion property. This is illustrated in fig. 3.17: the large variation of the defect band position with the refractive index in the pores leads to the large shift of the bandwidth, and therefore of the dispersion slope, observed in fig. 3.17a. At the given wavelength 1550 nm, three different regions of the defect band are excited. Consequently, large changes in the dispersion value occur, as shown in fig. 3.17b. To achieve a good adjustment of the dispersion properties by tuning, the variation of the defect band position must be well controlled and very small.

Two other problems with the liquid crystal tuning emerge while going to the 3D case of a planar PPC. For the particular case of the IOSOI PPC, the filling of the pores leads to a shift of the light line towards smaller frequencies, because the oxide claddings having a similar refractive index as the liquid crystals are filled simultaneously. Even if a part of the defect band is still below the light line, the working area suitable for dispersion compensation is drastically reduced, and very close to the light line, as illustrated in fig. 3.18a.

Furthermore, the variations of the dispersion with the refractive index in the pores are very strong. The dispersion curve is not only shifted in wavelength as it was the case for an infinite

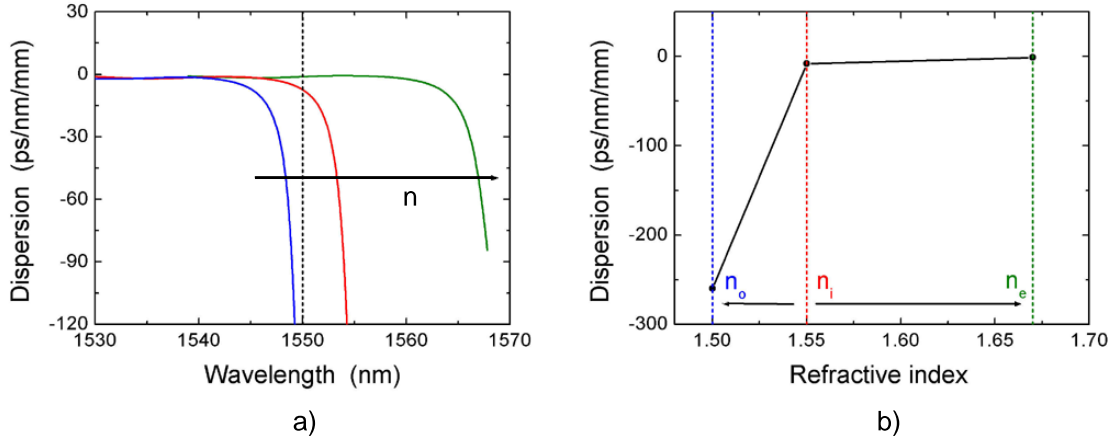


**Figure 3.17:** Change of the dispersion  $D$  with gradual tuning of a liquid crystal infiltrated into the pores of the same W1 waveguide as in fig. 3.16. The lattice constant is chosen to be  $a = 350$  nm. The liquid crystals have a refractive index  $n_i = 1.55$  in the isotropic phase (red lines),  $n_o = 1.5$  and  $n_e = 1.67$  in the nematic phases along the ordinary (blue lines) and extraordinary axis (green lines), respectively. a) Shift of the dispersion slope with the wavelength and b) shift of the dispersion value at 1550 nm wavelength (MIT package calculation [47]).

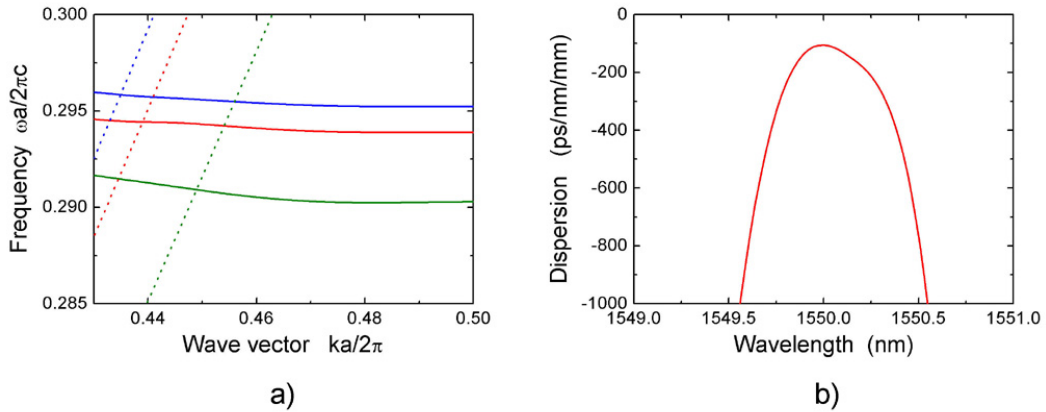


**Figure 3.18:** a) Variations of the band structure of a W1 waveguide made of one row of missing pores in an IOSOI PPC with relative silicon thickness  $h/a = 0.4$ . The pores with radius  $r/a = 0.366$  are filled with liquid crystals having a refractive index  $n_i = 1.55$  in the isotropic phase (red lines),  $n_o = 1.5$  and  $n_e = 1.67$  in the nematic phases along the ordinary (blue lines) and extraordinary axis (green lines), respectively (MIT package calculation [47]). The dotted lines indicate the position of the corresponding light line for each refractive index value. b) Dispersion for the isotropic case with  $n_i = 1.55$ . The lattice constant is assumed to be 450 nm.

photonic crystal; in the case of the IOSOI system the whole dispersion slope is varying. If the lattice constant is assumed to be 450 nm, the dispersion around 1550 nm wavelength is decreasing for the refractive index  $n_o = 1.5$ , whereas it is increasing for  $n_e = 1.67$  and reaches a maximum for the isotropic phase with  $n_i = 1.55$ . This last case is shown in fig. 3.18b.

Therefore, the infiltration of the pores with a tunable material is not convenient for applications to dispersion compensation, because it leads to a shift of the light line towards lower frequencies and to a strong modification of the dispersion properties of the defect band. Similar results are expected with a coating of the pore walls, instead of a complete infiltration. For exam-

ple, coating with ferroelectric materials is currently studied in the case of infinite 2D PCs of macroporous silicon [92]. In the IOSOI PPC-based DC working at 1550 nm wavelength, the pore radius is very small (160 nm). Since the minimal coating thickness achieved to date for ferroelectric materials is 50-100 nm, this configuration is close to the case of a complete pore filling, and a similar behavior is expected. Therefore, it may be more promising to tune the dielectric constant of the silicon layer via free carrier injection. The study of this way of tuning is presented in the next section.

### 3.3.2 Free Carrier Injection

Using free carrier injection as a tuning procedure, the two problems encountered in the case of liquid crystal infiltration could be avoided. By free carrier injection, the refractive index of the silicon can be adjusted [93, 94] with no changes in the refractive index of the cladding material, since the oxide is an insulator. Consequently, tuning by free carrier injection induces no variation in the light line position. Furthermore, free carriers injection can be controlled very accurately, and very small changes in the refractive index of silicon can be achieved. As discussed already in the case of liquid crystal infiltration, the extreme flatness of the defect band allows only very small variations of the defect band position. Otherwise, the tuning would result in an excitation of the defect band at completely different positions for a fixed wavelength, with the two disadvantages that one of these positions would necessarily lie above the light line and the dispersion properties would be completely different.

Free carriers injection can be obtained either optically, e.g., by illuminating the PPC from the side with a laser beam, or electrically by applying an electrical field, via a p-n junction or a Schottky barrier. In both cases, electrons and holes are created in the silicon. The presence of these additional free carriers induces a change in the dielectric function  $\varepsilon$  of the silicon. Consequently, the refractive index of silicon is also changed. If the density of the free carriers is sufficiently small, their absorption can be neglected [95]. Therefore, the variation of the dielectric constant of the silicon follows Drude's equation:

$$\varepsilon(\omega) = \varepsilon_b - \frac{\omega_p^2}{\omega^2} \quad (3.1)$$

with the plasma frequency  $\omega_p$  given by

$$\omega_p^2 = \frac{Ne^2}{\varepsilon_0 m^*} \quad (3.2)$$

where the effective mass  $m^*$  is very close to  $m_0^*$ . The dielectric constant is thus a function of both the frequency  $\omega$  and the plasma frequency  $\omega_p$ , which is a function of the plasma density  $N$ , as can be deduced from equation 3.2. Therefore, the dielectric constant of the silicon can be controlled by varying the plasma density, which is achieved by free carrier injection. The variations of the band structure with the silicon dielectric constant are shown in fig. 3.19. A reduction of the dielectric constant from  $\varepsilon = 11.60$  to  $\varepsilon = 11.59$  induces a shift of the defect band of 0.035 % towards higher frequencies. Reducing further the dielectric constant, the absolute shift of the band varies quite linearly and its slope is preserved. Due to the very small tuning, no significant change in the general dispersion slope is observed compared to fig. 3.8, except a shift in wavelength and a variation of the dispersion value. The corresponding variations of the dispersion are presented in fig. 3.20. The lattice constant is fixed to  $a = 473$  nm. From

fig. 3.20, we can deduce that both the dispersion value  $D$  at the central wavelength and the dispersion compensation  $\Delta D$  over the whole 0.4 nm bandwidth vary first very strongly with decreasing dielectric constant down to  $\varepsilon = 11.58$ , and then only slightly.

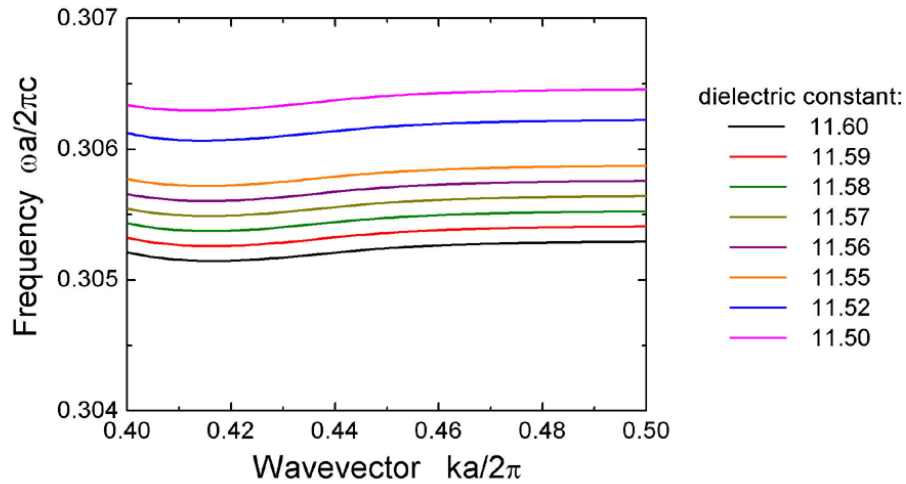


**Figure 3.19:** Effect of the free carriers injection: Shift of the defect band with varying silicon dielectric constant for the W1 waveguide made of one row of missing pores in the IOSOI PPC with relative thickness  $h/a = 0.4$  and relative pore radius  $r/a = 0.366$ . The oxide claddings are assumed to be infinite (MIT package simulation [47]).

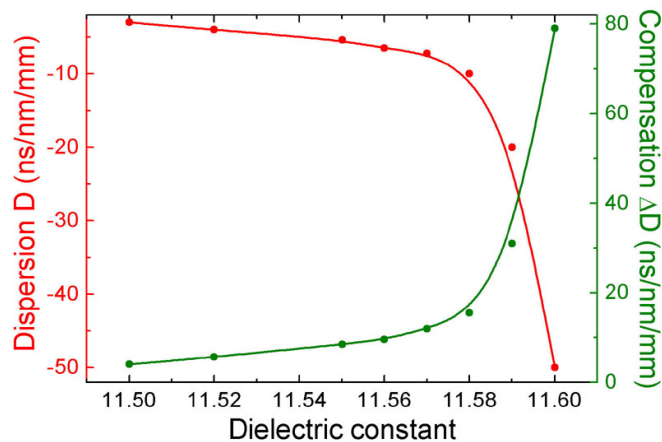


**Figure 3.20:** Dispersion value  $D$  at the central wavelength (red curve), and dispersion compensation  $\Delta D$  over the whole 0.4 nm bandwidth (green curve), as a function of the silicon dielectric constant, in the same W1 waveguide as in fig. 3.19. The lattice constant is assumed to be 473 nm, which is slightly smaller than that of fig. 3.8, in order to shift the dispersion curve towards slightly higher wavelengths (MIT package simulation [47]). This results in the difference in dispersion value compared to fig. 3.8, and put into evidence the high accuracy required for the fabrication of the PPC as well as for the tuning after fabrication.

As was already discussed above, the band is so flat that the bandwidth suitable for dispersion compensation is very small. Any small variation of the defect mode position leads to a shift of the bandwidth. Fig. 3.21 shows the shift of the central wavelength of the bandwidth suitable for dispersion compensation with varying dielectric constant for a fixed lattice constant  $a = 473$  nm. In order to make the tuning procedure functional, the bandwidths after and before

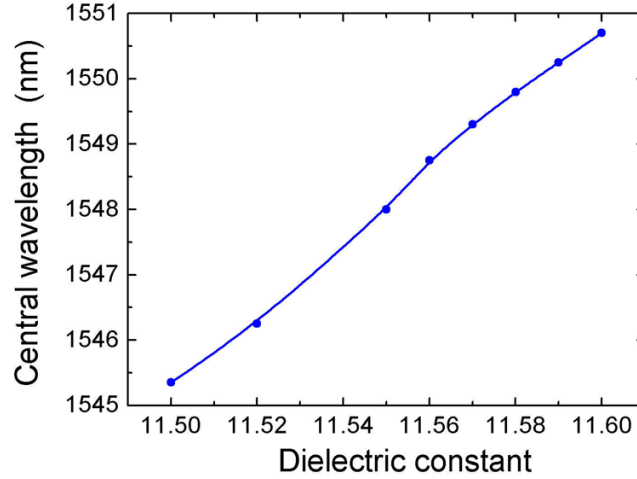


**Figure 3.21:** Central wavelength of the 0.4 nm bandwidth suitable for dispersion compensation, depending on the silicon dielectric constant, for the same W1 waveguide as in fig. 3.19. The constant lattice constant is assumed to be  $a = 473$  nm.

tuning should overlap over at least 0.4 nm. Since the whole bandwidth is not much larger than 0.4 nm, we deduce from fig. 3.21 that the allowed variations of the dielectric constant must be smaller than  $\Delta\varepsilon \leq 0.005$ . This requires very low injection currents in the case of electrical generation of free carriers, and therefore only very low absorption losses induced by the carriers. On the other hand, as can be observed in fig. 3.20, very large dispersion adjustment can be achieved within this very small variation range of the dielectric constant, requiring high accuracy in the tuning setup.

To summarize this section, two different ways of tuning the dispersion properties of the PPC after fabrication have been studied. Tuning by liquid crystal infiltration is not convenient, because it leads to strong changes of the dispersion properties and to a shift of the light line towards lower frequencies, reducing the working area. In contrast, tuning by free carrier injection allows variations of the defect mode position without shift of the light line. Although this method requires very high accuracy, very large dispersion adjustment can be achieved with variations of the dielectric constant as small as  $\Delta\varepsilon \leq 0.005$ , where absorption can be neglected.

### 3.4 Coupling Issues

An important issue for the functionality of waveguides is light in- and out-coupling. The coupling of light from the optical fiber into the integrated circuit containing the DC, and back to the optical fiber, has to be as good as possible to avoid tremendous losses. In the case where the DC is integrated into a chip together with other optical devices, the light is first coupled from the SMF into an integrated ridge waveguide and then from the ridge waveguide into the PPC. The ridge waveguides used in this work are chosen to be very narrow with similar geometrical parameters as the PPC waveguide, in order to achieve single-mode propagation. The coupling between the external light beam coming from the SMF and the ridge waveguide is well known and has already been optimized, e.g., by means of microlenses and/or optical tapers [84]. We will not discuss this issue here, since it is not the subject of this work. In the following, we will focus on the coupling between the ridge waveguide and the PPC. In particular, three different parameters have to be taken into account for a good coupling: impedance matching, mode

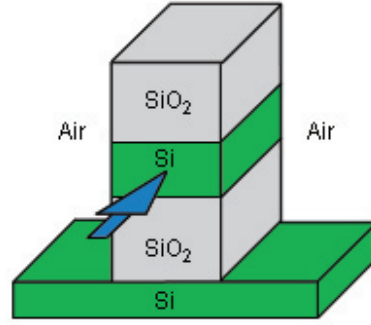


**Figure 3.22:** Principle of a ridge waveguide integrated into the IOSOI chip for light in- and out-coupling into the PC waveguide. Light is confined within the silicon core. The blue arrow indicates the direction of light propagation.

matching and band flatness.

### 3.4.1 Impedance Matching

A large source of coupling losses between two waveguides is the impedance mismatch. Due to the difference between the effective indices of core and claddings in the two waveguides, a part of the light is reflected at the coupling interface. In classical optics, the wave impedance is given by

$$Z = \frac{1}{n} \cdot \sqrt{\frac{\mu_0}{\epsilon_0}} \quad (3.3)$$

and the reflection and transmission coefficients  $R$  and  $T$ , at the interface between two media of indices  $n_1$  and  $n_2$  and impedances  $Z_1$  and  $Z_2$ , are, respectively

$$R = \frac{(Z_1 - Z_2)^2}{(Z_1 + Z_2)^2} = \frac{(n_1 - n_2)^2}{(n_1 + n_2)^2} \quad (3.4)$$

$$T = \frac{4Z_1 \cdot Z_2}{(Z_1 + Z_2)^2} = \frac{4n_1 \cdot n_2}{(n_1 + n_2)^2} \quad (3.5)$$

in the case of normal incidence.

In our selected design, the integrated ridge waveguide has a silicon core of the same width as the PC waveguide, and is surrounded by air trenches on both sides and silicon oxide layers on the top and bottom sides, as illustrated in fig. 3.22. Compared to the PPC waveguide, the thicknesses of the different layers as well as their effective indices are similar. The only difference comes from the IOSOI bulk PPC on both sides of the PC waveguide, which is replaced by air trenches in the case of the ridge waveguide. This leads to a small impedance mismatch. Therefore, some coupling losses due to impedance mismatch are expected.

To determine the effective indices in the ridge waveguide and PPC waveguides, respectively, we consider the inverse of the tangent of the lowest mode at the  $\Gamma$ -point in the band diagram of each waveguide. It leads to an effective index of  $n_{PC} = 1.32$  for the PPC waveguide and  $n_{RW} = 1.08$  for the ridge waveguide. From equation 3.5, we can deduce that the transmission

coefficient at the interface between the two waveguides is around 99 %. This value has to be considered very carefully since it is based on very simple approximations. However, it indicates qualitatively that the impedance matching between the two waveguides is good and the losses due to impedance mismatch are expected to be small.

From an experimental point of view, the effective indices of the two waveguides cannot be changed independently, so that this small impedance mismatch is unavoidable.

### 3.4.2 Mode Matching

Another key issue for mode coupling between two waveguides is mode matching. It includes mode symmetry, extension and profile, as well as propagation mechanism.

As already pointed out earlier, the mode symmetry is crucial. Relatively to the (y,z)-plane of symmetry in the middle of the waveguide, only laterally odd modes can be excited by an external light source (plane wave or guided wave from another waveguide). Furthermore, if the incoming light is TE-polarized or has a vertically even symmetry, it can only couple to vertically even modes, with respect to the (x,y)-plane of symmetry in the middle of the waveguide. In the case of an asymmetric structure with two different claddings, there are no pure even and odd modes anymore. Due to symmetry breaking some "odd-like" modes may be slightly excited by incoming TE-polarized (resp. even) light, leading to additional losses. In particular, a small transmission within the even band gap may occur.

The spatial mode extension is also a crucial parameter. Usually PPC-based waveguides are very narrow (less than  $1 \mu\text{m}$  at  $1.5 \mu\text{m}$  wavelength for W1 waveguides), while the incoming light beam may be quite broad (a few  $\mu\text{m}$  for a single-mode fiber or a large ridge-waveguide). Therefore, the overlap between the energy distributions of the incoming wave and the excited PPC mode is low, leading to low transmission. A way to decrease the mode extension mismatch is to use a taper, or "spot-size converter". If the ridge-waveguide width is large, the smooth reduction of the mode extension from a large beam to a narrow one allows good coupling of the light from the external waveguide into the PPC waveguide [85]. Another method consists in focussing the beam into the PPC waveguide, e.g., by means of a J-coupler [86]. In our case, the ridge waveguide is very narrow with similar geometrical parameters as the PPC waveguide. In this case, simple butt-coupling, i.e., direct coupling without additional device between the two waveguides, is often considered and yields transmission efficiency up to 80 % in SOI-based systems [87, 88].

Even if both modes have the same symmetry and a similar mode extension, a large difference in the field distributions leads to bad coupling. Therefore, we have to take care that the overlap between the region of high energy of the propagating modes in both in- and out-waveguides are good. Since both waveguides are single-mode, good coupling will be obtained when the propagating modes in both waveguides have similar field distributions.

The last mode property that may be of crucial importance is the propagation mechanism. As already discussed in section 1.3.2, two different guiding mechanisms coexist in PC waveguides. The first one is based on classical index-guiding and the second one on the existence of the band gap. To allow a good coupling between the modes of two waveguides, it is necessary that both of them are guided by the same mechanism [89]. Therefore, butt-coupling from the ridge-waveguide into the PPC waveguide may lead to high losses in our special case, because the ridge-waveguide mode is index-guided and the W1 mode of interest is PBG-guided.

Consequently, from the point of view of mode matching for the coupling between the ridge

waveguide and the PPC waveguide, a taper may be necessary. In particular, the taper to be designed has to allow a smooth conversion from an index-guidance to a PBG-guidance.

### 3.4.3 Band Flatness

Due to the extreme flatness of the defect band below the light line, the coupling from an external light source is expected to be very low. This is related to the group velocity mismatch between the incident mode and the PC mode.

If the incident wave is propagating in a medium with effective refractive index  $n$  - e.g., an integrated ridge waveguide or an optical fiber - the group velocity of the wave is

$$v_{gi} = \frac{c}{n} \quad (3.6)$$

Thus, typically:

$$10^{-1}c \leq v_{gi} \leq c \quad (3.7)$$

As presented above, the group velocity inside the PC waveguide in the guided region is

$$10^{-3}c \leq v_{gPC} \leq 10^{-2}c \quad (3.8)$$

leading to a group velocity mismatch of around two orders of magnitude.

Therefore, to build a functional device, for application, e.g., to dispersion compensation, it is necessary to insert a taper improving the coupling between the ridge waveguide and the W1 waveguide. The taper should allow a smooth slowing down of the group velocity. This can be achieved by a smooth reduction of the defect width [96]. Indeed, in the region above the light line, the defect mode has a high group velocity, as in a ridge waveguide. Therefore, if the incident light from the ridge waveguide is coupled to the PPC defect mode in this region, the coupling should be quite good. As shown schematically in fig. 3.23, the position of the defect mode in frequency decreases with increasing defect width. If the taper consists of a waveguide with slightly larger width (e.g., W1.5) in its outer part, the incoming light will excite the waveguide mode in its region with large group velocity. Then, a very smooth reduction of the waveguide width, down to the W1, would lead to an adiabatic conversion of the waveguide mode to the extreme band flatness suitable for dispersion compensation, as illustrated in fig. 3.23. The design of such a taper is shown schematically in fig. 3.24.

The kind of taper presented above shows the advantage of reducing simultaneously the coupling losses due to mode mismatch. Indeed, the requirement on smooth conversion from an index-guidance to a PBG-guidance is also fulfilled simultaneously in the taper presented above. In the region of high group velocity, the defect mode is index-guided. Consequently, the incoming index-guided light is coupled to an index-guided mode, and then converted to a PBG-guided mode through the taper. Therefore, in our DC design, we choose to insert this kind of taper for light in-and out-coupling from the ridge waveguide to the PPC waveguide.

As a direct check of the taper performance, transmission computations through the W1 waveguide and through the taper were performed, using the commercially available CrystalWave software by Photon Design. Because of the extremely low group velocity within the W1 waveguide,

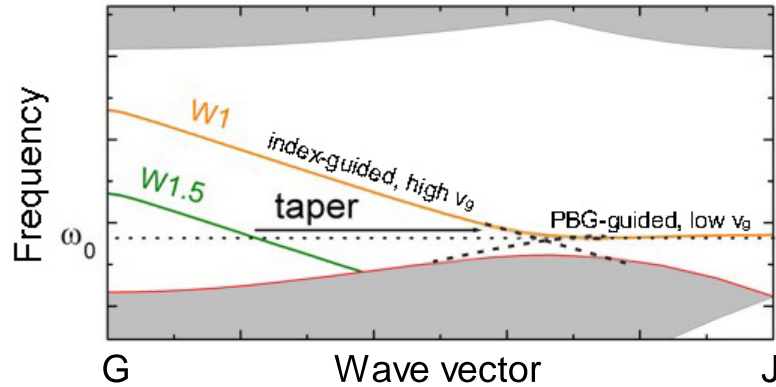


**Figure 3.23:** Schematic variation of defect mode position with the defect width (deduced from MIT package calculations [47]). At given frequency  $\omega_0$ , the defect band of the W1 waveguide is excited in the region of very low group velocity, while the larger waveguide W1.5 is excited in the region of large group velocity.

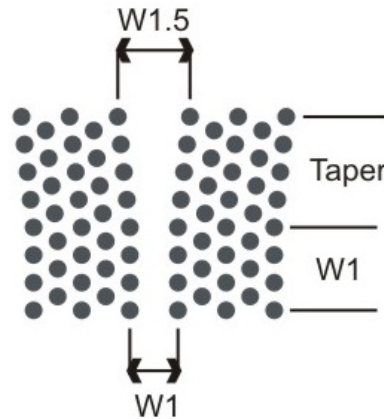


**Figure 3.24:** Principle of a taper based on limited waveguide width reduction ( $W1.5 \rightarrow W1$ ) to improve the group velocity matching as well as the mode matching between the incident wave and the PPC waveguide mode.

the transmission calculations require very long computation time. Therefore, only 2D calculations were performed, with waveguide lengths limited to few pore rows. Fig. 3.25 shows a comparison between the results in the case of a direct coupling through a W1 waveguide having a length of five lattice constants, and a coupling into the same W1 waveguide through a taper having also a length of five lattice constants. The direct coupling of light from the ridge waveguide into the W1 waveguide (fig. 3.25a) leads to very low transmission and strong reflection of the incident light. If the taper is inserted (fig. 3.25b), a clear light propagation can be observed. This result highlights the good functionality of the taper from a qualitative point of view.

In the case of a planar structure, the taper is used above the light line in the region of high radiation losses. However, very limited radiation losses are expected, because the small variation of the waveguide width requires only a short taper length of few lattice constants. For a taper length of  $5a$ , where the lattice constant  $a$  is typically around 500 nm, the radiation losses should be as low as 0.2-0.3 dB, for a transmission efficiency above 80 %. A larger 3D study, to be performed in the future, will allow a quantitative investigation of the taper efficiency.

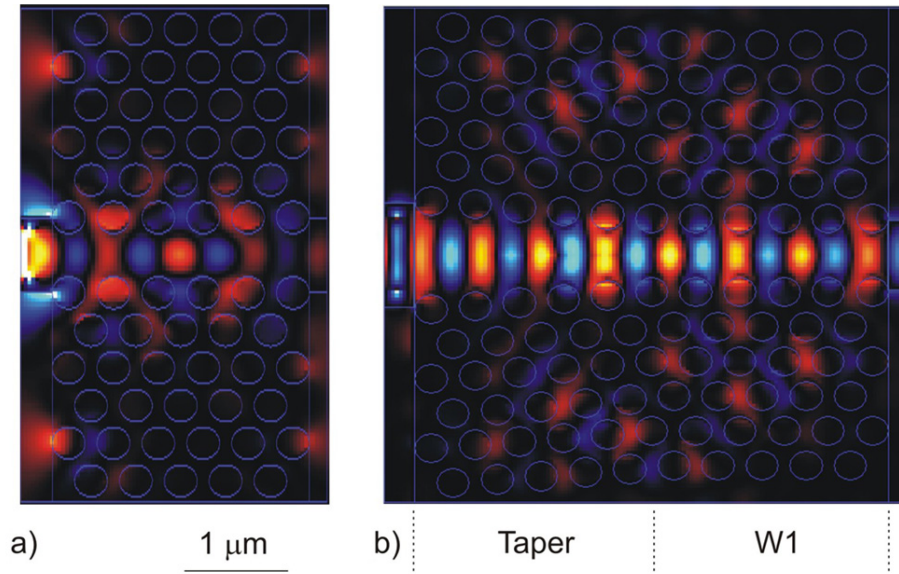


**Figure 3.25:** Comparison between light propagation through a) the W1 waveguide and b) the taper. Butt coupling of light from the ridge waveguide into the PPC waveguide (resp. the taper) is assumed.

### 3.5 Conclusions and Full Design

To summarize the results presented in this chapter, the main issues concerning the design of an integrated PPC-based DC were addressed and solutions were proposed to build a functional device. Within many different types of waveguides, we chose the W1 waveguide consisting of one row of missing pores as a preliminary design for the DC, considering its convenient properties for DC applications: it is single-mode in the frequency range of interest, the group velocity is low, and its slope corresponds to a negative dispersion. A complete 3D study of the properties of this W1 waveguide led to the design of an optimized W1 waveguide with 5 % larger pores on both sides, yielding a negative dispersion of  $-30$  ps/nm/mm at  $1.55$   $\mu\text{m}$  wavelength. Furthermore, the coupling issues were also addressed, and a taper allowing a better light coupling between the W1 waveguide and the ridge waveguides was proposed. Since the tuning of the material properties is very important to adjust the dispersion after fabrication, different methods of tuning were studied in this work, and it was demonstrated that the tuning of the silicon dielectric constant via free-carrier injection is more convenient than that of an infiltrated material into the pores.

As a result of the discussion on all issues addressed in this chapter, a complete design of the integrated dispersion compensating device has been developed. This design will be used as a basis for the experimental fabrication discussed in the next chapter, and is presented in fig. 3.26. The device includes the W1 waveguide as well as two ridge waveguides to guide the light from the other integrated devices or the SMF into and out of the W1 waveguide, respectively. One of the ridge waveguides is S-bent to avoid the overlap between the incident and the compensated beam, that may occur if the coupling of light into the ridge waveguide has some leakage. The radius of curvature of the S-bend is chosen to be  $150$   $\mu\text{m}$ , to ensure that the condition of total internal reflection inside the bent ridge waveguide is fulfilled and the light propagation is lossless.

At both ends of the W1 waveguide, the taper designed in section 3.4 is inserted. On both sides

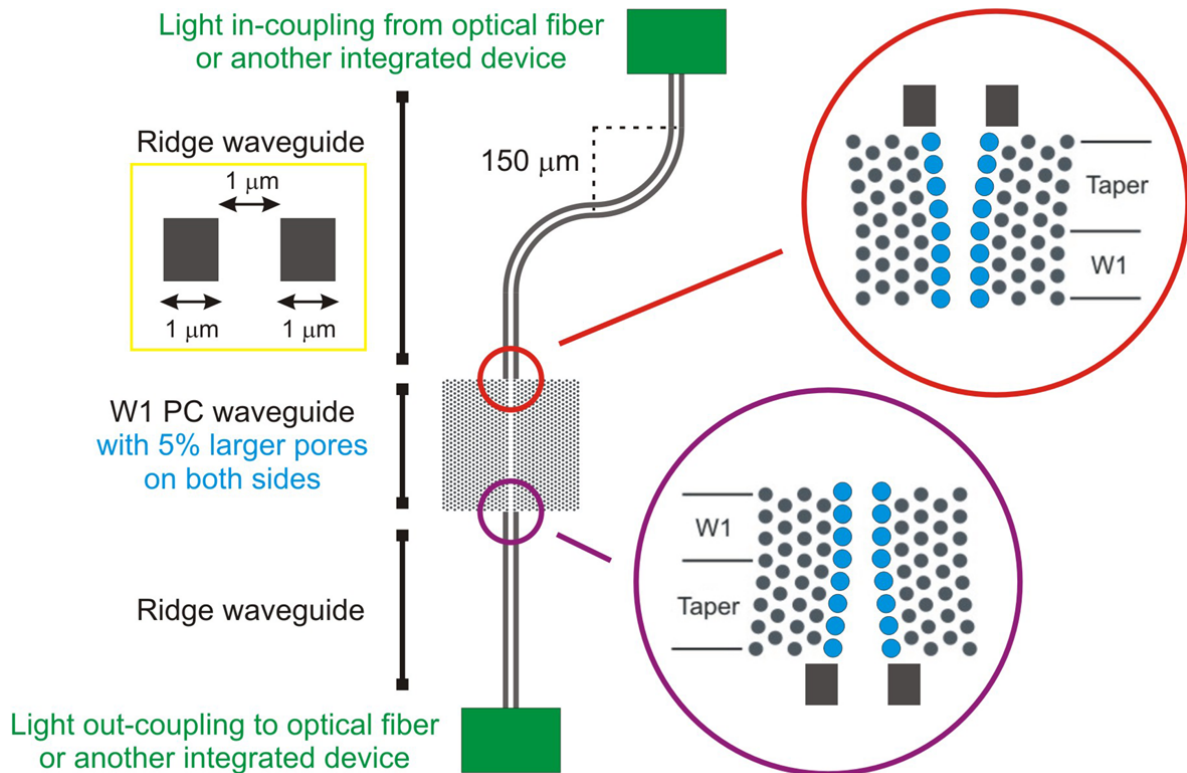


**Figure 3.26:** Full design of the integrated dispersion compensating device. The device includes the W1 waveguide, the two ridge waveguides, as well as the tapers for light in-and out-coupling between the ridge and the PC waveguides. The air pores and air trenches are shown in grey and blue. The radius of the air pores is  $r/a = 0.366$  for the lattice pores and  $r/a = 0.385$  for the larger pores along the waveguide. The thickness of the silicon core is  $h/a = 0.4-0.42$ .

of the W1 waveguide, the radius of the air pores of the row along the defect is 5 % larger than in the PPC lattice (blue pores in fig. 3.26), as discussed in section 3.2.2.

# 4. Experimental Fabrication

The fabrication of the IOSOI PPCs requires the etching of deep pores with very small feature size and high aspect ratio. Although the etching of silicon is well known, deep oxide etching at a submicron scale has never been performed successfully so far. In this chapter, we will show that it is possible to fabricate the IOSOI PPCs. For this purpose, not only the etching process itself, but also several preliminary steps have to be optimized carefully.

## 4.1 Overview on the Fabrication Process

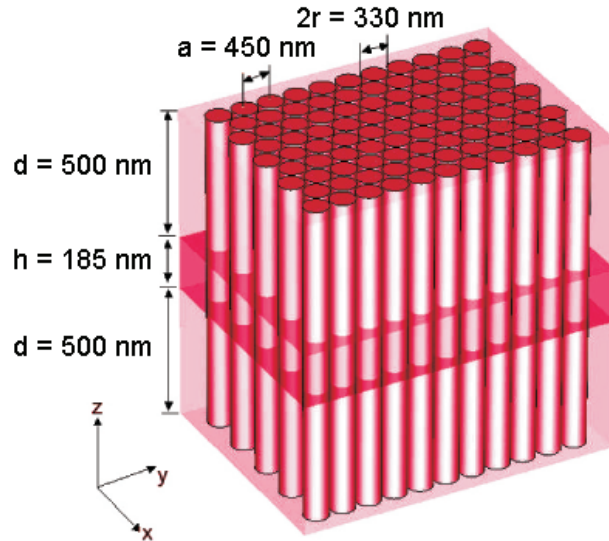
Before designing a fabrication process, it is important to know exactly the experimental parameters of the structure to be fabricated. Several choices depend on these parameters, which are essential for the success of the fabrication, such as the type of lithography process, the nature and thickness of the mask used for the etching, and the type of etching process. To position the flat region of the defect mode at a wavelength of  $1.55 \mu\text{m}$ , the lattice constant of the PC has to be  $a = 450 \text{ nm}$ , leading to a pore radius  $r = 165 \text{ nm}$  and a silicon thickness  $h = 185 \text{ nm}$ . Since an oxidation step is planned to reduce the roughness of the etched pore walls after fabrication, the experimental pore radius should be slightly smaller (around  $150 \text{ nm}$ ). The parameters of the PPC are summarized in table 4.1.

Fig. 4.1 shows a schematic of the PPC with the desired experimental parameters. As can be deduced from fig. 4.1 and table 4.1, the total pore depth is at least  $1.2 \mu\text{m}$ , corresponding to aspect ratios of 4 and 8 for the air pores and the pore walls, respectively. Since it is not possible to achieve such large aspect ratios with the highly isotropic wet etching technique, dry etching is necessary [97]. Two dry etching methods are available in this project, reactive ion etching (RIE) and inductively-coupled plasma (ICP) etching, both of them associated with chlorine-based and fluorine-based gases.

The small features with submicron sizes can not be written by standard photolithography, and reach as well the resolution limit of an available in-line stepper. Consequently, electron-beam (e-beam) lithography is necessary. However, the use of e-beam lithography usually requires a limited resist thickness. Indeed, aspect ratios larger than 1 for the resist patterning are difficult to achieve for most resist types. The resist thickness is thus limited to  $350\text{-}400 \text{ nm}$  for a good patterning of the  $300 \text{ nm}$ -large holes. Taking the above characteristics into account, a direct etching of the deep pores into the three-layer structure  $\text{SiO}_2/\text{Si}/\text{SiO}_2$  is not possible using only a usual resist mask, which would be removed too fast during the process. Therefore, a hard etching mask is necessary.

Lattice constant $a$	Pore Radius $r$	Silicon Thickness $h$	Min. Oxide Thickness $d$
$a = 450 \text{ nm}$	$r/a = 0.366$ $r \approx 150 \text{ nm}$	$h/a = 0.4\text{-}0.42$ $h \approx 185 \text{ nm}$	$d/a \geq 1$ $d \approx 500 \text{ nm}$

**Table 4.1:** Experimental parameters of the IOSOI-based PPC.



**Figure 4.1:** Schematic of the IOSOI-based PPC. The desired experimental parameters are indicated.

Among the available mask materials, the only one that fulfills our requirements is chromium (Cr), because it is hard, strongly adhering to the silicon dioxide, and resistant to the dry etching process with fluorine-based plasmas (commonly used in silicon and silicon oxide etching). Therefore, the etching mask should consist of a chromium layer. After several preliminary trials, we estimated the required chromium thickness to be  $\sim 150$  nm.

The full fabrication process is presented in fig. 4.2. Most corresponding steps were performed in a cleanroom of class 1 [98]. Starting from a commercially available 4" silicon-on-insulator (SOI) wafer (SOITEC SA), with a  $3 \mu\text{m}$ -thick embedded oxide layer and a  $1.5 \mu\text{m}$ -thick upper silicon layer (fig. 4.2a), three thermal oxidation steps were performed to reduce the silicon thickness down to 185 nm, upon which an upper oxide layer of 500 nm was readily obtained (fig. 4.2b). After the first two oxidations, the upper oxide layer was removed by wet etching in a 12.5 % HF bath. Then, the wafer was cleaned and re-oxidized. In the third oxidation step, the 500 nm-thick upper oxide cladding was build, leaving a 185 nm-thick silicon core. Followingly, the 150 nm-thick chromium mask was deposited by sputtering (fig. 4.2c). Thus obtained wafers were subjected to e-beam lithography (fig. 4.2d). Next, the Cr mask was opened by RIE (fig. 4.2e) using the patterned resist as the etching mask. Finally, the pores were etched into the IOSOI structure using a combination of the RIE and ICP etching modes (fig. 4.2f), with the patterned Cr layer as the etching mask. These three steps, e-beam lithography, Cr etching and  $\text{SiO}_2/\text{Si}$  etching, are discussed in more details in the rest of this chapter.

## 4.2 Electron-Beam Lithography

The advantage of e-beam lithography is the high flexibility in the pattern design. Since the pattern is written into the resist point by point without mask, one can modify it before each run. In this section, we will show the most important designs used in this project, followed by the results of the resist patterning by e-beam lithography.

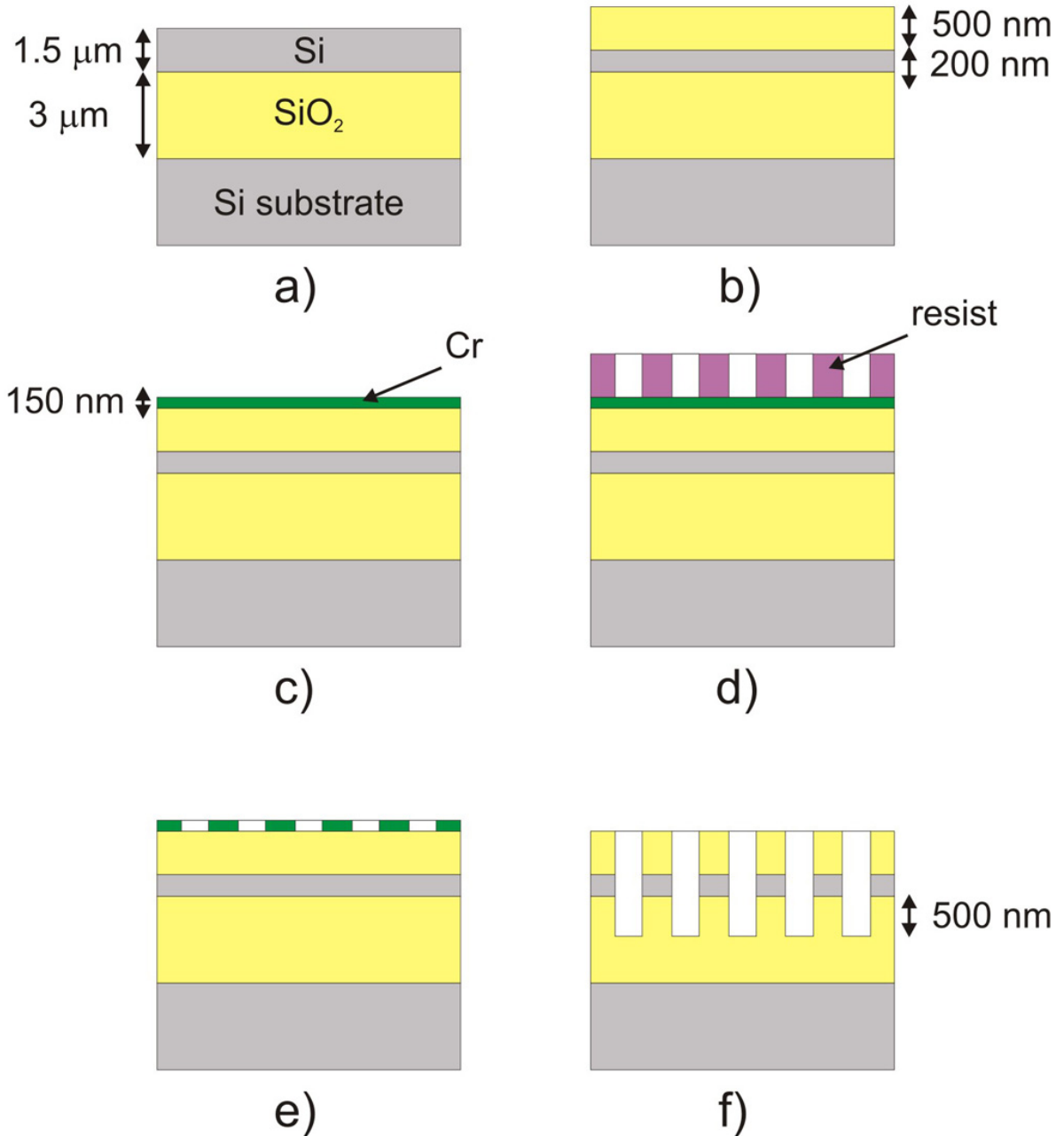
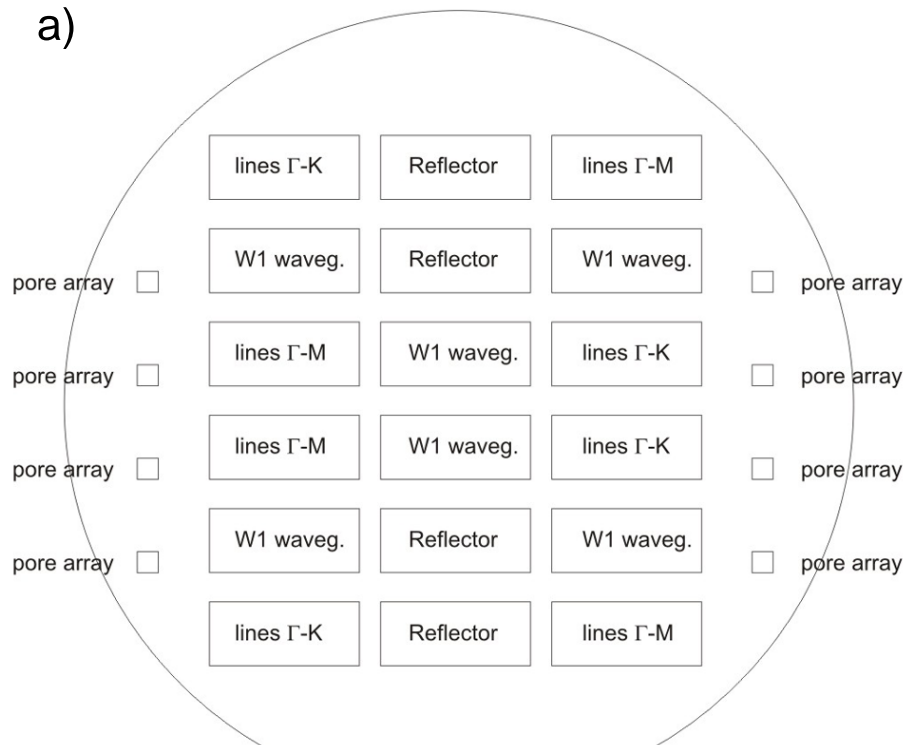


**Figure 4.2:** Full process designed to fabricate the IOSOI PPCs. a) Initial SOI wafer, b) formation of the silicon core and the upper oxide cladding via thermal oxidation steps followed by wet etching in HF, c) deposition of the Cr mask by sputtering, d) electron-beam lithography, e) patterning of the Cr mask and f) patterning of the IOSOI structure.

a)



b)

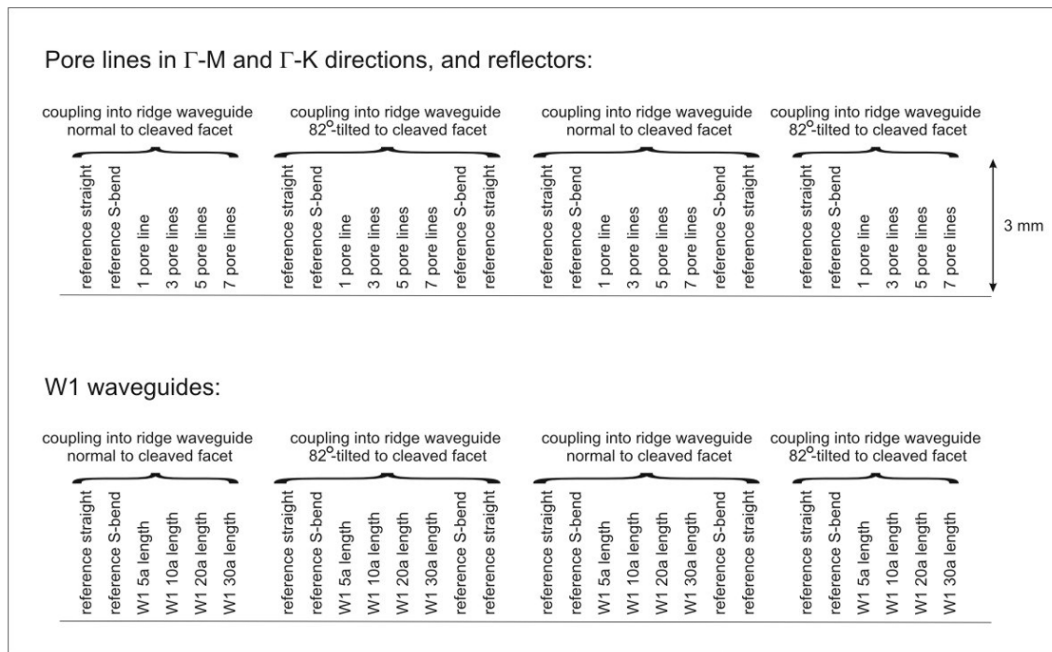


**Figure 4.3:** a) Layout of the large "mask" used for electron-beam lithography on whole 4" wafers. b) Arrangement of the waveguide series on this mask. Each series contains several waveguides, all with the same test structure of varying length or number of pore rows, as well as the reference ridge waveguides. Two ways of light in- and out-coupling from the external light source into the ridge waveguides are considered, either normal to the cleaved facet, or slightly tilted ( $8^\circ$ ). The length of the test structures is varied between 1, 3, 5 and 7 pore rows for the pore lines in the  $\Gamma$ -M and  $\Gamma$ -K directions, as well as for the reflector walls. In the case of the W1 waveguide, lengths of  $5a$ ,  $10a$ ,  $20a$  and  $30a$  are considered.

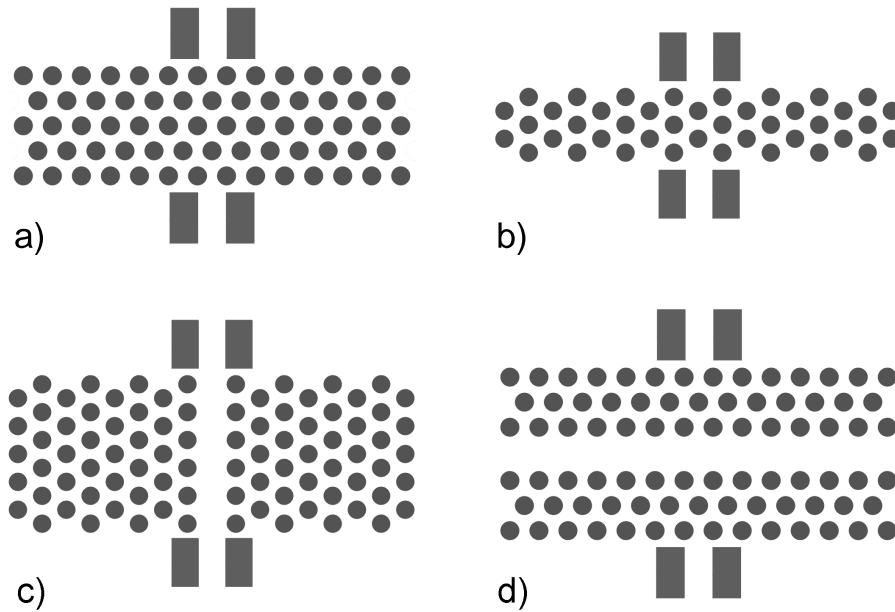


**Figure 4.4:** Test structure types on the test mask. a) Pore lines in the  $\Gamma$ -M direction, b) pore lines in the  $\Gamma$ -K direction, c) W1 waveguide, and d) W1 line defect in the reflector configuration.

#### 4.2.1 Design of the Masks

The designs for e-beam lithography have been written in the usual GDSII format using the ElphyFe software by Raith. In the following, we will refer to these designs as "masks". Among various masks programmed, the most important ones are the large mask for a whole 4" wafer containing several test structures and smaller masks with different long PC waveguides.

The general layout of the large test mask is presented in fig. 4.3a. It contains five different test structures. The two first ones, consisting of pore rows in the  $\Gamma$ -M and  $\Gamma$ -K directions with varying number of rows, are shown in fig. 4.4a and b, respectively. As presented in fig. 3.26 at the end of chapter 3, light is coupled in and out of the PC through integrated ridge waveguides. These structures will be used in transmission to measure the attenuation per pore row in both directions within the band gap. The third type of structure, shown in fig. 4.4c, is a short W1 waveguide. The length of the waveguide is varying in order to determine the transmission through the waveguide and the corresponding propagation losses. The fourth type of test structure, shown in fig. 4.4d, consists of a W1 line defect positioned perpendicularly to the input waveguide to build a reflector. Transmission measurements through this structure will allow to determine the quality factor of the W1 waveguide. Similar to cases a and b, the waveguide and reflector are sandwiched between two integrated ridge waveguides. The structures are arranged in series, each series containing several waveguides with the same type of test structure and varying number of pore rows. Each series contains also reference ridge waveguides of two different types, straight and S-bent. The standard layout of the series is presented in fig. 4.3b. The last test structure is a larger pore array. Unlike the others used in transmission from the side, this structure should be tested in reflection from the top, using the Astratov method [99]. Such approach allows to experimentally determine the position of the resonant modes of the bulk PPC.

The structures on the smaller masks are longer W1 waveguides, which will be used to study and to compare the dispersion properties of different designs. On one mask, shown in fig. 4.5,

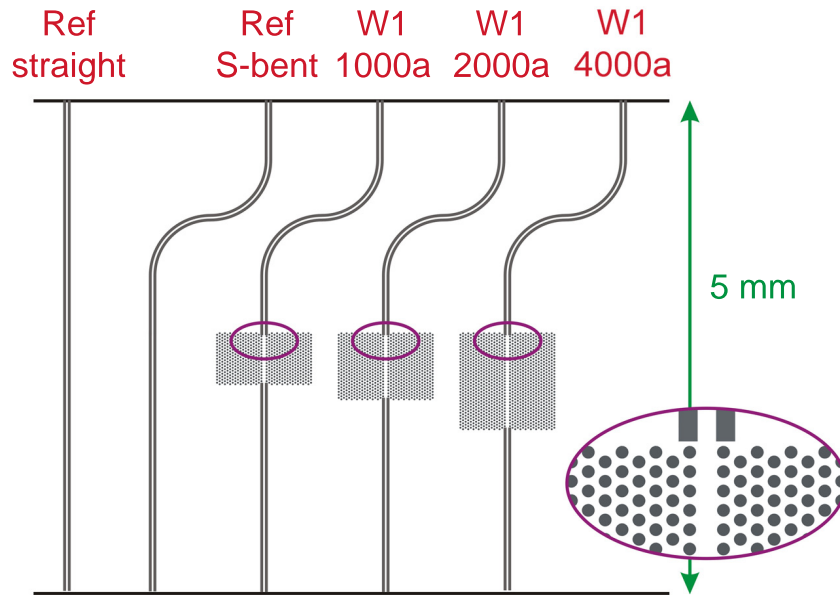


**Figure 4.5:** Layout of the small mask containing simple W1 waveguides of different lengths and reference ridge waveguides. The lengths of the W1 waveguides are  $1000 a$ ,  $2000 a$  and  $4000 a$ , respectively, for a total device length of 5 mm for all waveguides.

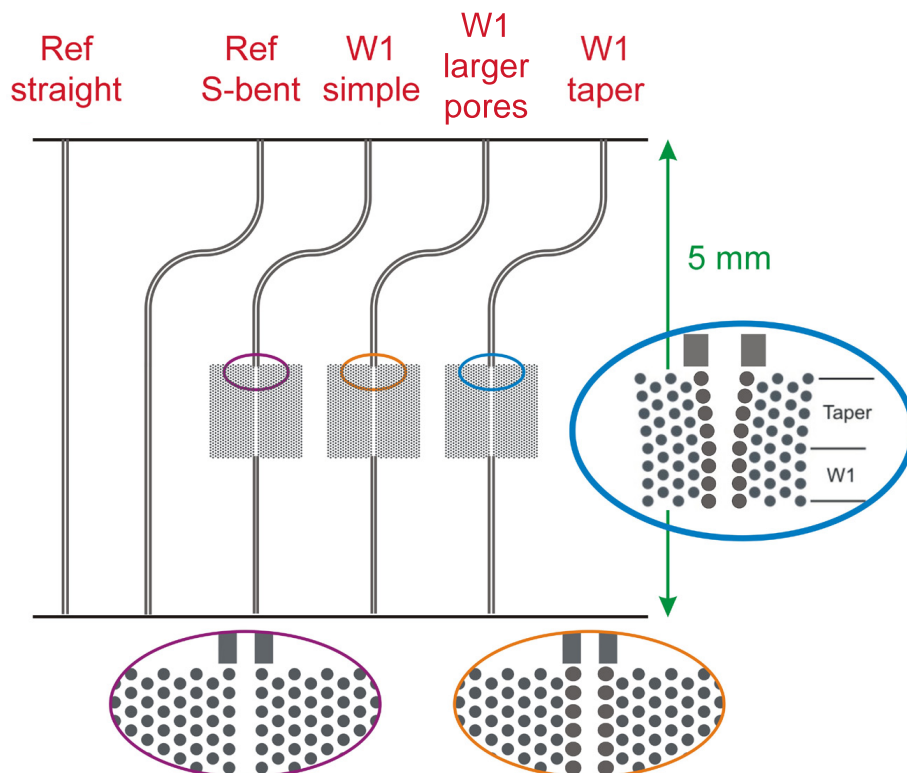


**Figure 4.6:** Layout of the small mask used for a comparison between simple W1 waveguides, W1 waveguides with 5% larger pores on both sides of the defect and W1 waveguides with 5% larger pores on both sides as well as the taper designed in chapter 3. All W1 waveguides are  $1000 a$  long, for a total device length of 5 mm for all waveguides. The wafer series include also reference ridge waveguides.

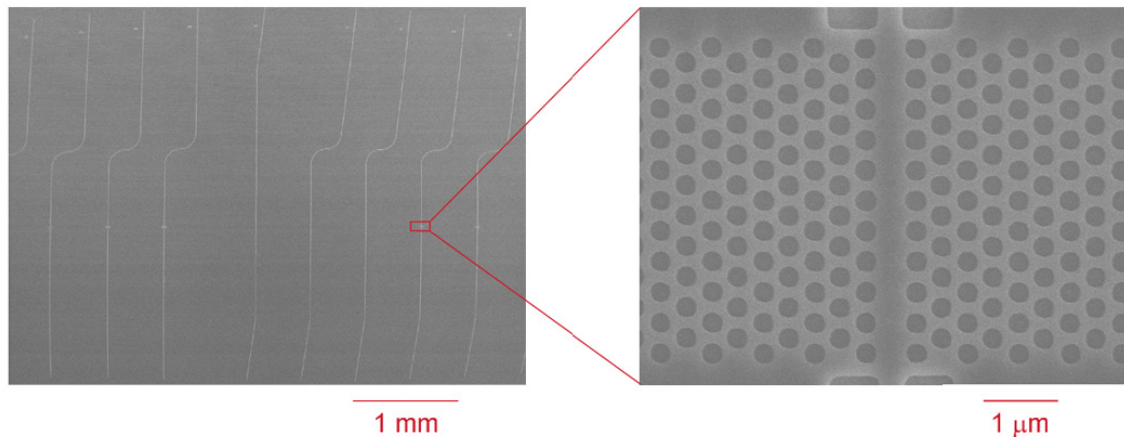


**Figure 4.7:** SEM pictures of the lithography on Shipley UV3 resist by Qudos (top views). The e-beam lithography was performed on a whole 4" wafer with the design presented in fig. 4.3 and 4.4. The left panel shows a part of a W1 waveguide series; going from the left to the right of this image, the three first devices have W1 waveguides of  $10a$ ,  $20a$ , and  $30a$  length, respectively, along with normal coupling into the ridge waveguides. In the other five devices, light is coupled into ridge waveguides which are  $8^\circ$  tilted to the normal. In the middle are two reference waveguides, one straight and one bent. The three last devices have W1 waveguides with  $5a$ ,  $10a$  and  $20a$  length, respectively. The right panel shows an enlargement of a W1 waveguide with a length of  $10a$ . The darker areas are the holes left in the resist after development. Inside the holes, the air pores will be etched into the Cr layer and then into the SOI structure to build the photonic crystal, whereas the larger lines will become the air trenches of the ridge waveguides.

W1 waveguides with lengths of  $1000a$ ,  $2000a$  and  $4000a$  are inserted between the usual ridge waveguides. On the other mask, shown in fig. 4.6, simple W1 waveguides with  $1000a$  length are compared to W1 waveguides of the same length with 5% larger pores on both sides, as well as to similar waveguides with larger pores and tapers, corresponding to the design presented in fig. 3.26 at the end of chapter 3.

## 4.2.2 Results of Resist Patterning

Once the masks are programmed, they are sent along with the samples for e-beam lithography, performed by Qudos Technology (England), and collaborators at the university of Würzburg.

The test patterns on the whole 4" wafers were written by Qudos into a 350 nm-thick Shipley UV3 resist layer. This kind of resist is quite resistant to dry etching processes. However, a resist layer thicker than 350 nm cannot be patterned easily for hole diameters around 300 nm. As will be discussed later in this chapter, this parameter strongly limits the rest of the fabrication process. Fig. 4.7 and 4.8 represent top views and cross sections, respectively, of scanning electron microscope (SEM) investigations of the lithography. In fig. 4.7, a part of a series with W1 waveguides and reference ridge waveguides is shown. From the zoom of a W1 waveguide (see the right panel in fig. 4.7), well defined patterns can be seen, revealing the quality of the lithography. The vertical resist walls shown in fig. 4.8 reconfirm this good quality.

The smaller masks with longer W1 waveguides have been first written in Würzburg into a PMMA layer. Compared to the Shipley UV3 resist, PMMA is easier to pattern, and a larger thickness up to 700 nm can be achieved. However, PMMA is removed easily in dry etching

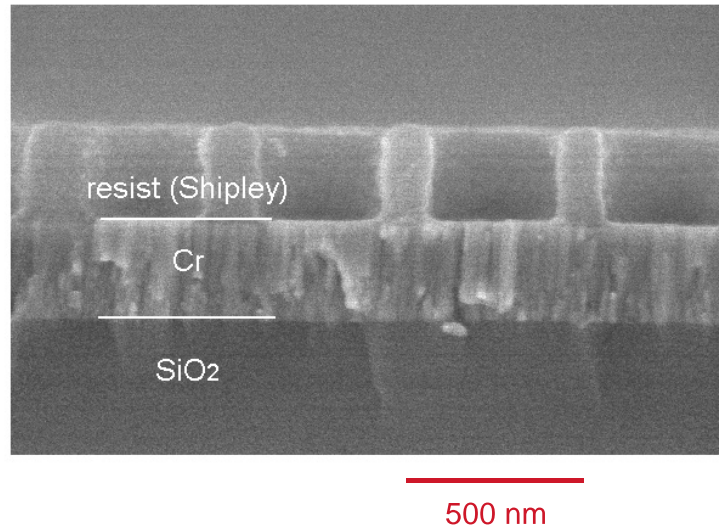


**Figure 4.8:** Cross-sectional SEM image of the patterned holes into the Shipley UV3 resist. The perfectly vertical resist walls attest of the good quality of the lithography.

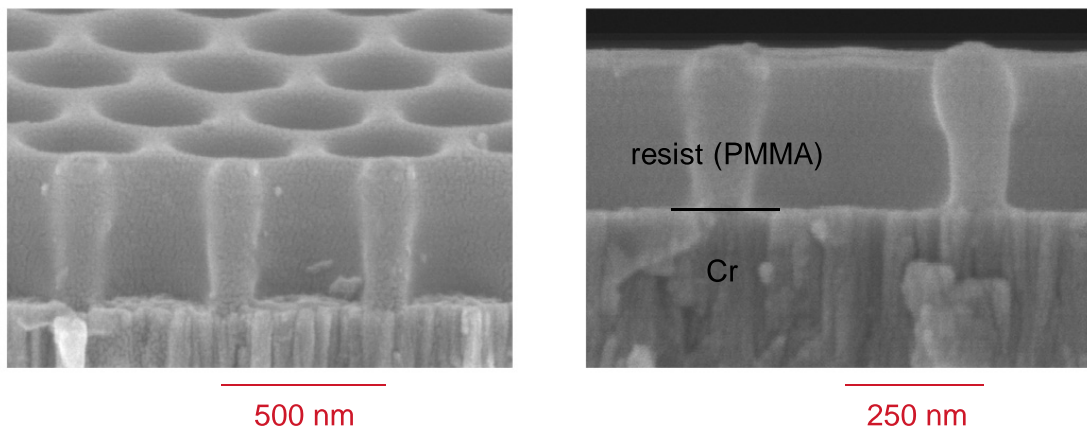


**Figure 4.9:** Results of the lithography in a 500 nm-thick PMMA layer (SEM images). The left panel shows a tilted cross section with an angle of  $15^\circ$  on the surface, and the right panel depicts an enlarged cross section.

processes, and more specifically, it is not convenient in the Cr patterning process, as will be presented in the next section. Therefore, the last batches of samples were patterned in Würzburg using a 400 nm-thick ZEP 520 resist layer. During dry etching processes, ZEP 520 shows a similar behavior as the Shipley UV3 resist. As in the case of Shipley UV3, the resistance to the plasma is high, but the thickness is limited to 400 nm. In both cases, the patterning into the resist thickness is as good as the lithography performed by Qudos. As an example, fig. 4.9 presents the results of e-beam lithography in a 500 nm-thick PMMA layer.

After the lithography, which is expensive and time consuming, the samples were sent back and the patterning of the underlying Cr mask was subsequently performed at the Max-Planck Institute, as shown in the following section.

Gas Composition	RF Power	DC bias	Chamber Pressure
Cl <sub>2</sub> : 60 sccm, O <sub>2</sub> : 3 sccm	50 W	25 V	90 mTorr

**Table 4.2:** Starting recipe used for the optimization of the Cr etching process.

## 4.3 Cr Etching

The etching of thick Cr layers at a submicron scale has not been performed in detail so far, partly due to the hardness of Cr, which makes the etching difficult. Furthermore, the following deep oxide etching process necessitates a large Cr thickness ( $\geq 150$  nm), which leads to aspect ratios of 0.5 for the 300 nm-large pores and 1 for the 150 nm-thick pore walls. Such aspect ratios are very high for a metal layer. Taking into account the small resist thickness limited by the e-beam lithography process, and the diversity of the resists used in this project, we had to find an optimal procedure, allowing to etch small features in Cr with aspect ratios around 0.5 and a selectivity better than 1:3 to any kind of resist. Furthermore, the etching of small samples requires the samples to be glued on a 4" substrate, e.g., a silicon dummy wafer. Since the glue used possess a low thermal conduction, the process to be designed should also be temperature independent.

### 4.3.1 Preliminary Result

The chemistry engaged in Cr plasma etching consists of three possible scenarios: etching in pure Cl<sub>2</sub> or Cl-containing gas, etching in Cl-based gas + O<sub>2</sub>, and etching in Cl-based gas + O<sub>2</sub> + Ar or other noble gas [100, 101, 102]. In fact, there is no other choice in the gas composition, because CrO<sub>2</sub>Cl<sub>2</sub> is the only volatile product of the Cr reaction in a gas plasma. In our work, we thus used a plasma composed of Cl<sub>2</sub> + O<sub>2</sub> for Cr etching. The etching was performed in an Oxford Plasmalab System 100 machine with the ICP180 source. Helium was applied to the wafer backside to improve thermal contact with the water-cooled electrode. The maximum gas flow for Cl<sub>2</sub> and O<sub>2</sub> was limited to 100 sccm<sup>1</sup> and 50 sccm, respectively. The etching was performed in the RIE mode [97], although some tests with the ICP source were also undertaken without success. Since a basic RIE process for Cr etching is known for larger feature sizes [103], it was used as a starting point for the optimization of the Cr etching process. The parameters of this process are summarized in table 4.2. All the optimization steps were performed using samples patterned with the Shipley UV3 resist. At the end of the optimization, the process was tested with the other types of resist.

The samples used for this test were patterned with 350 nm-thick Shipley UV3 resist. SEM pictures of the etched sample are shown in fig. 4.10. After 25 minutes, the entire resist layer was removed. However, the holes etched into the Cr were only 60 nm deep, corresponding to an etching rate of 2.4 nm/min. Therefore, this process was not convenient for the etching of small features with higher aspect ratios. A further optimization was necessary.

To optimize the etching recipe, the gas composition, RF power and pressure were varied step by step. Due to the limited resist thickness, the selectivity of the Cr etching to the resist is the most crucial parameter. The selectivity is defined by 1: $x$ , where  $x$  is the resist thickness necessary (in nm) to etch 1 nm of Cr. The smaller  $x$ , the better the selectivity. In the following study, we will consider the variations of the etch rate with the different process parameters, as well as the variations of the selectivity.

<sup>1</sup>sccm = standard cubic centimeter per minute

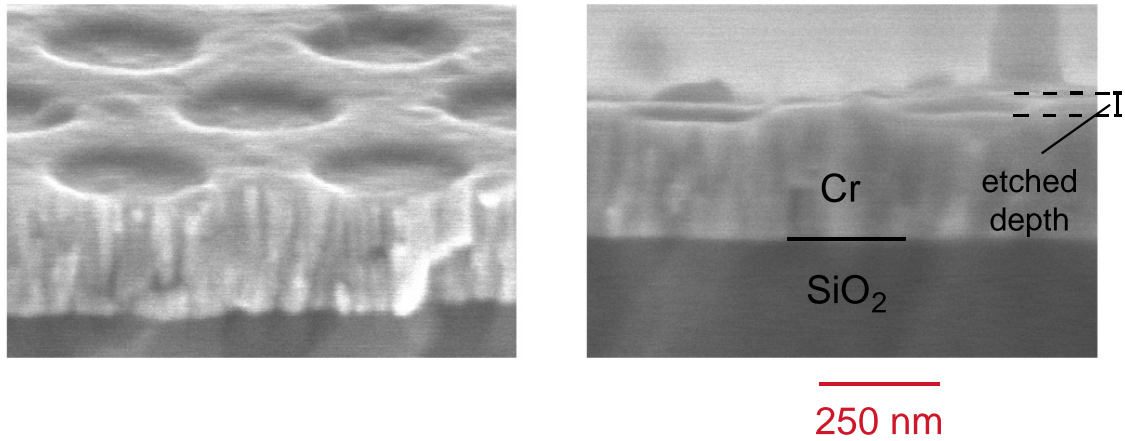


**Figure 4.10:** Cross sectional SEM images of the sample after Cr etching with the recipe optimized for larger feature sizes (given in table 4.2). The left picture was obtained by tilting the sample  $15^\circ$  towards the surface.

### 4.3.2 Optimization of the Gas Composition

Since the resist can be removed by an  $O_2$  plasma, the  $O_2$  concentration appears to be the most important parameter for the selectivity. Therefore, after some preliminary trials we fixed the values of RF power and pressure at 40 W and 98 mTorr, respectively, while varied the oxygen concentration at a constant  $Cl_2$  flow of 100 sccm to determine the gas composition yielding the best selectivity. The results are presented in fig. 4.11. The best selectivity was obtained between 20 and 30 sccm of  $O_2$  flow, corresponding to a concentration between 15 and 23 % in the gas mixture, respectively. This gas composition also yields the best etching rate,  $\sim 6.5$  nm/min. We should note that these results depend on the quality of the Cr layer. Two different batches of samples, prepared with different sputtering times or apparatus, have slightly different etching rates and selectivities, and the optimum  $O_2$  flow is shifted between 20 and 30 sccm. Therefore, prior to etching a new batch of samples, it is necessary to perform some tests to determine the best gas composition for this specific Cr quality.

### 4.3.3 Optimization of the RF Power

The next parameter playing an important role is the RF power. The higher the RF power, the higher the DC bias inside the chamber and the higher the energy of the etching species. Since the etching rate strongly depends on the energy of the etching species, it should vary strongly with the RF power. In contrast, the selectivity may be only slightly affected, because both the resist and the Cr behave similarly with different RF powers. Using a batch of samples having their optimum  $O_2$  flow at 30 sccm, a new series of etch tests was performed by varying the RF power. The pressure of the process was again 98 mTorr. Fig. 4.12 shows the dependence of the etching rate and selectivity on the RF power. The values of the corresponding DC bias are also indicated. Note that in the RIE process only the RF power, not the DC bias, can be chosen [97]. As in the case of the  $O_2$  flow dependence, the etching rate increases in the small RF power regime, reaching a maximum at  $\sim 45$  W and then decreasing again for a larger RF power. As predicted, the selectivity is not as sensitive to the RF power as the etching rate if the RF power is not too high, say below  $\sim 40$  W, but it increases significantly with higher RF powers. Although the best etching rate was obtained at  $\sim 45$  W, we chose to work at the RF power of  $\sim 40$  W,

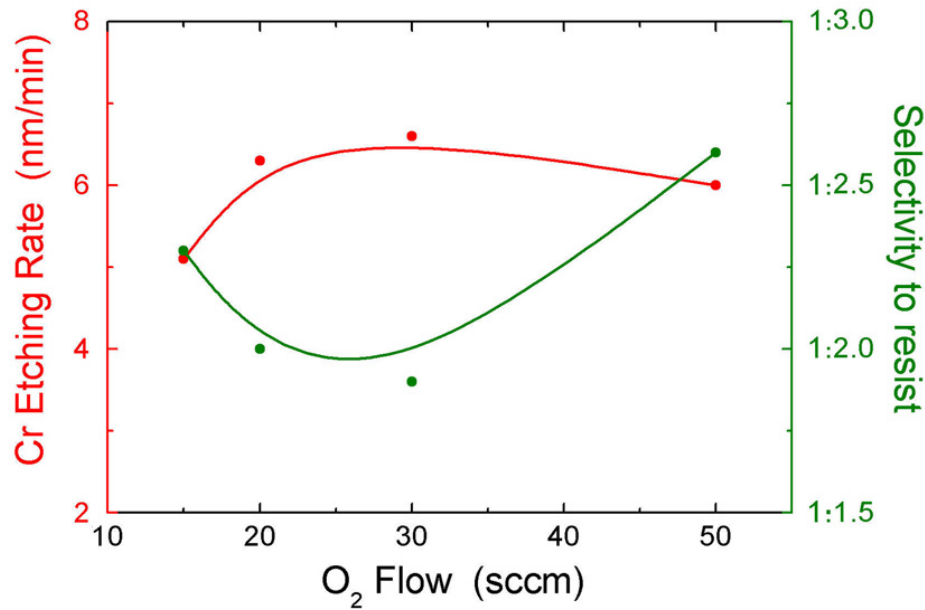


**Figure 4.11:** Dependences of the Cr etching rate (red curve) and selectivity to resist (green curve) on the O<sub>2</sub> flow. The etching process was performed at a pressure of 98 mTorr with a RF power of 40 W, leading to a DC bias of 22 V. The Cl<sub>2</sub> flow is 100 sccm.

considering the better selectivity. At 40 W, we are able to etch deeper with the same initial resist thickness, even if the process is slower.

#### 4.3.4 Further Optimization of the Process

Apart from the most important parameters, the gas composition and RF power, the pressure and temperature also play a crucial role in the Cr etching process.

In the RIE process used in this project for the Cr etching, the choice of the process pressure is very limited, since pressures  $\geq 100$  mTorr are not possible in the equipment to maintain a stable plasma during the process. By exploiting the pressure between 80 and 98 mTorr, we concluded that the higher the pressure, the better the etching rate and the selectivity. Therefore, we chose 98 mTorr as our working pressure.

The temperature dependence of the process is a crucial issue not yet addressed in this section. The different masks used all have different sizes, and sometimes we have to etch a whole 4" wafer, while sometimes only a small piece of only some square cm. Since only 4" wafers can be etched in the equipment, these small pieces must be glued on a 4" substrate, in this case a dummy silicon wafer. However, the sample cooling during the process is performed on the backside. Due to the low thermal conductivity of the glue, the temperature of the small wafer piece may be much higher than that of the whole 4" wafer. Furthermore, the different resists used have different behaviors as a function of the temperature. In particular, PMMA melts easier than ZEP 520 or Shipley UV3. Therefore, for a good reproducibility of the results, regardless of the sample size and the resist used, the process has to be temperature-insensitive as much as possible.

To succeed in this temperature independence, we cut the process in several sub-steps and introduced some pumping in between. Each etching sub-step lasted 2 minutes, and each pumping 50

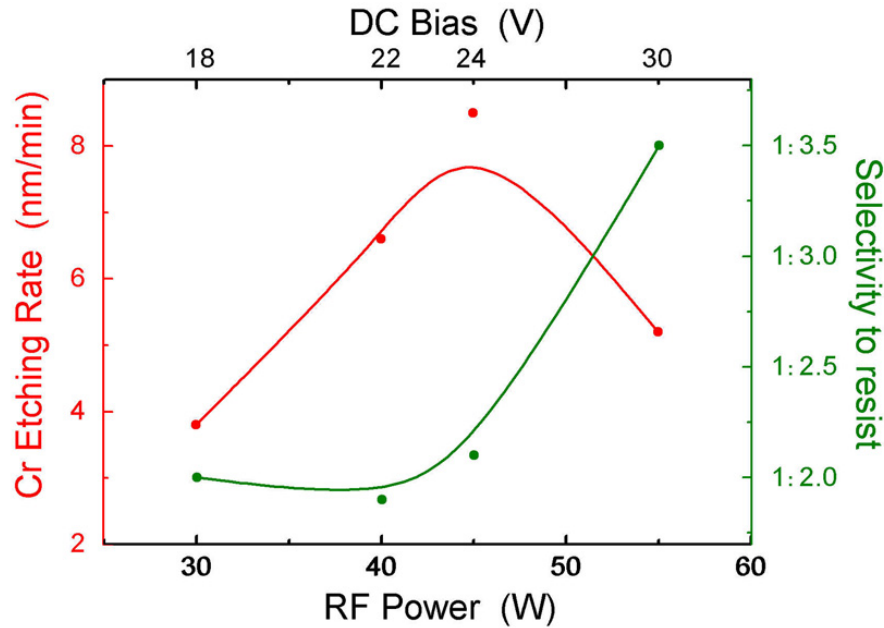


**Figure 4.12:** Dependences of the Cr etching rate (red curve) and selectivity to resist (green curve) on the RF power. The process was performed at a pressure of 98 mTorr. The  $\text{Cl}_2$  and  $\text{O}_2$  flows are 100 sccm and 30 sccm, respectively.

Gas Composition	RF Power	DC bias	Chamber Pressure	Time Steps
$\text{Cl}_2$ : 100 sccm $\text{O}_2$ : 20-30 sccm	40 W	22 V	98 mTorr	each step: 2' etching + 50'' pumping

**Table 4.3:** Optimized recipe used for the Cr etching process.

seconds. During the pumping, there was no plasma, but the low pressure and the backside cooling were maintained to qualitatively yield a relaxation of the system. The temperature of the sample surface (in particular, the resist), which increased during the etching due to the ion bombardment from the plasma, decreased during the pumping. As a result, the Shipley resist held longer before being removed, and the selectivity was increased by a factor of  $\sim 1.2$ . With other types of resists, it was also found that the introduction of the pumping improves the results. The most evident improvement was obtained with PMMA, where the selectivity was improved by a factor of 2.

To summarize, we have found an etching recipe, yielding a satisfactory etching rate, the best selectivity, and a temperature and sample size independence [104]. Table 4.3 summarizes the optimized parameters, and table 4.4 shows the results for the three different kinds of resists. SEM pictures of the samples after Cr etching using the optimized recipe are shown in fig. 4.13,

Resist	Etching Rate	Selectivity Cr:Resist
PMMA	3.7	1:6
Shipley UV3	6.6	1:1.9
ZEP 520	7.5	1:1.9

**Table 4.4:** Results of the Cr etching using the optimized recipe and the three types of resists.

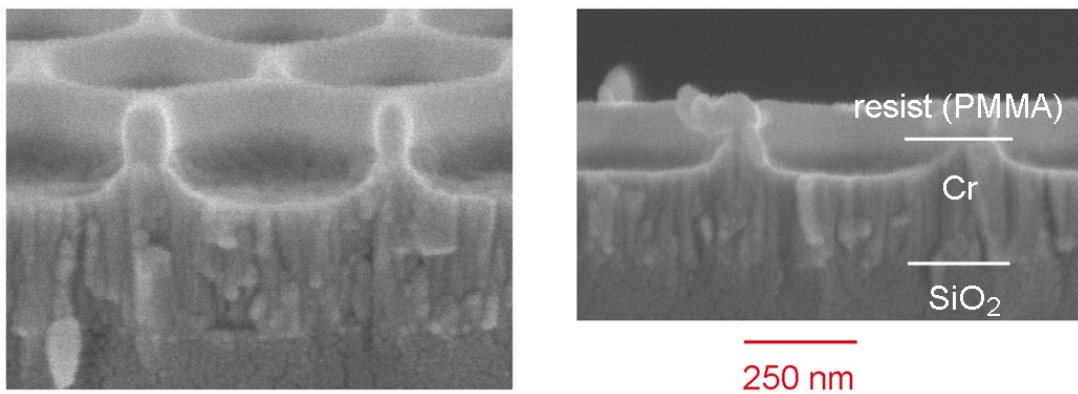


**Figure 4.13:** Cross sectional SEM images of the sample after Cr etching using the optimized recipe and a 700 nm-thick PMMA mask. The total thickness of the Cr layer was 400 nm. The left picture was obtained by tilting the sample 15° towards the surface.

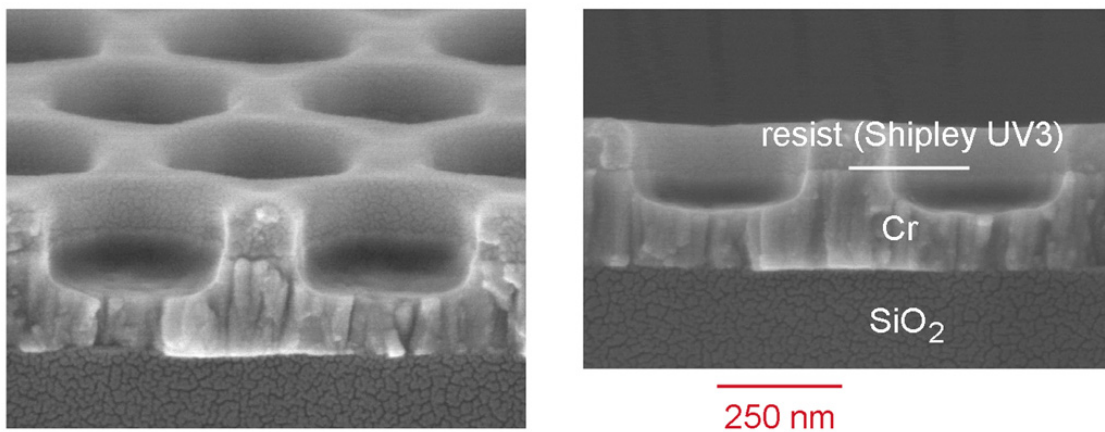


**Figure 4.14:** Cross sectional SEM images of the sample after Cr etching using the optimized recipe and a 350 nm-thick Shipley UV3 mask. The total thickness of the Cr layer was 400 nm. The left picture was obtained by tilting the sample 15° towards the surface.

4.14, and 4.15, in the case of a PMMA, Shipley UV3 and ZEP 520 mask, respectively. As indicated in table 4.4, the etching rate still depends on the type of resist used. This phenomenon may arise from an additional chemical reaction between the resist and the plasma. Further future investigations are necessary, to prove this hypothesis. From table 4.4, it can be also concluded that PMMA is not convenient to serve as a mask for Cr etching, due to the low etching rate and the poor selectivity, although the PMMA layer can be thicker than the ZEP or Shipley resists. Therefore, the Cr etching process had to be performed using samples patterned with the Shipley UV3 or ZEP 520 resists.

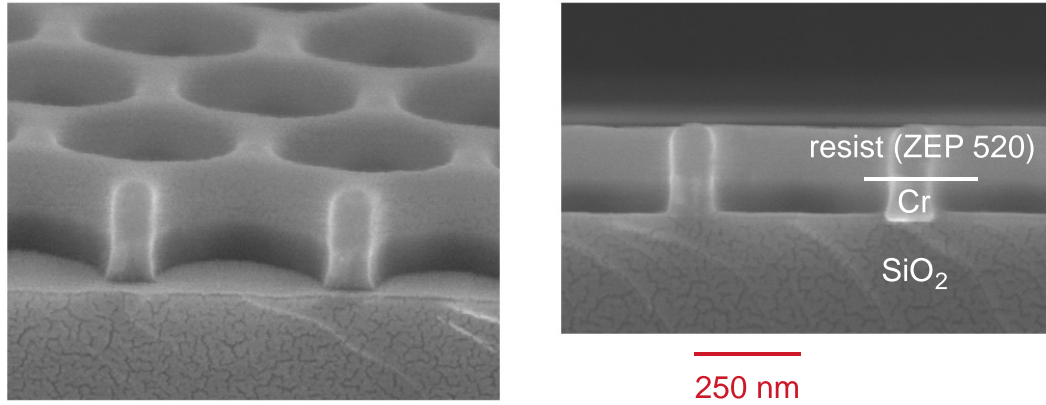


**Figure 4.15:** Cross sectional SEM images of the sample after Cr etching using the optimized recipe and a 400 nm-thick ZEP 520 mask. The total thickness of the Cr layer was 140 nm. In this case, the resist layer was thick enough to etch through the whole Cr layer. The left picture by obtained via tilting the sample  $15^\circ$  towards the surface.

## 4.4 Silicon and Silicon Dioxide Etching

Similar to Cr etching, silicon-dioxide etching at a submicron scale with high aspect ratios is a challenging process, although the etching of thin  $\text{SiO}_2$  layers with low aspect ratios is a standard process of the silicon technology [105]. This is due to two main issues that become stronger with increasing aspect ratio. First, since  $\text{SiO}_2$  is an insulator, the pore walls bombarded by the incident particles become charged during the process [105]. Secondly, the etch products react with the plasma particles to form a polymer that redeposits on the pore walls [106]. Both issues are well-known and have been widely studied. However, no satisfying general solution has been proposed so far. Since the fabrication of the IOSOI-based PPCs requires deep oxide etching, we should design an etching process which overcomes these two problems. Furthermore, the etching process should allow smooth transitions between the three layers  $\text{SiO}_2/\text{Si}/\text{SiO}_2$ , without underetching at the interfaces, to achieve perfectly vertical walls in the thin silicon core.

The etching is performed in an Oxford Plasmalab System 100 machine with the ICP380 source, equipped with fluorine-based gases. Unlike the case of Cr etching, no systematic study has been performed for the  $\text{SiO}_2/\text{Si}/\text{SiO}_2$  etching. This is due to the wide choice in chemistry involved in the etching process, leading to a large number of parameters that have to be optimized. Furthermore, several issues have to be addressed simultaneously, such as the etching of two different materials with completely different properties, Si and  $\text{SiO}_2$ , and the transitions between these two materials. Therefore, the method used was first to vary the parameters arbitrarily, to understand their influence on the etching results and to determine basic recipes. Among the several processes tested, one RIE process and two basic ICP processes were selected. These processes were then optimized further. This study is presented in more details in the following sections.

### 4.4.1 Results for RIE Etching

Initially, we intended to etch the three-layer structure  $\text{SiO}_2/\text{Si}/\text{SiO}_2$  in one step. Therefore, all the recipes under study - RIE as well as ICP - should allow to etch  $\text{SiO}_2$  as well as Si. In order to

test both the deep oxide etching and the transition  $\text{SiO}_2/\text{Si}$  with limited costs, all the etching tests were first performed on oxidized dummy silicon wafers with  $1.5 \mu\text{m}$   $\text{SiO}_2$  on the top. The SOI wafers were used after optimization of the process. The parameters of the optimized recipe for RIE etching are summarized in table 4.5, and SEM pictures of the etched samples are presented in fig. 4.16. This process shows the advantage to well preserve the Cr mask. Furthermore, the pore profiles presented in fig. 4.16 are vertical and only small polymer redeposition can be observed. However, if the pore depth is deeper than 500-600 nm, the profile becomes very bad and the pores tend to close, as shown in fig. 4.17. This "carrot" profile is found in most RIE processes that have been studied in this work and is also observed very often when etching III-V compounds in the RIE mode. Therefore, the RIE process is restricted to low aspect ratios up to 1.5.

Gas Composition	RF Power	DC bias	Chamber Pressure	Time
$\text{CHF}_3$ : 30 sccm $\text{SF}_6$ : 50 sccm $\text{O}_2$ : 20 sccm	RF: 75 W	260 V	20 mTorr	10'

**Table 4.5:** Recipe of the optimized RIE process for  $\text{SiO}_2/\text{Si}$  etching.

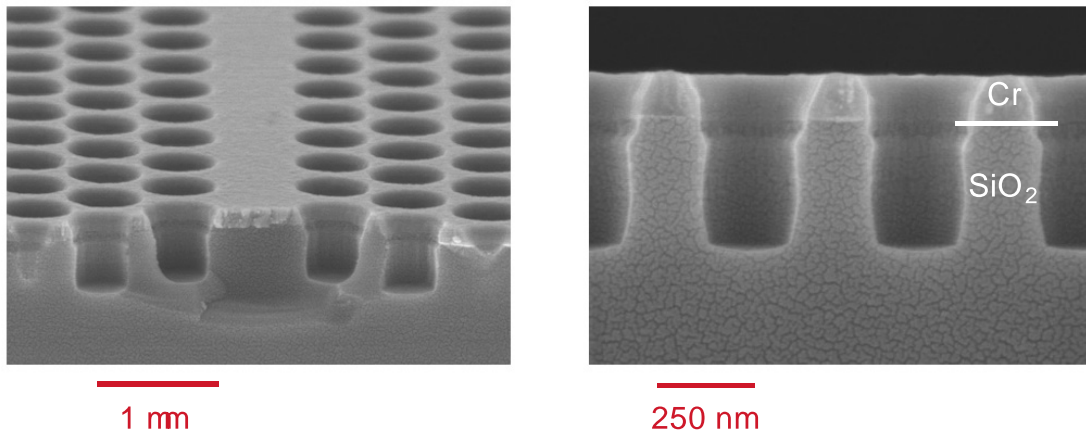


**Figure 4.16:** Cross sectional SEM images of  $\text{SiO}_2$  etching with the RIE recipe presented in table 4.5. The left picture was obtained by tilting the sample  $15^\circ$  towards the surface, and a W1 waveguide can be recognized in its center.

#### 4.4.2 Results for ICP Etching

In parallel to the RIE mode, the ICP etching was studied. Two basic recipes were selected, based on the  $\text{CHF}_3/\text{SF}_6$  and  $\text{C}_4\text{F}_8/\text{Ar}$  chemistry, respectively. For a better understanding of the different mechanisms that occur during etching, we will discuss the optimization of the first type of recipe in more details. The basic parameters for this recipe are summarized in table 4.6. SEM pictures of the samples after etching are presented in fig. 4.18.

Using the recipe presented in table 4.6, 900 nm oxide layers were etched, corresponding to an etching rate of 75 nm/min. As can be noticed in fig. 4.18, this recipe is not very aggressive

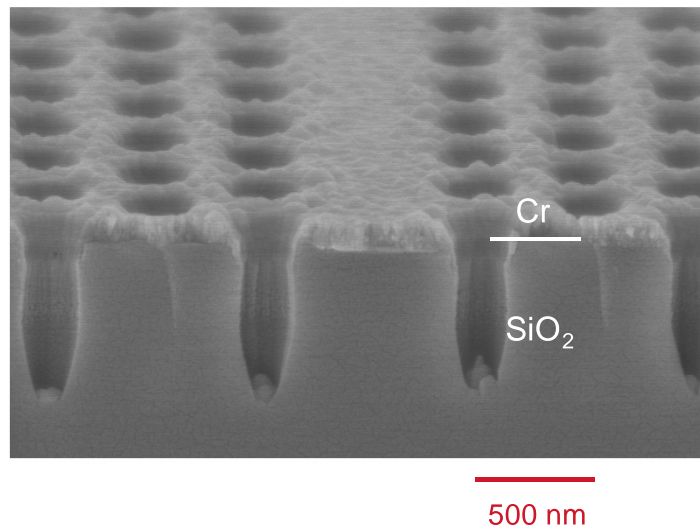


**Figure 4.17:** Cross sectional SEM image of  $\text{SiO}_2$  etching with the RIE recipe presented in table 4.5 and a longer etching time. The picture was obtained by tilting the sample  $15^\circ$  towards the surface, and a W1 waveguide can be recognized in its center.

Gas Composition	RF and ICP Power	DC bias	Chamber Pressure	Time
$\text{CHF}_3$ : 10 sccm $\text{SF}_6$ : 5 sccm	RF: 50 W ICP: 1500 W	130 V	0.8 mTorr	12'

**Table 4.6:** First ICP etching basic recipe used for  $\text{SiO}_2/\text{Si}$  etching.

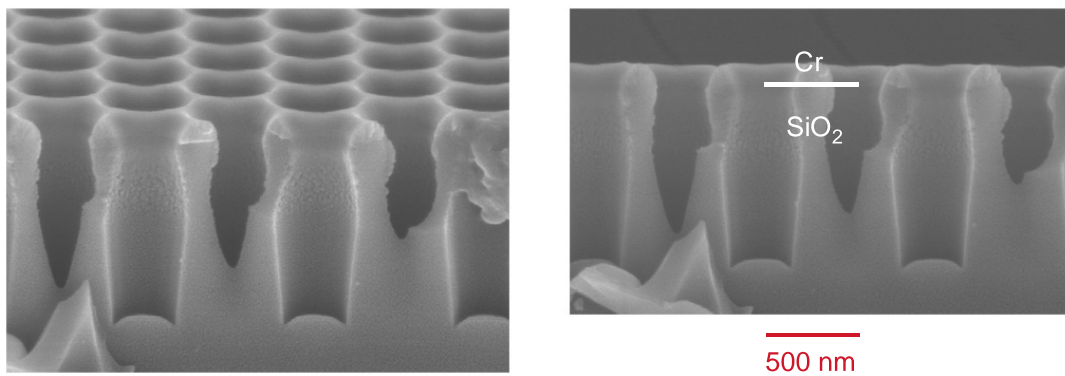


**Figure 4.18:** Cross sectional SEM images of  $\text{SiO}_2$  etching with the ICP recipe presented in table 4.6. The left picture was obtained by tilting the sample  $15^\circ$  towards the surface.

Gas Composition	RF and ICP Power	DC bias	Chamber Pressure	Time
CHF <sub>3</sub> : 10 sccm SF <sub>6</sub> : 10 sccm	RF: 80 W ICP: 1500 W	200 V	0.6 mTorr	10'

**Table 4.7:** Second ICP etching basic recipe used for SiO<sub>2</sub>/Si etching, with increased RF power and SF<sub>6</sub> concentration.

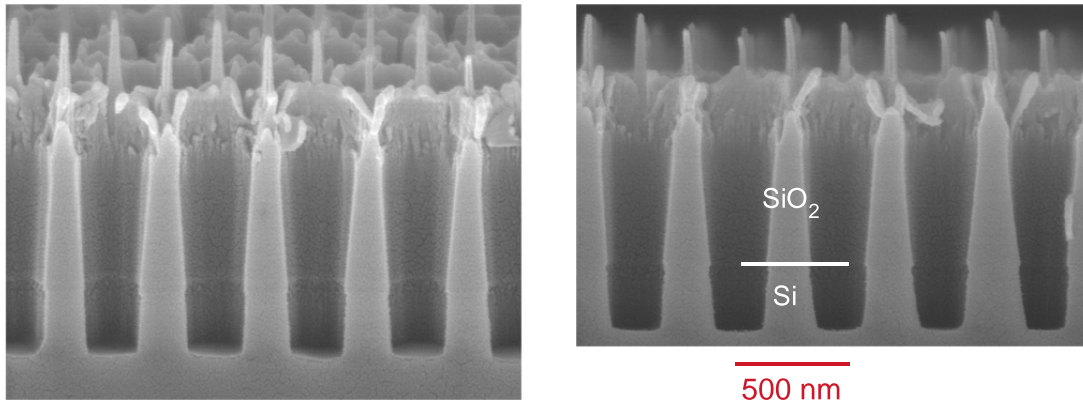


**Figure 4.19:** Cross sectional SEM images of SiO<sub>2</sub>/Si etching with the ICP recipe presented in table 4.7. The left picture was obtained by tilting the sample 15° towards the surface.

against the Cr mask, since only 20-30 nm have been removed. However, the "bottle-shape" of the oxide walls is typical for a charging of the walls during the etch process. Since SiO<sub>2</sub> is an insulator, it can be strongly charged by the plasma particles reaching the pore walls. As a consequence of the wall charging, the plasma particles are deflected, leading to this particular profile. One of the ways to avoid this problem is to increase the energy of the particles to enhance the anisotropy and reduce the amount of particles reaching the pore walls instead of the pore bottom. This is achieved by enhancing the bias, i.e., by enhancing the RF power, or by decreasing the pressure. Furthermore, the roughness on the top part of the walls, that can be observed in fig. 4.18, is due to some polymer formation and redeposition. This phenomenon is typical for SiO<sub>2</sub> etching with carbon-based gases. A way to lower this effect is to reduce the carbon concentration in the plasma. Therefore, in the following recipe, the SF<sub>6</sub> flow was enhanced. The parameters of this recipe with increased RF power and increased SF<sub>6</sub> flow are presented in table 4.7, and SEM pictures of the sample after etching are shown in fig. 4.19.

As can be noticed in fig. 4.19, the etching rate is strongly enhanced due to the higher bias, and the underlying silicon layer was reached. It can be clearly recognized that this recipe allows to etch SiO<sub>2</sub> as well as Si. However, the Cr mask was almost completely sputtered away during the etching process. As a result, the upper part of the oxide walls was partly removed, and the remaining walls are not perfectly vertical. Therefore, a very high bias is not a good solution to avoid the "bottle" profile of the walls arising from the particle deflection. In a further optimization of the ICP process, the parameters should be chosen in such a way that the Cr mask holds during the etching process. A possible solution is to vary the bias during the process. In this way, the trajectory of the charged particles can be modified continuously to avoid a "bottle" profile, with an average bias low enough to protect the Cr mask. The parameters of the recipe with varying RF power are presented in table 4.8, and SEM pictures of the sample

Gas Composition	ICP Power	RF Power	DC bias	Chamber Pressure	Time
CHF <sub>3</sub> : 10 sccm SF <sub>6</sub> : 10 sccm	1500 W	50 W	135 V	1.5 mTorr	10''
		60 W	170 V		10''
		70 W	190 V		10''
		80 W	210 V		10''
cycle repeated 15 times					

**Table 4.8:** ICP etching recipe used for SiO<sub>2</sub>/Si etching, with varying RF power.

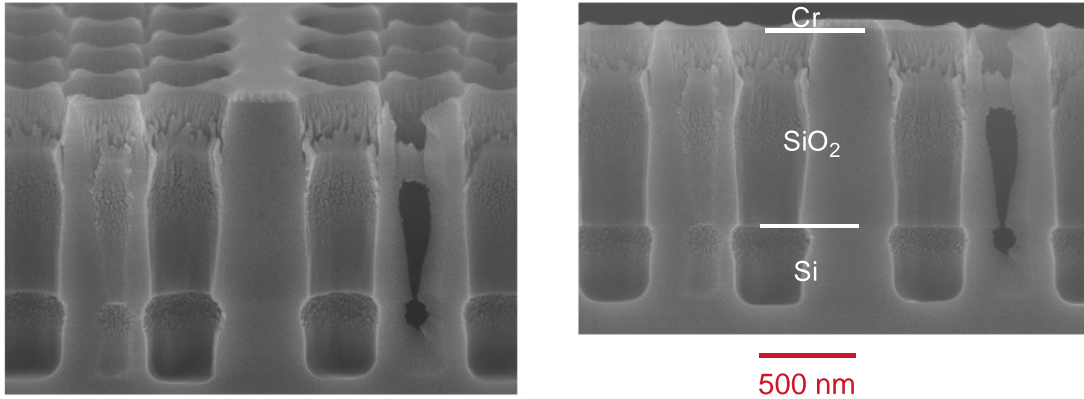


**Figure 4.20:** Cross sectional SEM images of SiO<sub>2</sub>/Si etching with the ICP recipe presented in table 4.8. The left picture was obtained by tilting the sample 15° towards the surface. In the center of the pictures, a W1 waveguide can be recognized.

after etching are shown in fig. 4.20.

Comparing with fig. 4.18, the profile of the oxide walls in fig. 4.20 is much better. However, as could also be observed in fig. 4.19, the two last recipes lead to a strong polymer redeposition on the upper part of the oxide walls. Furthermore, large underetching of the silicon at the interface SiO<sub>2</sub>/Si occurred with the recipe presented in table 4.8. Due to the strong bias of the recipe given in table 4.7, the transition between the SiO<sub>2</sub> and the Si layers was much smoother. A way to reduce the underetching observed in fig. 4.20, without increasing the bias, is to add some oxygen in the plasma. Indeed, oxygen is often used in deep silicon etching, to passivate the silicon walls during the etching process and to protect them. Since O<sub>2</sub> plasmas are also used to etch polymers, we hope that adding O<sub>2</sub> in the plasma will simultaneously reduce the polymer redeposition. The parameters of the new recipe, with additional O<sub>2</sub> in the plasma and an average RF power of 65 W, are presented in table 4.9. The corresponding SEM pictures of the sample after etching are shown in fig. 4.21.

Gas Composition	RF and ICP Power	DC bias	Chamber Pressure	Time
CHF <sub>3</sub> : 5 sccm SF <sub>6</sub> : 5 sccm O <sub>2</sub> : 5 sccm	RF: 65 W ICP: 1500 W	180 V	0.8 mTorr	12'

**Table 4.9:** Recipe of the ICP etching process for SiO<sub>2</sub>/Si etching, with O<sub>2</sub> in the gas mixture.

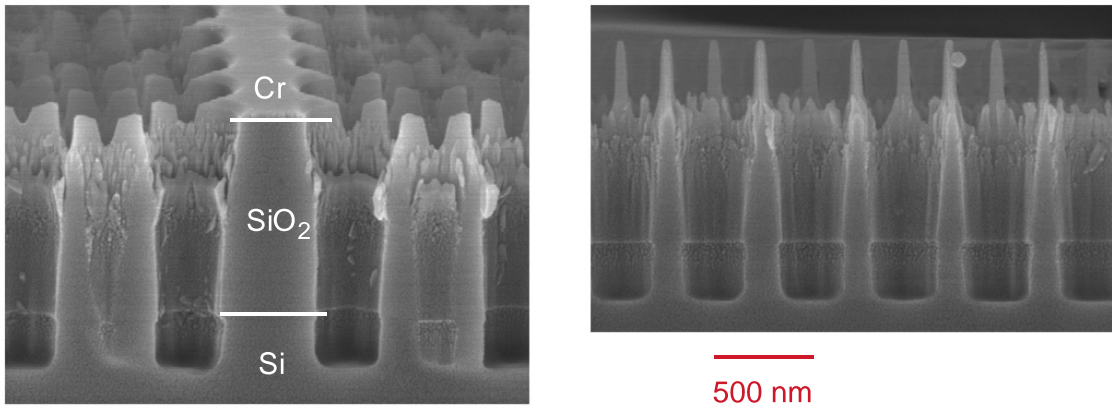


**Figure 4.21:** Cross sectional SEM images of SiO<sub>2</sub>/Si etching with the ICP recipe presented in table 4.9. The left picture was obtained by tilting the sample 15° towards the surface, and a W1 waveguide can be recognized in its center.

Although the underetching is reduced with additional O<sub>2</sub> in the plasma, the polymer redeposition is still as strong as was observed in fig. 4.19 and fig. 4.20. Replacing CHF<sub>3</sub> by C<sub>4</sub>F<sub>8</sub> in the above processes, very smooth transitions without any underetching at the SiO<sub>2</sub>/Si interfaces were achieved. However, the polymer redeposition was not reduced. Another solution to this problem is to reduce again the carbon concentration in the plasma. The corresponding recipe is given in table 4.10. From the results presented in fig. 4.22, it can be deduced that this solution strongly limits the polymer formation. However, the shape of the pores is tilted. This is partly due to the removing of the Cr mask, partly to the modification of the process chemistry.

To summarize, the optimized recipe based on the CHF<sub>3</sub>/SF<sub>6</sub> chemistry should yield simultaneously:

- Perfectly vertical walls. It implies a preserved Cr mask, as well as no "bottle" profile. This is achieved by working with an average low bias, and by varying it (i.e., varying the RF power) during the process to modify continuously the trajectory of the deflected particles.
- No underetching of the silicon at the interface SiO<sub>2</sub>/Si. A way to reduce this underetching is to apply very high bias when etching through the interface between the two materials. The other way is to modify the gas composition, by replacing CHF<sub>3</sub> by C<sub>4</sub>F<sub>8</sub>. The addition of O<sub>2</sub> in the plasma, to passivate the silicon walls during the etching process, can also help.
- A limited polymer formation and redeposition on the pore walls. This issue is the most difficult one. Although the presence of the polymer on the upper part of the oxide walls may not have any significant influence on the device functionality, it may strongly affect the properties of the PPC if it is deposited in the surrounding of the Si core. A possible solution to limit the polymer formation is to lower the carbon concentration in the plasma. However, a good compromise between low redeposition requiring low carbon concentration, and vertical walls requiring high carbon concentration, still remains to be found.

Although the further optimization of this ICP process may be possible in order to find a recipe fulfilling all requirements cited above, we prefer to study a second type of process based on

Gas Composition	ICP Power	RF Power	DC bias	Chamber Pressure	Time
CHF <sub>3</sub> : 3 sccm	1500 W	50 W	135 V	0.8 mTorr	10''
SF <sub>6</sub> : 6 sccm		60 W	170 V		10''
O <sub>2</sub> : 6 sccm		70 W	190 V		10''
		80 W	210 V		10''
cycle repeated 20 times					

**Table 4.10:** ICP etching recipe used for SiO<sub>2</sub>/Si etching, with varying RF power and a lower CHF<sub>3</sub> concentration.

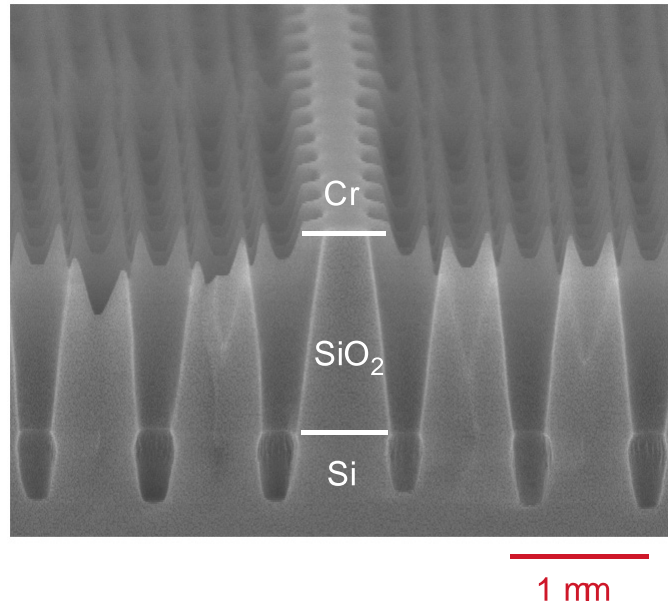


**Figure 4.22:** Cross sectional SEM image of SiO<sub>2</sub>/Si etching with the ICP recipe presented in table 4.10. The picture was obtained by tilting the sample 15° towards the surface, and a W1 waveguide can be recognized in its center.

the C<sub>4</sub>F<sub>8</sub>/Ar chemistry. The basic recipe for this second ICP process is given in table 4.11. In the case of C<sub>4</sub>F<sub>8</sub> highly diluted in a noble gas like Ar, the plasma chemistry is completely different from the previous case. In particular, the polymer redeposition is very homogeneous and passivates the pore walls in a convenient way, leading to a high anisotropy and a good protection of the walls from underetching at the interfaces. As a result, the pore walls are smooth and highly vertical, and the transitions at the interfaces between the silicon and the oxide are not visible. Furthermore, during this process the Cr mask is well preserved, allowing deep anisotropic etching. The same recipe applied to SOI wafers led to similar results, as confirmed in fig. 4.23.

Gas Composition	ICP Power	RF Power	DC bias	Chamber Pressure	Time
C <sub>4</sub> F <sub>8</sub> : 10 sccm Ar : 90 sccm	1500 W	25 W	100 V	15 mTorr	10'

**Table 4.11:** Second type of ICP etching recipe used for SiO<sub>2</sub>/Si etching, based on the C<sub>4</sub>F<sub>8</sub>/Ar chemistry.

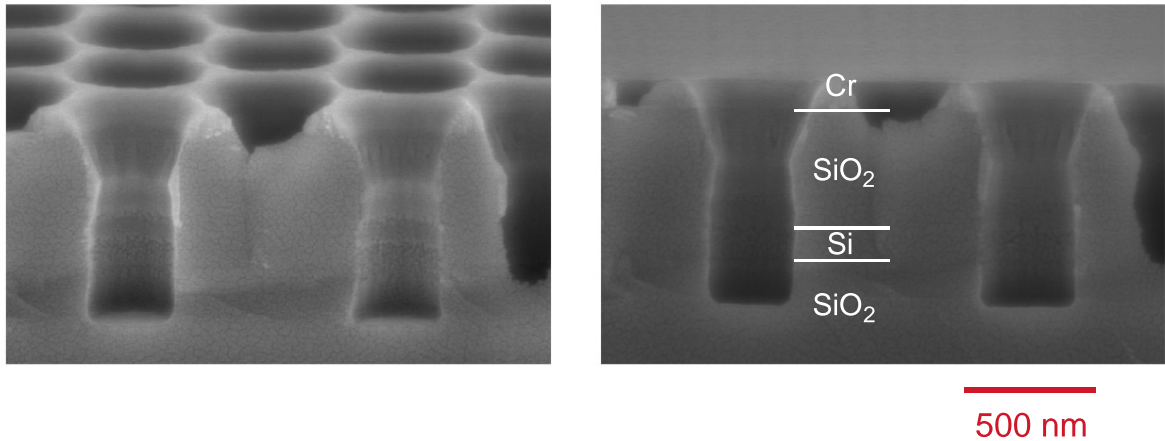


**Figure 4.23:** Cross sectional SEM images of SiO<sub>2</sub>/Si/SiO<sub>2</sub> etching with the ICP recipe presented in table 4.11. The left picture was obtained by tilting the sample 15° towards the surface.

## 4.5 Conclusions

To summarize the results presented in this section, the fabrication of the IOSOI-based PPCs is a very tedious and challenging task. The full fabrication process consists of several steps. Some of them, like the thermal oxidation followed by the wet etching in HF, the Cr sputtering, or the e-beam lithography, are standard processes of the silicon technology. However, the Cr etching with a high aspect ratio was completely unknown and has been optimized in this project.

Although the optimization of the SiO<sub>2</sub>/Si etching process based on the CHF<sub>3</sub>/SF<sub>6</sub> chemistry is not finished yet, this study was necessary to understand the different mechanisms occurring during SiO<sub>2</sub> etching. In particular, we have put into evidence that there exist solutions to all three main problems occurring when etching deep pores in the IOSOI structure (polymer redeposition, charging of the pore walls and underetching at the interfaces between the materials). Therefore, an optimized process combining all these solutions could certainly be available in the near future. A RIE process has also been found, that well preserves the Cr mask and yields almost perfect pore profiles. However, this recipe works only for limited thicknesses.

A second ICP process, based on the C<sub>4</sub>F<sub>8</sub>/Ar chemistry, has been optimized, yielding smooth and vertical pore walls as well as very smooth transitions between the different layers of Si and SiO<sub>2</sub>. This process will be used for the fabrication of the IOSOI photonic crystals for optical measurements.

# 5. Conclusion and Outlook

The aim of this work was to demonstrate the principle and the feasibility of dispersion compensators in planar photonic crystals based on the insulator-on-silicon-on-insulator system. This DC should compensate for the dispersion of a single-wavelength channel with a bandwidth of 0.4 nm, corresponding to 40 GHz at 1.55  $\mu\text{m}$  wavelength. Performing theoretical studies on the properties of PPCs, significantly different from the well-know properties of the infinite 2D PCs, we elaborated and optimized a design of a DC taking into account several requirements for a good device functionality. To show the feasibility of such a device, the experimental fabrication of the IOSOI structure was also performed.

## 5.1 Theory and Design of the Dispersion Compensator

Although the concept of dispersion compensators (DCs) based on the low group velocity and high dispersion in W1 waveguides is well understood in the 2D case, we showed that this problem becomes much more involved in planar photonic crystals (PPCs). Due to the small thickness of the silicon core and the high index contrast between the core and the oxide claddings, the behavior of the insulator-on-silicon-on-insulator (IOSOI) system is fully three-dimensional and combines the properties of a 2D PC with those of a planar waveguide. Therefore, a complete study of the properties of the bulk PPC was necessary before designing the dispersion compensator. As in a planar waveguide, higher-order modes exist and the whole band structure strongly varies with the vertical confinement. The band structure dependence on the different geometrical parameters was investigated, and the best set of parameters turned out to be a relative radius  $r/a = 0.366$ , a relative silicon thickness  $h/a = 0.4-0.42$ , and a relative cladding thickness  $d/a \geq 1$ , where  $a$  is the lattice constant of the PPC. Furthermore, in PPCs the condition of total internal reflection is not fulfilled for all wave vectors. The limit between the vertically-confined modes and the radiative modes is given by the light line. Above the light line, the modes have finite lifetimes; a quantitative study of their radiation losses was performed for the first time in the case of the IOSOI system. All the above effects are due to the planar nature of the photonic crystal, and should be taken into account when designing any device based on planar photonic crystals, because some of them may play an essential role on the device properties. However, most of them were studied in detail for the first time in the present work.

The existence of the cladding modes, with their energy predominantly located in the oxide claddings, is a completely new concept in the physics of planar photonic crystals. In the present work, we showed that the cladding modes are of crucial importance. In particular, the interaction between the lowest cladding mode and the PPC mode at the upper edge of the band gap leads to a non-negligible transmission within the band gap of an IOSOI structure suspended in air. When the IOSOI structure is mounted onto a substrate, corresponding to the experimental configuration, this interaction results in an important loss mechanism, and the interaction region covers a large part of the band gap, strongly limiting the useful frequency range for applications. After theoretically studying all PPC properties, a line defect was introduced into the lattice to

realize the waveguide. Within many different types of waveguides, we chose the W1 waveguide consisting of one row of missing pores, considering its convenient properties for DC applications: it is single-mode in the frequency range of interest, the group velocity is low, and its slope corresponds to a negative dispersion. A full theoretical 3D study of the properties of this W1 waveguide led to the optimized design of a W1 waveguide consisting of one row of missing pores and one row of 5 % larger pores on both sides. This waveguide yields a negative dispersion of -30 ps/nm/mm over a bandwidth of 0.4 nm at 1.55  $\mu\text{m}$  wavelength. Furthermore, we partly addressed the associated coupling issues, leading to the design of a taper and a device fully integrated into a chip. A more detailed qualitative and quantitative study of the coupling efficiencies, with and without taper, to be performed in the future, could be indispensable for determining the efficiency of the taper and accordingly improving its design.

The theoretically predicted properties of the DC require high fabrication precision, because they are very sensitive to variations from the theoretical values and to every experimental imperfections, that limit the accuracy necessary to achieve the desired dispersion properties. Therefore, the tuning of the material properties, to adjust the dispersion after fabrication, is a crucial issue. Different methods of tuning were studied in this work, and it was demonstrated that the tuning of the silicon dielectric constant via free-carrier injection is more promising than that of an infiltrated material into the pores. A method to achieve the tuning experimentally will be completed and included into the full DC design in the future, in order to enlarge this study.

## 5.2 Experimental Fabrication

The complex fabrication of the IOSOI PPCs on silicon-on-insulator (SOI) wafers requires deep silicon oxide and silicon etching, which is performed by the dry etching processes RIE and ICP with a 150 nm-thick chromium (Cr) mask. The first steps in the process are standard processes of the silicon technology, such as thermal oxidation followed by wet etching in HF to build the upper oxide layer, chromium (Cr) sputtering, and electron-beam lithography. The following step is Cr etching using the resist as an etching mask. Though completely unknown in the literature, the patterning of small features in thick Cr layers was successfully optimized in this project. Furthermore, the influence of the process parameters (RF power, gas composition, pressure, sample size and type of resist used) on the Cr etching rate and the selectivity to resist was determined.

In order to readily etch successfully the three layers  $\text{SiO}_2/\text{Si}/\text{SiO}_2$  constituting the IOSOI structure, three main issues had to be addressed simultaneously, the loading effects in the oxide, the polymer redeposition on the pore walls and the smooth transitions at the  $\text{SiO}_2/\text{Si}$  and  $\text{Si}/\text{SiO}_2$  interfaces. We studied all three issues and proposed solutions to all of them, for both plasma chemistries under consideration. As a result, the IOSOI PPCs were successfully fabricated. More importantly, future optical measurements on IOSOI PPC test structures will yield information on the properties of the bulk PPC and the W1 waveguide, such as the attenuation per pore row in the PPC, the quality of the W1 waveguide and the propagation losses in the W1 waveguide. The optical characterization of several long W1 waveguides with different designs and lengths will yield information on the dispersion and the radiation losses in the W1 waveguide. Depending on the measurement results, the design of the DC will correspondingly be modified and optimized further. Moreover, experiments allowing to test the concept of tunability are also planned.

The transfer of the IOSOI PPC fabrication from a laboratory scale to the industry requires some modifications in the fabrication process presented in this work, in order to fit the high throughput

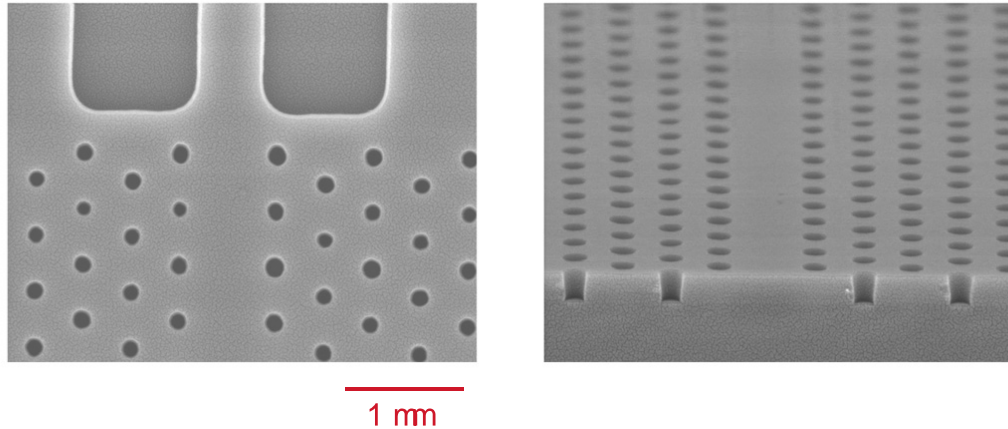


**Figure 5.1:** Top view (left panel) and cross-sectional SEM picture (right panel) of a W1 waveguide patterned in silicon via deep-UV lithography, followed by an ICP etching step. The right panel was obtained by tilting the sample  $15^\circ$  towards the surface. The wavelength of the deep-UV lithography process was 248 nm.

and low cost demanded by industry. In particular, the very long and expensive electron-beam-lithography process should be avoided. Once the complete design of the chip is fixed and no modification has to be brought about anymore, the lithography can be performed via deep-UV lithography [65]. To show the quality of deep-UV lithography at a submicron scale, we have designed two masks in collaboration with IMEC, Belgium. An example of waveguide patterned by deep-UV lithography with a wavelength of 248 nm is presented in fig. 5.1. The lithography was performed directly on 8" silicon wafers, and the silicon layer was subsequently 200 nm-deep etched. It can be seen that holes with diameters as small as 150 nm can be well defined with deep-UV lithography, and the proximity of the wide ridge waveguide trenches close to the small pores does not affect the quality of the PC pores. Within the industrial framework, deep-UV lithography is thus a good alternative to e-beam lithography for the fabrication of the PPC-based DCs.

To conclude, the application of line-defect waveguides in PPCs to dispersion compensation was demonstrated in this work. Further design improvements, exceeding the frame of this dissertation, will be performed in the future to finally fulfill the requirements on the bandwidth and the dispersion slope. Although the experimental fabrication of such devices is very challenging, we have demonstrated that it can be done in principle. Moreover, a theoretical estimate showed that the small experimental imperfections, arising from the process difficulties, may be compensated after fabrication by tuning via free-carrier injection.

## 6. Appendix: Atlas of Waveguide Designs

Several waveguide designs have been studied before selecting the W1 waveguide, made of one row of missing pores, as the initial design to build the dispersion compensator. The most important are:

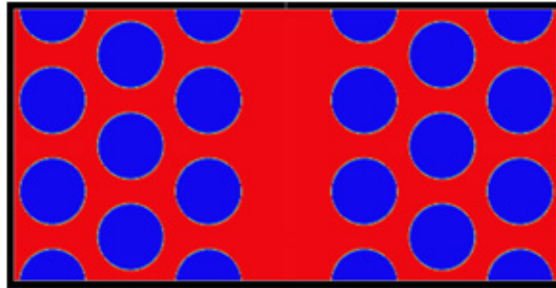
- the W1 waveguide made of one row of missing pores
- the W1 waveguide made of one row of smaller pores
- the W3 waveguide made of three rows of missing pores
- the W3 waveguide made of three rows of smaller pores
- the W3 waveguide made of one row of pores in its center and one row of missing pores on both sides
- the W3 waveguide consisting of another photonic crystal having the same relative radius and a smaller lattice constant

The design and properties of each waveguide type are presented in the following. Only 2D calculations, using the MIT package, have been performed in this preliminary study. Although the deviations between the results of 2D and full 3D computations are non negligible for systems with high vertical index contrast like the IOSOI structure, they are expected to be small compared to the differences between two types of waveguides. As a general rule, only the modes located in the lower half of the band gap are considered. Indeed, in the PPC the upper defect modes are above the light line, and consequently not suitable for lossless waveguiding.

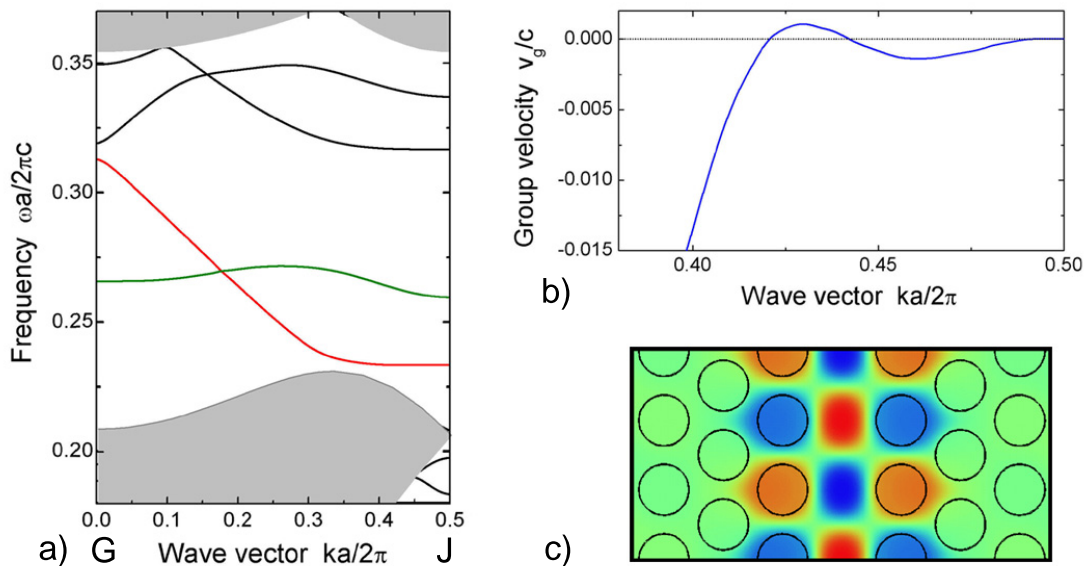
### W1 waveguide made of one row of missing pores

Fig. 6.1 shows the design of the W1 waveguide made of one row of missing pores in a hexagonal lattice of air pores in silicon with relative radius  $r/a = 0.366$ . The corresponding projected band structure along the  $\Gamma$ -J path is presented in fig. 6.2a. As can be noticed in fig. 6.2a, only two modes exist in the lower half of the band gap. Since one of them (green mode) has a laterally even symmetry, it cannot be excited by an external plane wave. Therefore, the only candidate for dispersion compensation is the red mode. The group velocity of this mode in the wave vector range of interest  $ka/2\pi = 0.38-0.5$  is shown in fig. 6.2b, and its  $H_z$ -field distribution at the J-point is shown in fig. 6.2c. Due to the very small group velocity, a high dispersion is expected. The slope of the group velocity with two sign inversions is not very convenient. However, this slope should change with the introduction of the finite slab thickness and can be adjusted by fine tuning of the design, as discussed in chapter 3. Therefore, this mode is a good candidate for the dispersion compensator.

Several other designs, derived from the W1 waveguide made of one row of missing pores, have been studied. They are obtained by increasing or decreasing the radius of the pore row on both sides of the defect. For a smaller pore radius, no defect band with satisfying group velocity variations has been found. The results for a larger pore radius are discussed in section 3.2.2.



**Figure 6.1:** Design of the W1 waveguide made of one row of missing pores in the  $\Gamma$ -K direction. The blue and red colors represent air and silicon, respectively.



**Figure 6.2:** a) Band structure of the 2D PC with the waveguide design presented in fig. 6.1. The red band indicates the mode of interest for dispersion compensation and the green band is the other defect mode that is low enough in frequency within the band gap to exist also below the light line in the 3D case. The other bands are shown in black. b) Group velocity and c) field distribution at the J-point of the red mode.

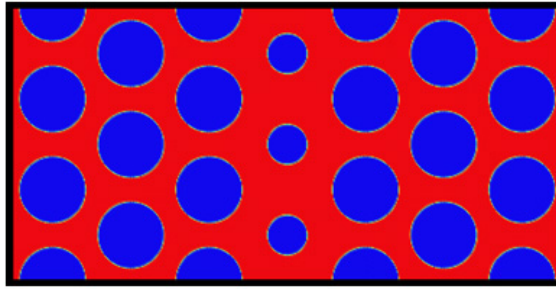


**Figure 6.3:** Design of the W1 waveguide made of one row of smaller pores in the  $\Gamma$ -K direction. The blue and red colors represent air and silicon, respectively.

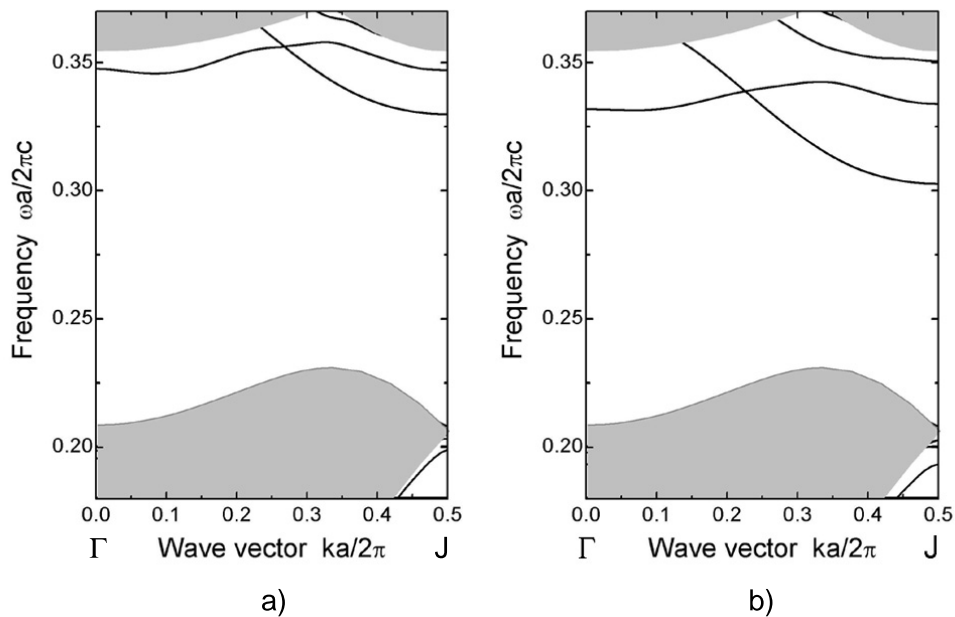
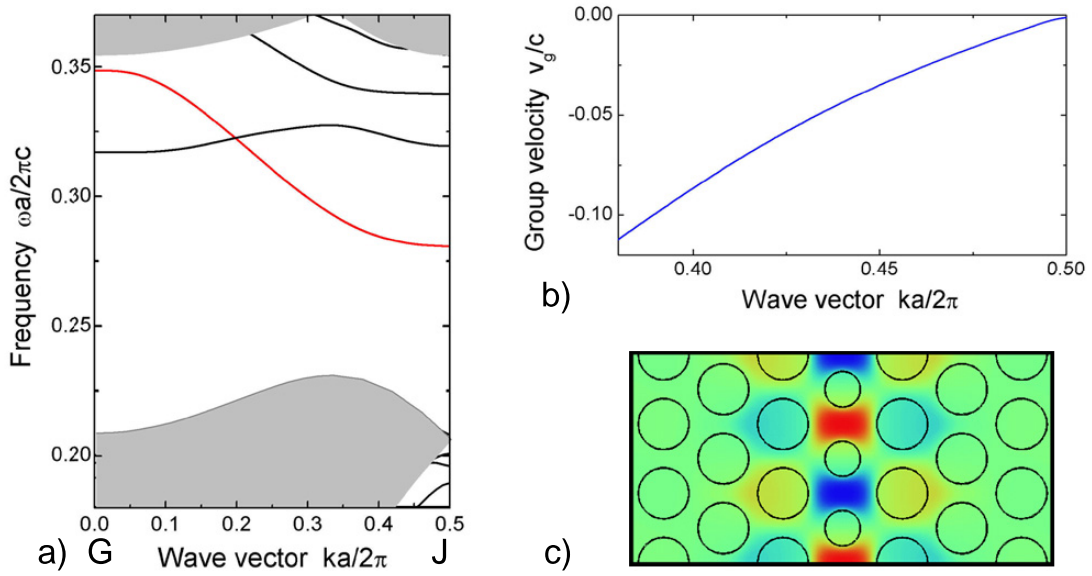


**Figure 6.4:** Band structures of the 2D PC with the waveguide design presented in fig. 6.3, with a relative radius of a)  $r/a = 0.33$  and b)  $r/a = 0.295$  for the smaller pores (10 % and 20 % smaller than the lattice pores, respectively). For these two designs, no defect modes are low enough in frequency within the band gap to exist also in 3D below the light line.

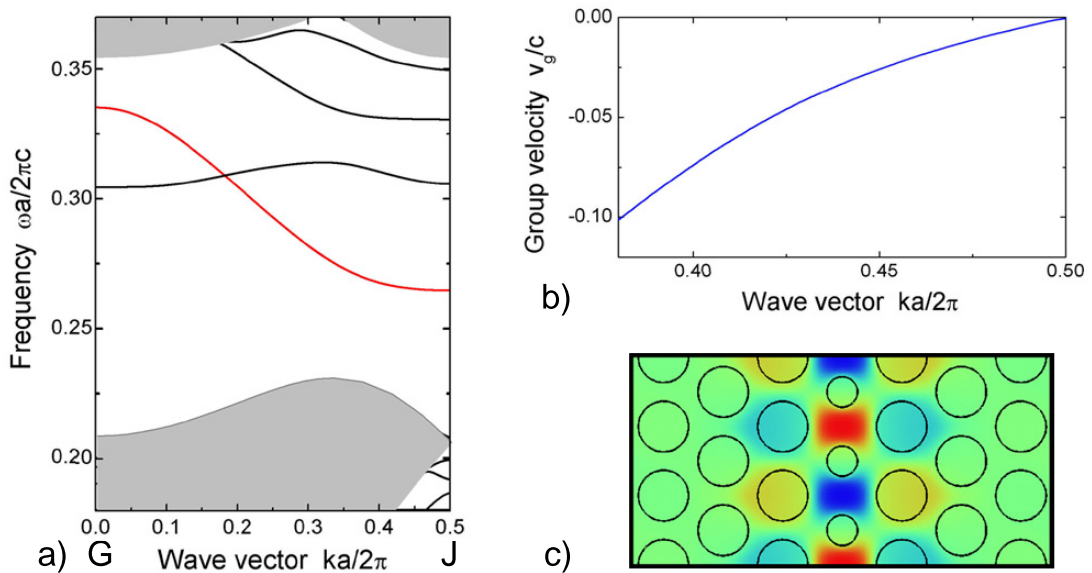
### W1 waveguide made of one row of smaller pores

Fig. 6.3 shows the design of the W1 waveguide made of one row of smaller pores in a hexagonal lattice of air pores in silicon with relative radius  $r/a = 0.366$ . The corresponding projected band structures along the  $\Gamma$ -J path for the two cases where the waveguide consists of 10 % and 20 % smaller pores are presented in fig. 6.4a and b, respectively. As can be noticed in fig. 6.4, the only defect modes existing in the band gap are lying very high in frequency. Therefore, these designs are not suitable for applications in the case of a 3D structure with finite thickness.

The projected band structures along the  $\Gamma$ -J path for the two cases where the waveguide consists of 30 % and 40 % smaller pores are presented in fig. 6.5 and fig. 6.6, respectively. Although a band exists low enough in the band gap (red band) with correspondingly convenient group velocity and mode symmetry, this type of waveguide design with two very different pore radii



**Figure 6.5:** a) Band structure of the 2D PC with the waveguide design presented in fig. 6.3, with a relative radius of  $r/a = 0.255$  for the smaller pores (30 % smaller than the lattice pores). The red band indicates the mode of interest for dispersion compensation. The other bands are shown in black. b) Group velocity and c) field distribution at the J-point of the red mode.



**Figure 6.6:** a) Band structure of the 2D PC with the waveguide design presented in fig. 6.3, with a relative radius of  $r/a = 0.220$  for the smaller pores (40 % smaller than the lattice pores). The red band indicates the mode of interest for dispersion compensation. The other bands are shown in black. b) Group velocity and c) field distribution at the J-point of the red mode.

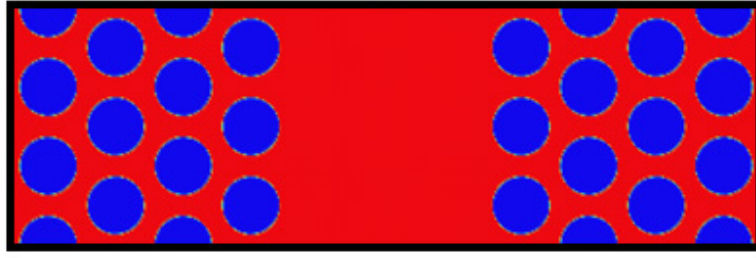


**Figure 6.7:** Design of the W3 waveguide made of three rows of missing pores in the  $\Gamma$ -K direction. The blue and red colors represent air and silicon, respectively.

for the waveguide and the surrounding lattice may be very difficult to realize experimentally. In most dry etching processes, the etching rate depends strongly on the feature size. Consequently, it is better to have only similar pore sizes in the waveguide design.

The case of waveguides consisting of a pore row with larger radius than in the surrounding lattice has also been studied. However, the same problem arises as above. A large pore radii difference, between the waveguide and the lattice, is necessary, for some defect modes to be located at a convenient frequency within the band gap.

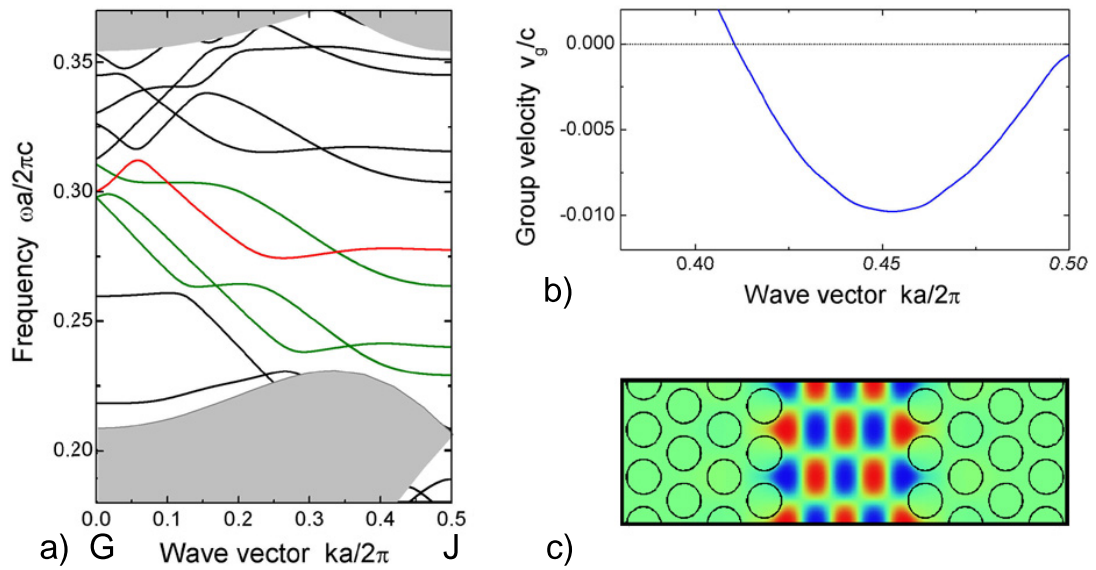
### W3 waveguide made of three rows of missing pores

Fig. 6.7 shows the design of the W3 waveguide made of three rows of missing pores in a hexagonal lattice of air pores in silicon with relative radius  $r/a = 0.366$ . The corresponding projected band structure along the  $\Gamma$ -J path is presented in fig. 6.8a. Among the several modes that are located in the lower half of the band gap (green modes), we select the red one as a candidate for dispersion compensation. The group velocity of this mode in the wave vector range of interest  $ka/2\pi = 0.38$ -0.5 is shown in fig. 6.8b, and its  $H_z$ -field distribution is shown in fig. 6.8c. Although the low group velocity is convenient for a high dispersion, this waveguide is multimode, as can be verified in fig. 6.8a. Consequently, it is not convenient for applications to dispersion compensation. While coupling light from the external light source, all modes existing at this frequency would be excited, not only the band of interest.

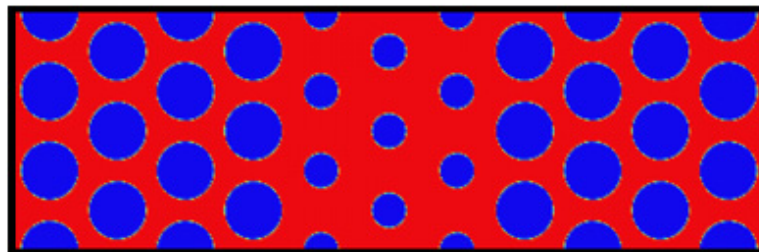
### W3 waveguide made of three rows of smaller pores

Fig. 6.9 shows the design of the W3 waveguide made of three rows of smaller pores in a hexagonal lattice of air pores in silicon with relative radius  $r/a = 0.366$ . The corresponding projected band structures along the  $\Gamma$ -J path for the two cases where the waveguide consists of 10 % and 20 % smaller pores are presented in fig. 6.10a and b, respectively. As can be noticed in fig. 6.10, the defect modes existing in the band gap are lying very high in frequency. Therefore, these designs are not suitable for applications in the case of a 3D structure with finite thickness.

The projected band structures along the  $\Gamma$ -J path for the two cases where the waveguide consists of 30 % and 40 % smaller pores are presented in fig. 6.11 and fig. 6.12, respectively. Some bands exist with frequencies low enough within the band gap (green bands). Among them, the



**Figure 6.8:** a) Band structure of the 2D PC with the waveguide design presented in fig. 6.7. The red band indicates the mode of interest for dispersion compensation and the green bands are the defect modes that are low enough in frequency within the band gap to exist also in 3D below the light line. The other bands are shown in black. b) Group velocity and c) field distribution at the J-point of the red mode.



**Figure 6.9:** Design of the W3 waveguide made of three rows of smaller pores in the  $\Gamma$ -K direction. The blue and red colors represent air and silicon, respectively.

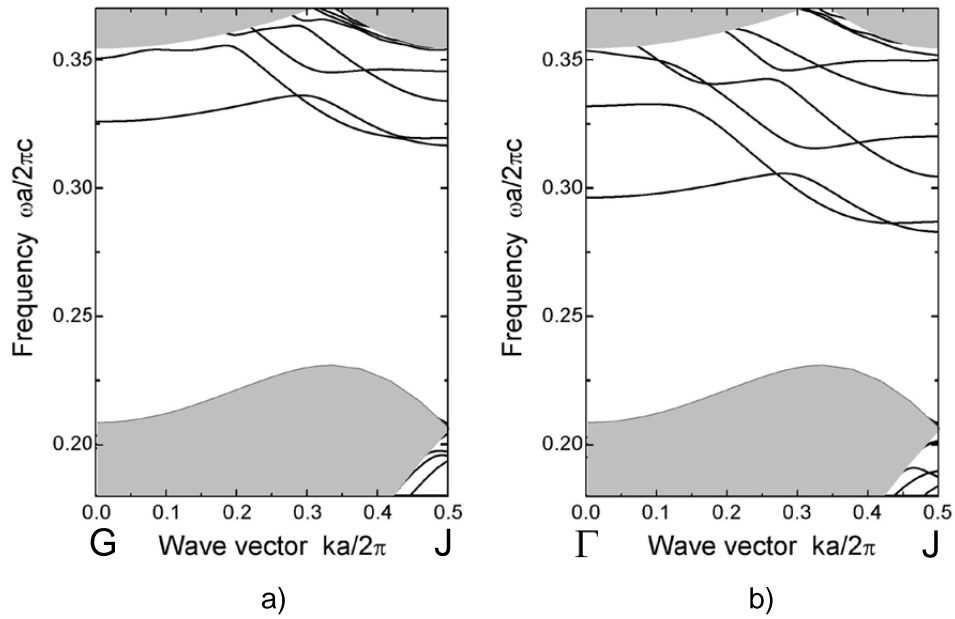


**Figure 6.10:** a) Band structures of the 2D PC with the waveguide design presented in fig. 6.9, with a relative radius of a)  $r/a = 0.33$  and b)  $r/a = 0.295$  for the smaller pores (10 % and 20 % smaller than the lattice pores, respectively). For these two designs no defect modes are low enough in frequency within the band gap to exist also in 3D below the light line.

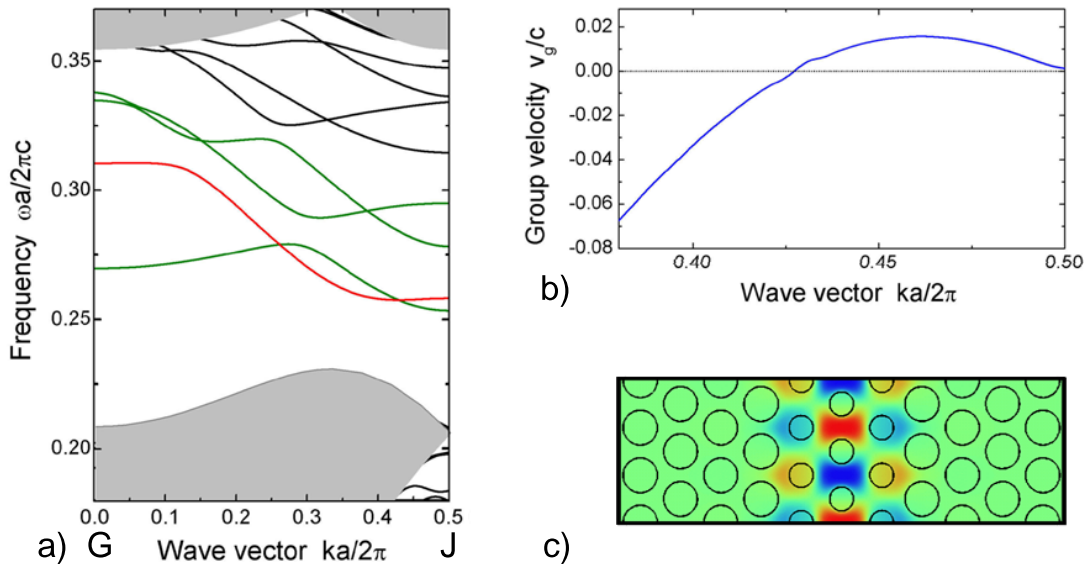


**Figure 6.11:** a) Band structure of the 2D PC with the waveguide design presented in fig. 6.9, with a relative radius of  $r/a = 0.256$  for the smaller pores (30 % smaller than the lattice pores). The red band indicates the mode of interest for dispersion compensation and the green bands are the defect modes that are low enough in frequency within the band gap to exist also in 3D below the light line. The other bands are shown in black. b) Group velocity and c) field distribution at the J-point of the red mode.

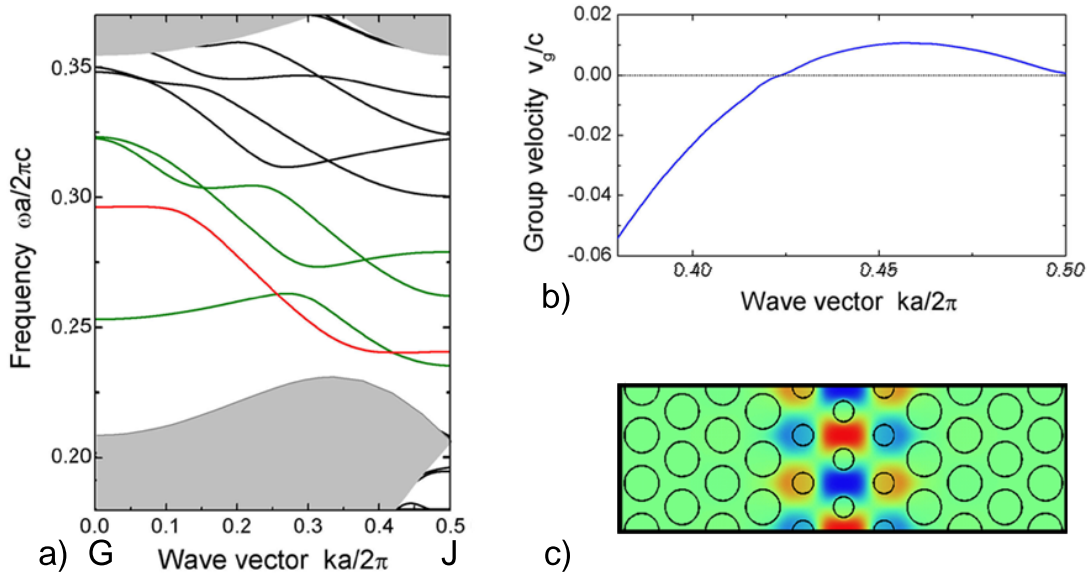


**Figure 6.12:** a) Band structure of the 2D PC with the waveguide design presented in fig. 6.9, with a relative radius of  $r/a = 0.220$  for the smaller pores (40 % smaller than the lattice pores). The red band indicates the mode of interest for dispersion compensation and the green bands are the defect modes that are low enough in frequency within the band gap to exist also in 3D below the light line. The other bands are shown in black. b) Group velocity and c) field distribution at the J-point of the red mode.

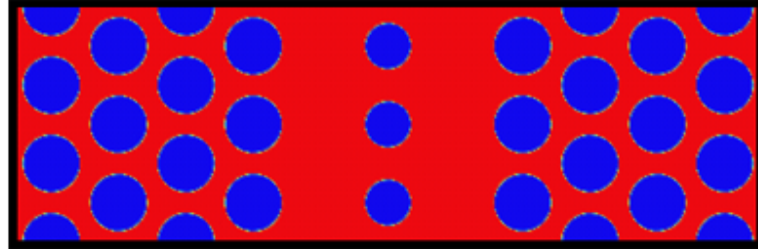
red mode has a convenient group velocity and mode symmetry. However, these designs are no good candidates for dispersion compensation, since the waveguides are not single-mode in the frequency range of interest. Furthermore, as in the case of the W1 waveguide made of one row of smaller pores, this structure may be very difficult to realize experimentally, because of the large pore radius differences between the waveguide and its surrounding.

For each relative radius value of the waveguide pores, several other designs derived from the W3 waveguide made of three rows of smaller pores have been studied. They are obtained by varying the pore radii of the central pore row relatively to the side rows. However, no significant improvement of the waveguide properties has been observed.

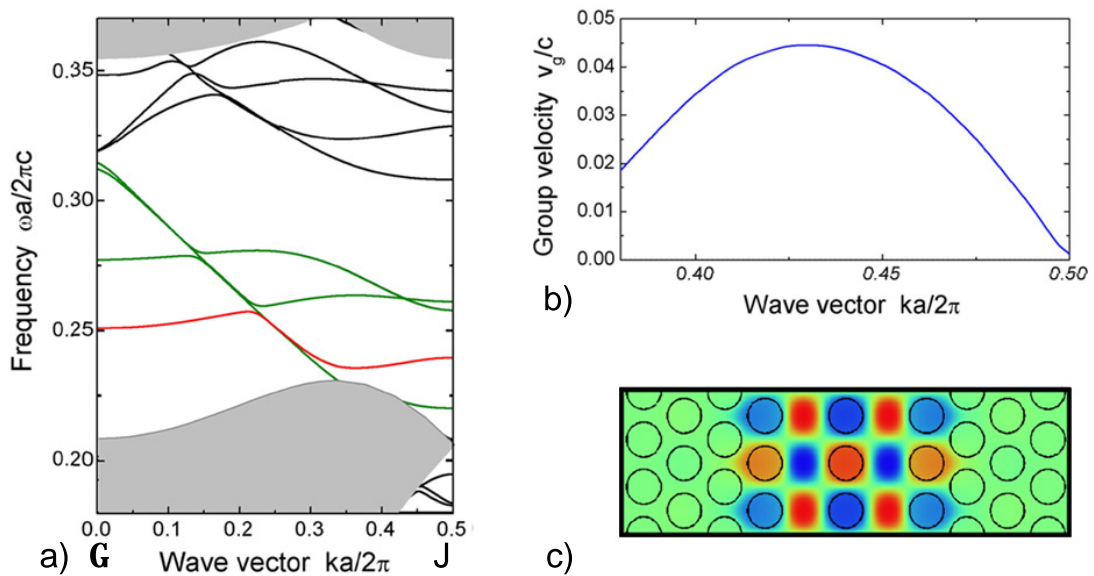
### W3 waveguide made of one row of pores in its center, surrounded by one row of missing pores on both sides

Fig. 6.13 shows the design of the W3 waveguide made of one row of pores in its center, surrounded by one row of missing pores on both sides, in a hexagonal lattice of air pores in silicon with relative radius  $r/a = 0.366$ . The corresponding projected band structure along the  $\Gamma$ -J path, in the case where the pore radius of the central pore row is  $r/a = 0.366$ , is presented in fig. 6.14a. Among the several modes that are located in the lower half of the band gap (green modes), we select the red one as a candidate for dispersion compensation. The group velocity of this mode in the wave vector range of interest  $ka/2\pi = 0.38$ -0.5 is shown in fig. 6.14b, and its  $H_z$ -field distribution is shown in fig. 6.14c. However, this waveguide is not single-mode, and therefore not convenient for applications to dispersion compensation.

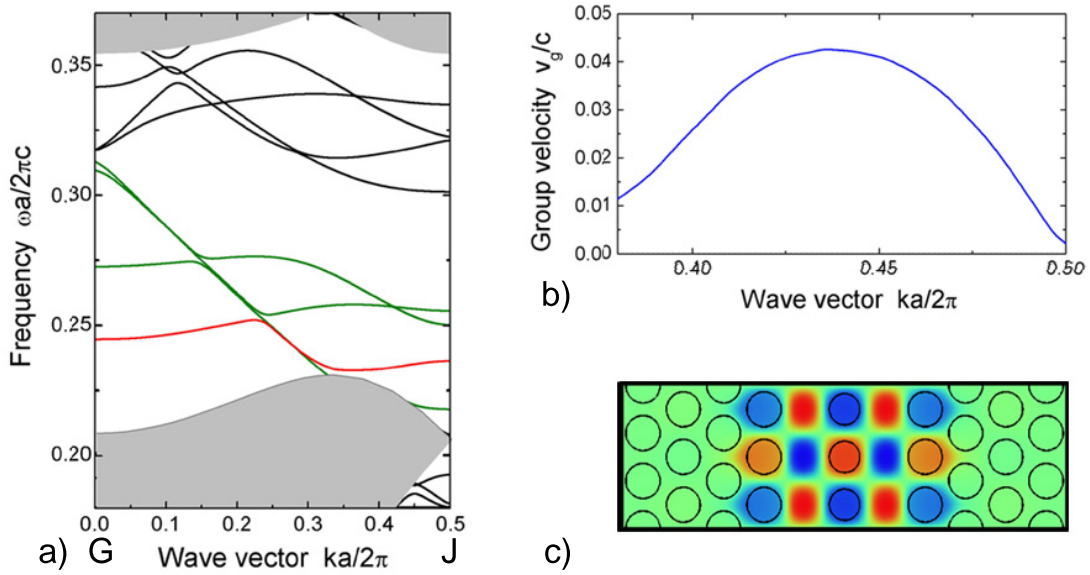
By varying the radius of the central pore line, the frequency of the defect modes is shifted, so that another mode can become a good candidate for dispersion compensation, as illustrated in



**Figure 6.13:** Design of the W3 waveguide, made of one row of pores in its center, surrounded on both sides by a row of missing pores, in the  $\Gamma$ -K direction. The blue and red colors represent air and silicon, respectively.



**Figure 6.14:** a) Band structure of the 2D PC with the waveguide design presented in fig. 6.13, with a relative radius  $r/a = 0.366$  for the central pores (same radius as the lattice pores). The red band indicates the mode of interest for dispersion compensation and the green bands are the defect modes that are low enough in frequency within the band gap to exist also in 3D below the light line. The other bands are shown in black. b) Group velocity and c) field distribution at the J-point of the red mode.



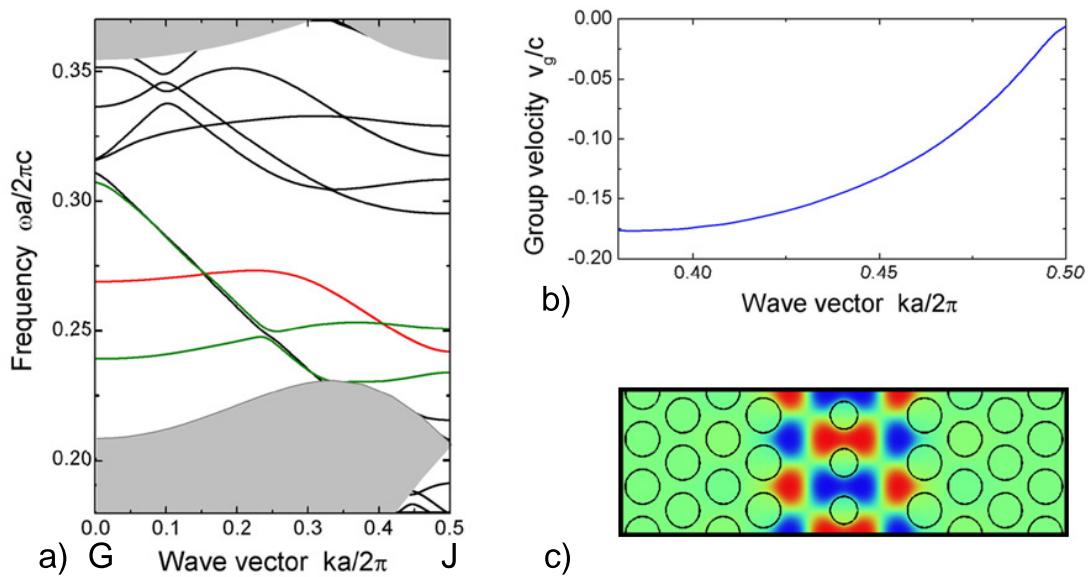
**Figure 6.15:** a) Band structure of the 2D PC with the waveguide design presented in fig. 6.13, with a relative radius of  $r/a = 0.33$  for the central pores (10 % smaller than the lattice pores). The red band indicates the mode of interest for dispersion compensation and the green bands are the defect modes that are low enough in frequency within the band gap to exist also in 3D below the light line. The other bands are shown in black. b) Group velocity and c) field distribution at the J-point of the red mode.

fig. 6.15 and 6.16 in the case of a smaller radius. However, the waveguide is still multimode in the frequency range of interest.

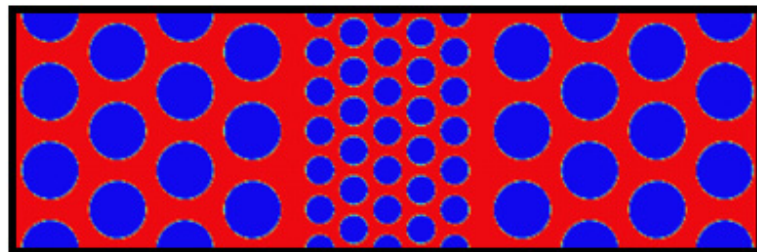
### W3 waveguide consisting of another photonic crystal having the same relative radius and a twice smaller lattice constant

Fig. 6.17 shows the design of the W3 waveguide consisting of another photonic crystal having the same relative radius and a lattice constant twice smaller than in the surrounding lattice. The bulk PC consists of a hexagonal lattice of air pores in silicon with relative radius  $r/a = 0.366$ . The corresponding projected band structure along the  $\Gamma$ -J path is presented in fig. 6.18a. The group velocity of the selected red mode in the wave vector range of interest  $ka/2\pi = 0.38$ -0.5 is shown in fig. 6.14b, and its  $H_z$ -field distribution is shown in fig. 6.14c. However, again, this waveguide is not convenient for applications to dispersion compensation, because it is not single-mode, and the large pore radius differences between the waveguide and its surrounding makes its experimental fabrication very difficult.

Several other designs of this type have been studied, obtained by varying the lattice constant of the photonic crystal constituting the defect. However, the defect modes can be computed in 3D with the MIT package only for this particular value of the lattice constant, being twice smaller than in the surrounding lattice. Taking any other lattice constant within the waveguide, the translation symmetry in the propagation direction is changed. For example, in the case of a 90 % smaller lattice constant within the waveguide than in the lattice, the periodicity in the propagation direction is  $9a$ . It leads to a nine time smaller Brillouin zone, where the band gap lies far away above the light line. Even if these modes should still be vertically confined, they are lying within the numerous back-folded modes of the waveguide structure and very difficult to sort out, as discussed in section 2.3.3.



**Figure 6.16:** a) Band structure of the 2D PC with the waveguide design presented in fig. 6.13, with a relative radius of  $r/a = 0.293$  for the central pores (20 % smaller than the lattice pores). The red band indicates the mode of interest for dispersion compensation and the green bands are the defect modes that are low enough in frequency within the band gap to exist also in 3D below the light line. The other bands are shown in black. b) Group velocity and c) field distribution at the J-point of the red mode.



**Figure 6.17:** Design of the W3 waveguide, consisting of another PC, in the  $\Gamma$ -K direction. The second PC has the same relative radius and a lattice constant twice smaller than the lattice of the bulk PC. The blue and red colors represent air and silicon, respectively.

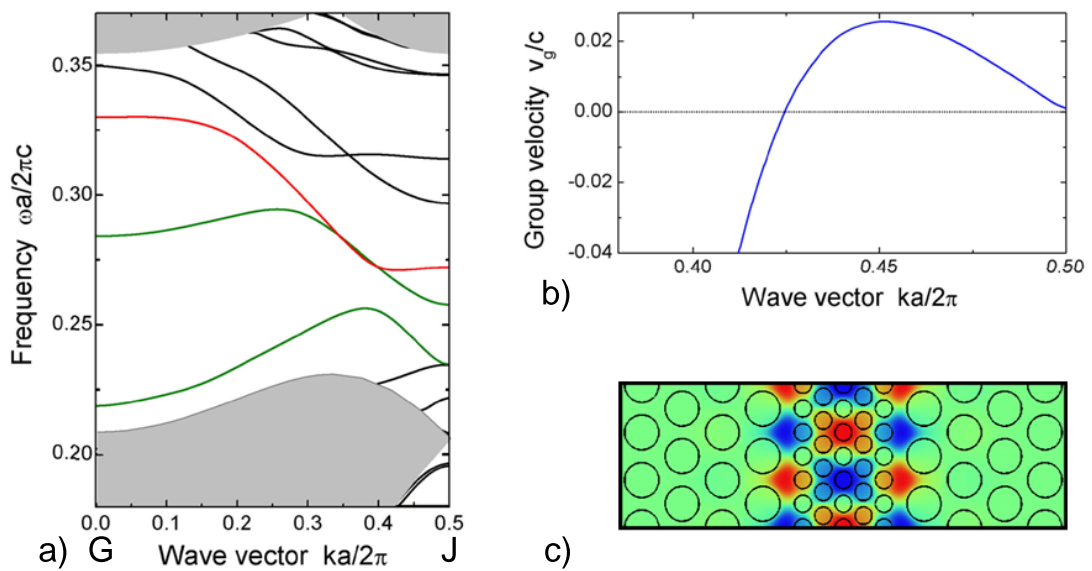


**Figure 6.18:** a) Band structure of the 2D PC with the waveguide design presented in fig. 6.17. The red band indicates the mode of interest for dispersion compensation and the green bands are the defect modes that are low enough in frequency within the band gap to exist also in 3D below the light line. The other bands are shown in black. b) Group velocity and c) field distribution at the J-point of the red mode.

# List of Abbreviations

1D	one dimensional
2D	two dimensional
3D	three dimensional
CCW	coupled-cavity waveguide
DC	dispersion compensator
DCF	dispersion compensating fiber
FBG	fiber Bragg grating
FDTD	finite-difference time-domain
ICP	inductively-coupled plasma
IOSOI	insulator-on-silicon-on-insulator
PBG	photonic band gap
PC	photonic crystal
PPC	planar photonic crystal
RF	radio-frequency
RIE	reactive ion etching
SEM	scanning electron microscope
SMF	single-mode fiber
SOI	silicon-on-insulator
TE	transverse electric
TM	transverse magnetic
UV	ultra-violet
WDM	wavelength division multiplexing
$W_n$ waveguide	waveguide having a width of $n$ pore rows

# Bibliography

- [1] S. John, *Strong localization of photons in certain disordered dielectric lattices*, Phys. Rev. Lett. **58**, 23 (1987)
- [2] E. Yablonovitch, *Inhibited spontaneous emission in solid-state physics and electronics*, Phys. Rev. Lett. **58**, 20 (1987)
- [3] J. D. Joannopoulos, R. D. Meade and J. N. Winn, *Photonic crystals, molding the flow of light*, Princeton Academic Press, Princeton, NJ (1995)
- [4] A. Blanco, E. Chomski, S. Grachtak, M. Ibsate, S. John, S. W. Leonard, C. Lopez, F. Meseguer, H. Miguez, J. P. Mondia, G. A. Ozin, O. Toader and H. M. van Driel, *Large-scale synthesis of a silicon photonic crystal with a complete three-dimensional bandgap near 1.5 micrometres*, Nature **405**, 437 (2000)
- [5] J. E. G. J. Wijnhoven, L. Bechger and W. L. Vos, *Fabrication and characterization of large macroporous photonic crystals in titania*, Chem. Mater. **13**, 4486 (2001)
- [6] S. Noda, K. Tomoda, N. Yamamoto and A. Chutinan, *Full three-dimensional photonic bandgap crystals at near-infrared wavelengths*, Science **289**, 604 (2000)
- [7] S. Y. Lin, J. G. Fleming, R. Lin, M. M. Sigalas, R. Biswas and K. M. Ho, *Complete three-dimensional photonic bandgap in a simple cubic structure*, J. Opt. Soc. Am. B **18**, 32 (2001)
- [8] J. Schilling, F. Müller, S. Matthias, R. B. Wehrspohn, U. Gösele and K. Busch, *Three-dimensional photonic crystals based on macroporous silicon with modulated pore diameter*, Appl. Phys. Lett. **78**, 1180 (2001)
- [9] A. Birner, R. B. Wehrspohn, U. Gösele and K. Busch, *Silicon-based photonic crystals*, Adv. Mater. **13**, 377 (2001)
- [10] R. D. Meade, A. Devenyi, J. D. Joannopoulos, O. L. Alerhand, D. A. Smith and K. Kash, *Novel applications of photonic band gap materials: Low-loss bends and high Q cavities*, J. Appl. Phys. **75**, 4753 (1994)
- [11] T. F. Krauss, R. M. De La Rue and S. Brand, *Two-dimensional photonic-bandgap structures operating at near-infrared wavelengths*, Nature **383**, 699 (1996)
- [12] S. G. Johnson, S. Fan, P. R. Villeneuve, J. D. Joannopoulos and L. A. Kolodziejski, *Guided modes in photonic crystal slabs*, Phys. Rev. B **60**, 5751 (1999)
- [13] P. R. Villeneuve, S. Fan, S. G. Johnson and J. D. Joannopoulos, *Three-dimensional photon confinement in photonic crystals of low-dimensional periodicity*, IEE Proc. Optoelectron. **145**, 384 (1998)
- [14] C. Weisbuch, H. Benisty, S. Olivier, M. Rattier, C. J. M. Smith and T. F. Krauss, *Advances in photonic crystals*, Phys. Stat. Sol. **221**, 93 (2000)
- [15] O. Painter, J. Vučković and A. Scherer, *Defect modes of a two-dimensional photonic crystal in an optically thin dielectric slab*, J. Opt. Soc. Am. B **16**, 275 (1999)

- [16] S. Mahnkopf, M. Kamp, A. Forchel and R. März, *Tunable distributed feedback laser with photonic crystal mirrors*, Appl. Phys. Lett. **82**, 2942 (2003)
- [17] R. B. Wehrspohn, S. L. Schweizer, J. Schilling, T. Geppert, C. Jamois, R. Glatthaar, P. Hahn, A. Feisst and A. Lambrecht, *Application of photonic crystals for gaz detection and sensing*, in *Photonic crystals: Advances in design, fabrication and characterization*, ed. by K. Busch, S. Lölkes, R. B. Wehrspohn and H. Föll, Wiley, 238 (2004)
- [18] M. Lončar, A. Scherer and Y. Qiu, *Photonic crystal laser sources for chemical detection*, Appl. Phys. Lett. **82**, 4648 (2003)
- [19] L. Wu, M. Mazilu, T. Karle and T. F. Krauss, *Superprism phenomena in planar photonic crystals*, IEEE J. Quantum Electron. **38**, 915 (2002)
- [20] K. B. Chung and S. W. Hong, *Wavelength demultiplexers based on the superprism phenomena in photonic crystals*, Appl. Phys. Lett. **81**, 1549 (2002)
- [21] D. Taillaert, W. Bogaerts, P. Bienstman, T. F. Krauss, P. Van Daele, I. Moerman, S. Verstyuyft, K. De Mesel and R. Baets, *An out-of-plane grating coupler for efficient butt-coupling between compact planar waveguides and single-mode fibers*, IEEE J. Quantum Electron. **38**, 949 (2002)
- [22] S. Noda, A. Chutinan and M. Imada, *Trapping and emission of photons by a single defect in a photonic bandgap structure*, Nature **407**, 608 (2000)
- [23] M. Megens, J. Wijnhoven, A. Lagendijk and W. L. Vos, *Fluorescence lifetimes and linewidths of dye in photonic crystals*, Phys. Rev. A **59**, 4727 (1999)
- [24] K. Busch and S. John, *Photonic band gap formation in certain self-organizing systems*, Phys. Rev. E **58**, 3896 (1998)
- [25] F. Genereux, S. W. Leonard, H. M. van Driel, A. Birner and U. Gösele, *Large birefringence in two-dimensional silicon photonic crystals*, Phys. Rev. B **63**, 161101 (2001)
- [26] H. Kosaka, T. Kawashima, A. Tomita, M. Notomi, T. Tamamura, T. Sato and S. Kawakami, *Superprism phenomena in photonic crystals*, Phys. Rev. B **58**, 10096 (1998)
- [27] W. Park and C. J. Summers, *Extraordinary refraction and dispersion in two-dimensional photonic-crystal slabs*, Opt. Lett. **27**, 1397 (2002)
- [28] C. Luo, S. G. Johnson, J. D. Joannopoulos and J. B. Pendry, *All-angle negative refraction without negative effective index*, Phys. Rev. B **65**, 201104 (2002)
- [29] M. Notomi, *Theory of light propagation in strongly modulated photonic crystals: Refractionlike behavior in the vicinity of the photonic band gap*, Phys. Rev. B **62**, 10696 (2000)
- [30] see, e.g., the special issue on PBG materials in IEEE J. Quantum Electron. **38**, 724-963 (2002)
- [31] K. C. Kao and G. A. Hockham, *Dielectric-fiber surface waveguides for optical frequencies*, Proc. IEE **113**, 1151 (1966)
- [32] F. P. Kapron, D. B. Keck and R. D. Maurer, *Radiation losses in glass optical waveguides*, Appl. Phys. Lett. **17**, 423 (1970)
- [33] N. Uchida, *Development and future prospect of optical fiber technologies*, IEICE Trans. Electron. **E85-C**, 868 (2002)

- [34] J. F. Brennan, *Dispersion compensating gratings for the C-band*, Photonics Spectra, 159 (June 2001)
- [35] H. Izadpanah, C. Lin, J. Gimlett, H. Johnson, W. Way and P. Kaiser, *Dispersion-compensation for upgrading interoffice networks built with 1310nm optimized SMFs using an equalizer fiber, EDFAs and 13130/1550nm WDM*, Tech. Digest Opt. Fiber Commun. Conf., San Jose, USA, PD15, 371 (1992)
- [36] C. C. Chang, H. P. Sardesai and A. M. Weiner, *Dispersion-free fiber transmission for femtosecond pulses by use of a dispersion-compensating fiber and a programmable pulse shaper*, Opt. Lett. **23**, 283 (1998)
- [37] S. Kawanishi, H. Takara, T. Morioka, O. Kamatani, K. Takiguchi, T. Kitoh, and M. Saruwatari, *Single-channel 400Gbit/s time-division-multiplexed transmission of 0.98ps pulses over 40 km employing dispersion slope compensation*, Electron. Lett. **32**, 916 (1996)
- [38] L. Dong, M. J. Cole, A. D. Ellis, M. Durkin, M. Ibsen, V. Gusmeroli and R. I. Laming, Tech. Digest of the Opt. Fiber Commun. Conf., Washington D.C., USA, 391 (1997)
- [39] A. Othonos, *Fiber Bragg gratings*, Rev. Sci. Instrum. **68**, 4309 (1997)
- [40] V. A. Semenov, A. V. Belov, E. M. Dianov, A. A. Abramov, M. M. Bubnov, S. L. Semjonov, A. G. Shchebunjaev, V. F. Khopin, A. N. Guryanov and N. N. Vechkanov, *Broadband dispersion-compensating fiber for high-bit-rate transmission network use*, Appl. Optics **34**, 5331 (1995)
- [41] T. Sugihara, K. Ishida, K. Shimomura, K. Shimizu and Y. Kobayashi, *Adaptive dispersion compensation for 40 Gbit/s RZ transmission by using Bragg gratings*, IEICE Trans. Electron. **E84-C**, 527 (2001)
- [42] M. Agio and L. C. Andreani, *Complete photonic band gap in a two-dimensional chess-board lattice*, Phys. Rev. B **61**, 15519 (2000)
- [43] A. Birner, *Optische Wellenleiter und Mikroresonatoren in zweidimensionalen photonischen Kristallen aus makroporösem Silizium*, PhD thesis, University of Halle (2000)
- [44] D. Cassagne, C. Jouanin and D. Bertho, *Photonic band gaps in a two-dimensional graphite structure*, Phys. Rev. B **52**, R2217 (1995)
- [45] J.-Y. Ye, V. Mizeikis, Y. Xu, S. Matsuo and H. Misawa, *Fabrication and optical characteristics of silicon-based two-dimensional photonic crystals with honeycomb lattice*, Opt. Commun. **211**, 205 (2002)
- [46] R. D. Meade, O. Alerhand and J. D. Joannopoulos, *Handbook of photonic band gap materials*, available on request
- [47] S. G. Johnson and J. D. Joannopoulos, *Block-iterative frequency-domain methods for Maxwell's equations in a planewave basis*, Opt. Express **8**, 173 (2001)
- [48] A. Yariv, Y. Xu, R. K. Lee and A. Scherer, *Coupled-resonator optical waveguide: a proposal and analysis*, Opt. Lett. **24**, 711 (1999)
- [49] S. Olivier, C. Smith, M. Rattier, H. Benisty, C. Weisbuch, T. Krauss, R. Houdré and U. Oesterle, *Miniband transmission in a photonic crystal coupled-resonator optical waveguide*, Opt. Lett. **26**, 1019 (2001)
- [50] T. J. Karle, D. H. Brown, R. Wilson, M. Steer and T. F. Krauss, *Planar photonic crystal coupled cavity waveguides*, IEEE J. Selec. Top. Quantum Electron. **8**, 909 (2002)

- [51] M. Lončar, T. Doll, J. Vučković and A. Scherer, *Design and Fabrication of Silicon Photonic Crystal Optical Waveguides*, IEEE J. Lightwave Technol. **18**, 1402 (2000)
- [52] S. G. Johnson, P. Villeneuve, S. Fan and J. D. Joannopoulos, *Linear waveguides in photonic-crystal slabs*, Phys. Rev. B **62**, 8212 (2000)
- [53] M. Notomi, A. Shinya, K. Yamada, J. Takahashi, C. Takahashi and I. Yokohama, *Structural tuning of guiding modes of line-defect waveguides of silicon-on-insulator photonic crystal slabs*, IEEE J. Quantum Electron. **38**, 736 (2002)
- [54] C. J. M. Smith, H. Benisty, S. Olivier, M. Rattier, C. Weisbuch, T. F. Krauss, R. M. De La Rue, R. Houdré and U. Oesterle, *Low-loss channel waveguides with two-dimensional photonic crystal boundaries*, Appl. Phys. Lett. **77**, 2813 (2000)
- [55] P. Lalanne, *Electromagnetic analysis of photonic crystal waveguides operating above the light cone*, IEEE J. Quantum Electron. **38**, 800 (2002)
- [56] C. Jamois, R. B. Wehrspohn, C. Hermann, O. Hess, L.C. Andreani and U. Gösele, *Silicon-Based Two-Dimensional Photonic Crystal Waveguides*, Photonics and Nanostructures: Fundamentals and Applications **1**, 1 (2003)
- [57] W. T. Lau and S. Fan, *Creating large bandwidth line defects by embedding dielectric waveguides into photonic crystal slabs*, Appl. Phys. Lett. **81**, 3915 (2002)
- [58] K. Hosomi and T. Katsuyama, *A dispersion compensator using coupled defects in a photonic crystal*, IEEE J. Quantum Electron. **38**, 825 (2002)
- [59] A. Martínez, A. García, P. Sanchis and J. Martí, *Group velocity and dispersion model of coupled-cavity waveguides in photonic crystals*, J. Opt. Soc. Am. A **20**, 147 (2003)
- [60] T. Karle, Y. J. Chai, C. N. Morgan, I. H. White and T. F. Krauss, *Observation of pulse compression in photonic crystal coupled cavity waveguides*, IEEE J. Lightwave Technol. **22**, 514 (2004)
- [61] R. März, S. Burger, S. Golka, A. Forschel, C. Hermann, C. Jamois, D. Michaelis and K. Wandel, *Planar high index-contrast photonic crystals for telecom applications*, in *Photonic crystals: Advances in design, fabrication and characterization*, ed. by K. Busch, S. Lölkes, R. B. Wehrspohn and H. Föll, Wiley, 308 (2004)
- [62] T. Baba, A. Motegi, T. Iwai, N. Fukaya, Y. Watanabe and A. Sakai, *Light propagation characteristics of straight single-line-defect waveguides in photonic crystals fabricated into a silicon-on-insulator substrate*, IEEE J. Quantum Electron. **38**, 743 (2002)
- [63] A. Talneau, L. Le Gouezigou and N. Bouadma, *Quantitative measurement of low propagation losses at 1.55  $\mu\text{m}$  on planar photonic crystal waveguides*, Opt. Lett. **26**, 1259 (2001)
- [64] C. Weisbuch, H. Benisty, S. Olivier, M. Rattier, C. J. M. Smith and T. F. Krauss, *3D control of light in waveguide-based two-dimensional photonic crystals*, IEICE Trans. Commun. **E84-B**, 1286 (2001)
- [65] W. Bogaerts, V. Wiaux, D. Taillaert, S. Beckx, B. Luyssaert, P. Bienstman and R. Baets, *Fabrication of Photonic Crystals in Silicon-on-Insulator Using 248-nm Deep UV Lithography*, IEEE J. Selec. Top. Quantum Electron. **8**, 928 (2002)
- [66] W. Bogaerts, P. Bienstman and R. Baets, *Scattering at sidewall roughness in photonic crystal slabs*, Opt. Lett. **28**, 689 (2003)

- [67] C. Jamois, R. B. Wehrspohn, J. Schilling, F. Müller, R. Hillebrand, and W. Hergert, *Silicon-based photonic crystal slabs: Two concepts*, IEEE J. Quantum Electron. **38**, 805 (2002)
- [68] L. C. Andreani and M. Agio, *Photonic bands and gap maps in a photonic crystal slab*, IEEE J. Quantum Electron. **38**, 891 (2002)
- [69] M. Qiu, *Effective index method for heterostructure-slab-waveguide-based two-dimensional photonic crystals*, Appl. Phys. Lett. **81**, 1163 (2002)
- [70] M. Qiu, *Band gap effects in asymmetric photonic crystal slabs*, Phys. Rev. B **66**, 033103 (2002)
- [71] O. Hess, C. Hermann and A. Klaedtke, *Finite-Difference Time-Domain simulations of photonic crystal defect structures*, Phys. Stat. Sol. (a) **197**, 605 (2003)
- [72] M. Galli, M. Agio, L.C. Andreani, L. Atzeni, D. Bajoni, G. Guizzetti, L. Businaro, E. Di Fabrizio, F. Romanato and A. Passaseo, *Optical properties and photonic bands of GaAs photonic crystal waveguides with tilted square lattice*, Eur. Phys. J. B **27**, 79 (2002)
- [73] T. Ochiai and K. Sakoda, *Nearly free-photon approximation for two-dimensional photonic crystal slabs*, Phys. Rev. B **63**, 125107 (2001)
- [74] H. Benisty, D. Labilloy, C. Weisbuch, C. J. M. Smith, T. F. Krauss, D. Cassagne, A. Béraud and C. Jouanin, *Radiation losses of waveguide-based two-dimensional photonic crystals: Positive role of the substrate*, Appl. Phys. Lett. **76**, 532 (2000)
- [75] E. Chow, S. Y. Lin et al., , Nature **407**, 983 (2000)
- [76] H. Benisty, S. Olivier, C. Weisbuch, M. Agio, M. Kafesaki, C. M. Soukoulis, M. Qiu, M. Swillo, A. Karlsson, B. Jaskorzynska, A. Talneau, J. Moosburger, M. Kamp, A. Forschele, R. Ferrini, R. Houdré and U. Oesterle, *Models and measurements for the transmission of submicron-width waveguide bends defined in two-dimensional photonic crystals*, IEEE J. Quantum Electron. **38**, 770 (2002)
- [77] C. T. Chan, Q. L. Yu and K. M. Ho, *Order-N spectral method for electromagnetic waves*, Phys. Rev. B **51**, 16635 (1995)
- [78] L. C. Andreani, *Photonic bands and radiation losses in photonic crystal waveguides*, Phys. Stat. Sol. (b) **234**, 139 (2002)
- [79] C. Hermann, C. Jamois, R. B. Wehrspohn, O. Hess and U. Gösele, *Cladding modes in silicon-on-insulator-based photonic crystal slabs*, submitted to Opt. Lett. (2004)
- [80] S. I. Bozhevolnyi, V. S. Volkov, J. Arentoft, A. Boltasseva, T. Søndergaard and M. Kristensen, *Direct mapping of light propagation in photonic crystal waveguides*, Opt. Commun. **212**, 51 (2002)
- [81] L. C. Andreani and M. Agio, *Intrinsic diffraction losses in photonic crystal waveguides with line defects*, Appl. Phys. Lett. **82**, 2011 (2003)
- [82] M. Lončar, D. Nedeljković, T. P. Pearsall, J. Vučković, A. Scherer, S. Kuchinsky and D. C. Allan, *Experimental and theoretical confirmation of Bloch-mode light propagation in planar photonic crystal waveguides*, Appl. Phys. Lett. **80**, 1689 (2002)
- [83] M. Lončar, J. Vučković and A. Scherer, *Methods for controlling positions of guided modes of photonic-crystal waveguides*, J. Opt. Soc. Am. B **18**, 1362 (2001)
- [84] R. März, *Integrated optics, design and modeling*, Artech House, Boston-London, (1995)

- [85] T. D. Happ, M. Kamp and A. Forscheil, *Photonic crystal tapers for ultracompact mode conversion*, Opt. Lett. **26**, 1102 (2001)
- [86] D. W. Prather, J. Murakowski, S. Shi, S. Venkataraman, A. Sharkawy, C. Chen and D. Pustai, *High-efficiency coupling structure for a single-line-defect photonic-crystal waveguide*, Opt. Lett. **27**, 1601 (2002)
- [87] E. Miyai, M. Okano, M. Mochizuki and S. Noda, *Analysis of coupling between two-dimensional photonic crystal waveguide and external waveguide*, Appl. Phys. Lett. **81**, 3729 (2002)
- [88] N. Moll and G.-L. Bona, *Comparison of three-dimensional photonic crystal slab waveguides with two-dimensional photonic crystal waveguides: Efficient butt coupling into these photonic crystal waveguides*, J. Appl. Phys. **93**, 4986 (2003)
- [89] S. G. Johnson, P. Bienstman, M. A. Skorobogatiy, M. Ibanescu, E. Lidorikis and J. D. Joannopoulos, *Adiabatic theorem and continuous coupled-mode theory for efficient taper transitions in photonic crystals*, Phys. Rev. E **66**, 066608 (2002)
- [90] S. W. Leonard, J. P. Mondia, H. M. van Driel, O. Toader, S. John, K. Busch, A. Birner, U. Gösele and V. Lehmann, *Tunable two-dimensional photonic crystals using liquid-crystal infiltration*, Phys. Rev. B **61**, R2389 (2000)
- [91] G. Mertens, T. Röder, H. Matthias, H. Marsmann, H.-S. R. Kitzerow, S. L. Schweizer, C. Jamois, R. B. Wehrspohn and M. Neubert, *Two- and three-dimensional photonic crystals made of macroporous silicon and liquid crystals*, Appl. Phys. Lett. **83**, 3036 (2003)
- [92] Y. Luo, I. Szafraniak, V. Nagarjan, R. B. Wehrspohn, M. Steinhart, J. H. Wendorff, N. D. Zakharov, R. Ramesh and M. Alexe, *Ferroelectric switching of nanotubes composed of lead zirconate titanate and barium titanate*, Appl. Phys. Lett. **83**, 440 (2003)
- [93] S. W. Leonard, H. Van Driel, J. Schilling and R. B. Wehrspohn, *Ultrafast band-edge tuning of a two-dimensional silicon photonic crystal via free-carrier injection*, Phys. Rev. B **66**, 161102 (2002)
- [94] Y.-K. Ha, J.-E. Kim, H. Y. Park, C.-S. Kee and H. Lim, *Tunable three-dimensional photonic crystals using semiconductors with varying free-carrier densities*, Phys. Rev. B **66**, 075109 (2002)
- [95] S. W. Leonard, PhD thesis, University of Toronto, Dept. of Physics (2001)
- [96] C. Jamois, T. Geppert and R. B. Wehrspohn, *Design of a new taper for light coupling between a ridge waveguide and a photonic crystal waveguide*, Mat. Res. Soc. Symp. Proc. **797**, W6.7.1 (2004)
- [97] M. Köhler, *Etching in Microsystem Technology*, Wiley, (1999)
- [98] W. Whyte, *Cleanroom Design*, Wiley, (1999)
- [99] V. N. Astratov, I. S. Culshaw, R. M. Stevenson, D. M. Whittaker, M. S. Skolnick, T. F. Krauss and R. M. De La Rue, *Resonant coupling of near-infrared radiation to photonic band structure waveguides*, IEEE J. Lightwave Technol. **17**, 2050 (1999)
- [100] D. M. Manos and D. L. Flamm, *Plasma Etching: an Introduction*, Academic Press, Inc., (1989)
- [101] S. H. Jeong, S.-J. Choi, H.-S. Cha, S.-Y. Yoon, S.-M. Jung, S.-S. Choi and J.-H. Lee, *Dry-etching characteristics of attenuated phase-shifting masks using  $Cl_2/CF_4/O_2/He$  plasmas*, Jpn. J. Appl. Phys. **41**, 5419 (2002)

- 
- [102] H. Nakata, K. Nishioka, and H. Abe, *Plasma etching characteristics of chromium film and its novell etching mode*, J. Vac. Sci. Technol. **17**, 1351 (1980)
- [103] information given by Oxford Plasma Technologies
- [104] A. P. Milenin, C. Jamois, M. Reiche and R. B. Wehrspohn, *Sub-micron patterning of Cr using  $Cl_2/O_2$  plasma etching*, submitted to J. Vac. Sci. Technol. (2004)
- [105] M. Schaepkens and G. S. Oehrlein, *A review of  $SiO_2$  etching in inductively coupled fluorocarbon plasmas*, J. Electrochem. Soc. **148**, C211 (2001)
- [106] J-H. Min, S-W. Hwang et al., *Redeposition of etch products on sidewalls during  $SiO_2$  etching in a fluorocarbon plasma. I. Effect of particle emission from the bottom surface in a  $CF_4$  plasma*, J. Vac. Sci. Technol. A **20**, 1574 (2002)

# List of Publications

- C. Jamois, R.B. Wehrspohn, J. Schilling, F. Müller, R. Hillebrand, and W. Hergert, *Silicon-Based Photonic Crystal Slabs: Two Concepts*, IEEE J. Quantum Electron. **38**, 805-810 (2002)
- C. Jamois, R.B. Wehrspohn, C. Hermann, O. Hess, L.C. Andreani, and U. Gösele, *Silicon-Based Two-Dimensional Photonic Crystal Waveguides*, Photonics and Nanostructures: Fundamentals and Applications **1**, 1-13 (2003)
- C. Jamois, R.B. Wehrspohn, C. Hermann, O. Hess, L.C. Andreani, and U. Gösele, *Silicon-Based Two-Dimensional Photonic Crystal Waveguides*, in *Micro-Optics*, ed. by J. Jahns, Springer (2003)
- C. Jamois, T. Geppert and R.B. Wehrspohn, *Design of a New Taper for Light Coupling Between a Ridge Waveguide and a Photonic Crystal Waveguide*, Mat. Res. Soc. Symp. Proc. **797**, W6.7.1 (2004)
- R. März, S. Burger, S. Golka, A. Forchel, C. Hermann, C. Jamois, D. Michaelis, and K. Wandel, *Planar High Index-Contrast Photonic Crystals for Telecom Applications*, in *Photonic Crystals: Advances in Design, Fabrication and Characterization*, ed. by K. Busch, S. Lölkes, R. B. Wehrspohn and H. Föll, Wiley, 308 (2004)
- R. Hillebrand, C. Jamois, J. Schilling, R.B. Wehrspohn and W. Hergert, *Computation of Optical Properties of Si-Based Photonic Crystals with Varying Pore Diameters*, Phys. Stat. Sol. (b) **240**, 124 (2003)
- C. Hermann, C. Jamois, R.B. Wehrspohn, O. Hess and U. Gösele, *Cladding Modes in Silicon-On-Insulator-Based Photonic Crystal Slabs*, submitted to Opt. Lett. (2004)
- A. P. Milenin, C. Jamois, M. Reiche and R. B. Wehrspohn, *Sub-Micron Patterning of Cr using Cl<sub>2</sub>/O<sub>2</sub> Plasma Etching*, submitted to J. Vac. Sci. Technol. (2004)
- G. Mertens, T. Röder, H. Matthias, H. Marsmann, H-S. R. Kitzerow, S.L. Schweizer, C. Jamois, R.B. Wehrspohn and M. Neubert, *Two- and Three-Dimensional Photonic Crystals Made of Macroporous Silicon and Liquid Crystals*, Appl. Phys. Lett. **83**, 3036 (2003)
- S. Matthias, F. Müller, C. Jamois, R.B. Wehrspohn and U. Gösele, *Large-Area Three-Dimensional Nanostructuring by Self-Organized Electrochemical Etching and Lithography*, to be published in Adv. Mat.
- R. B. Wehrspohn, S. L. Schweizer, J. Schilling, T. Geppert, C. Jamois, R. Glatthaar, P. Hahn, A. Feisst and A. Lambrecht, *Application of photonic crystals for gaz detection and sensing*, in *Photonic crystals: Advances in design, fabrication and characterization*, ed. by K. Busch, S. Lölkes, R. B. Wehrspohn and H. Föll, Wiley, 238 (2004)

---

S. Richter, S. L. Schweizer, R. Hillebrand, C. Jamois, R. B. Wehrspohn, M. Zacharias and U. Gösele, *Interaction of Periodically Arranged Point Defects in a Two Dimensional Photonic Crystal - The Photonic Analogue to a Doped Semiconductor*, Mat. Res. Soc. Symp. Proc. **797**, 51 (2004)

S. Richter, S. L. Schweizer, R. Hillebrand, C. Jamois, R. B. Wehrspohn, M. Zacharias and U. Gösele, *Periodically Arranged Point Defects in a Two Dimensional Photonic Crystal - The Photonic Analogue to a Doped Semiconductor*, Proc. SPIE **5277**, 238 (2004)

# Acknowledgments

I am very grateful to all the colleagues, collaborators, friends, and relatives, who contributed to the success of my PhD thesis.

First of all, I would like to express my gratitude to my supervisors, Prof. Gösele for giving me the opportunity to do my PhD in his department, and Prof. Wehrspohn for his guidance, his support and his optimism. Without the collaboration of Christian Hermann and his supervisor Prof. Hess, as well as of Prof. Andreani, my thesis would have looked completely different. I enjoyed our fruitful discussions, that helped me understand the physics of planar photonic crystals, and motivated me to continue doing research in the future. I also thank my colleagues from the photonic crystal group at the Max Planck Institute and the University of Halle, in particular Jörg Schilling, Dr. Hillebrand and Prof. Hergert, who explained me the basics of photonic crystals at the beginning of my PhD, and Torsten Geppert for the long simulation days to test the taper design. Many thanks also to Dr. März for his advice on integrated optics, especially in terms of the ridge waveguide design.

The experimental part of my work would not have been a success without the important contribution of some of my colleagues. In particular, I shared together with Alexey Milenin and Christian Cojocar a nice etching adventure. I am also grateful to Mr. Meyer and Mr. Ilbrig for helping me in the sample preparations, and to Dr. Reiche for allowing me to enter his Clean-room and for his motivation to help me increase my self-control and frustration resistance day after day. In a similar way, I would also like to thank Martin Kamp for performing the electron-beam lithography on some of my samples, as well as his electron-beam equipment, which was so many months under reparation that I had time to perform all this interesting theoretical study. More importantly, I would like to thank Dr. Erfurth and Ms. Doss for their introduction and help in SEM investigations and electron-beam lithography.

Finally, I appreciated very much the support of Frank Müller, who treated my dear computers day after day. Many thanks to all my other colleagues and friends at the Max Planck Institute for the nice atmosphere. I also acknowledge financial support from the German Ministry of Research within the project "HiPhoCs", as well as the collaboration with the other partners in this BMBF project.

Un grand Merci to the "French Clan", Gwilherm, Mathieu, Jean-Marc and Carine for keeping me in good mood, and to my family, who has always been at my side despite the distance between us.

My last thought is for Ming-Wen. I would like to thank him, not only for his love and his attention, but also for the long nights he spent improving my English writing...

# Eidesstattliche Erklärung

Ich erkläre hiermit, dass ich keine anderen als die von mir angegebenen Quellen und Hilfsmittel zur Erstellung meiner Dissertation verwendet habe. Den benutzten Werken wörtlich oder inhaltlich entnommene Stellen sind als solche gekennzeichnet.

Cécile Jamois.

Halle (Saale), im Januar 2004.

# Curriculum vitae

First Name	Cécile
Family Name	Jamois
Date of Birth	April 19, 1977 (Rennes, France)
Nationality	French
Permanent Address	14 Rue des Bas Gasts F-35240 Marcillé-Robert, France
E-mail	jamois@mpi-halle.de

---

## EDUCATION

<i>Oct. 2000 - present</i>	Max Planck Institute of Microstructure Physics and Martin-Luther-University Halle Wittenberg (Halle, Germany) Ph.D. candidate (Supervisors: Prof. Ulrich Gösele and Prof. Ralf B. Wehrspohn)
<i>Sept. 1999 - Sept. 2000</i>	Physical Engineering study at INSA de Rennes (Institut National des Sciences Appliquées, Rennes, France)
<i>Sept. 1998 - June 1999</i>	RWTH Aachen (Aachen, Germany) Exchange student within the Erasmus program
<i>Sept. 1995 - June 1998</i>	Physical Engineering study at INSA de Rennes (Rennes, France)
<i>June 1995</i>	Science-based Baccalauréat (A)

---

## PROFESSIONAL EXPERIENCE

<i>Mar. 2000 - Sept. 2000</i>	Philips Forschungslaboratorien Aachen (Aachen, Germany) Diploma thesis in Physical Engineering (Supervisors: Prof. Bertrand Lambert (INSA Rennes) and Dr. Indra Ghosh (Aachen)) Thesis: Study of photonic crystals and application in the microwave regime
-------------------------------	---

---

---

*July 1999 - Aug. 1999* Philips Forschungslaboratorien Aachen (Aachen, Germany)  
Internship in the Electrical Ceramics Department  
Subject: Study and fabrication of antennas in the microwave regime

*Aug. 1997 & Aug. 1998* Seasonal work at Organic Ile-de-France (Paris, France)

---

#### PRIZES and FELLOWSHIPS

*Sept. 1998* Erasmus Scholarship, RWTH Aachen, Germany.

*June 1995* Prize of the Scientific Vocation for Young Females, Rennes, France.